



Title	Mechanical response and damage analysis of asphalt pavement subjected to wheel loads in seasonally cold region
Author(s)	SI, Junling
Citation	北海道大学. 博士(工学) 甲第15678号
Issue Date	2023-12-25
DOI	10.14943/doctoral.k15678
Doc URL	http://hdl.handle.net/2115/91188
Type	theses (doctoral)
File Information	SI_Junling.pdf



[Instructions for use](#)

**Mechanical response and damage analysis of asphalt pavement
subjected to wheel loads in seasonally cold region**

輪荷重を受ける積雪寒冷地のアスファルト舗装の構造解析手法の提案

By

Junling SI

A thesis submitted in partial fulfilment of the requirements for the degree of Doctor of

Philosophy in Engineering

under the guidance and supervision of

Professor Tatsuya ISHIKAWA

Examined by the Doctoral Committee

Professor Tatsuya ISHIKAWA

Professor Yoshiaki FUJII

Professor Satoshi NISHIMURA

December 2023

English Engineering Program (e³)

Laboratory of Analytical Geomechanics

Division of Field Engineering for the Environment

Graduate School of Engineering

Hokkaido University

Sapporo, Hokkaido, Japan

ABSTRACT

Asphalt pavement is a commonly used form of infrastructure exposed to various environmental impacts and traffic load actions. There has been increasing concern about the deepening of asphalt pavement damage. During the initial stage of service, most of the damage is usually on the pavement surface. However, damage can occur in the base and subgrade layers where the pavement has aged severely. Therefore, accurately predicting the fatigue life of asphalt pavement requires a comprehensive understanding of its mechanical response to significant environmental impacts. This becomes especially crucial in cold regions where temperature variations, moisture fluctuations, and freeze–thaw action can significantly impact the performance and durability of asphalt pavements.

Current Japanese theoretical pavement structure design method (TPSDM) uses mechanical empirical criteria to predict the fatigue loading number against fatigue cracking and rutting. Although the TPSDM is widely used for designing asphalt pavements in Japan, it still exhibits certain limitations, such as not considering the variation in moduli of the base and subgrade layers due to water contents, freeze–thaw action, and stress states. This study aims to enhance Japanese TPSDM's accuracy by considering variations in the resilient modulus of environmental impacts, pavement materials, pavement structure, and traffic load actions to accurately calculate the mechanical responses and predict pavement fatigue life.

Firstly, the study develops a 3D Thermo-Hydro-Mechanical (THM) model using the finite element method (FEM). Based on a nonlinear elastic model and convergence analysis, the mechanical field is developed within the proposed coupled model. The thermal and hydraulic fields are established by the PDEs (partial differential equations). Secondly, this study uses ODEs (ordinary differential equations) to characterize the physical state of geomaterials and quantify the number of days passed during the recovery period on the element scale. Furthermore, modeling the geomaterials with a stress-dependent modulus is a typical coupling problem that involves a circular dependence among resilient modulus, matric suction, temperature, stress, and deformation. This circular dependence can be solved in the WF-PDEs (weak form partial differential equations) to define the stress-dependent modulus. Lastly, in a multi-layer elastic model, the structural response results can be generated by utilizing the resilient modulus, which is influenced by the stress state and environmental impacts. Based on empirical models, the structural response results can then estimate the expected allowable loading number against rutting and fatigue cracking.

The method of modifying the rutting failure criterion by incorporating the MEPDG model and the PSAR effect enhances the practicality of the rutting model. To validate the proposed method, this study conducts a comparative analysis to compare its predictions with those obtained using established pavement design methods. Additionally, field validation is conducted to confirm the effectiveness of the method in real-world scenarios by monitoring pavement moisture content and temperature changes, as well as actual fatigue life and modulus. Results indicate that the modifications improve the Japanese TPSDM by considering the environmental impacts, traffic load actions, pavement materials, and pavement structure, thereby improving the accuracy of predicting the fatigue life of asphalt pavements, particularly in cold regions.

The thesis is composed of 7 chapters. Chapter 1 introduces the study's background, objectives, and the need for improvement in the Japanese theoretical pavement structure design method. Chapter 2 provides an overview of several resilient modulus and permanent deformation prediction models for pavement materials, the THM coupled model and effect of principal stress axis rotation. Chapter 3 summarizes the environmental impacts on pavement systems and verifies the validity of the TH coupled model by comparing the measured and simulated results. Chapter 4 investigates the infiltration behavior of asphalt pavements under rainfall, with a specific focus on the hydraulic properties of the As layer and compares the applicability of single-phase and two-phase flow models in simulating such behavior. Chapter 5 establishes a system for evaluating the environmental impact on resilient modulus of pavement materials and verifies it through field measurements. Chapter 6 replaces the constant elastic modulus of the base layer and subgrade layer with an elastic modulus related to the stress state and complex environmental impacts, and modifies the rutting failure criterion, then examines the applicability of the modified design approach. Finally, Chapter 7 summarizes the study's findings, provides recommendations for pavement design improvements, and discusses enhancing pavement fatigue life.

**< This dissertation is a modified and revised form of the following
original journals and proceedings >**

1. Si, J., Ishikawa, T., Ren D, Maruyama, K., Ueno, C. (2023). Response prediction of asphalt pavement in cold region with thermo-hydro-mechanical coupling simulation. *Sustainability*, 15(18), 13614.

2. Ishikawa, T., Si, J., Ren, D., Maruyama, K., Takahashi, S. (2023). Proposal of pavement structure design and performance evaluation method considering environmental factors based on transportation geotechnics. *Expressways and automobiles*, 66(5), 13-20. (in Japanese)

3. Si, J., Ishikawa, T., Maruyama, K., Ueno, C. Evaluation of resilient modulus of asphalt pavement in cold region based on Thermo-Hydro-Mechanical coupling simulation, 97-106. 62nd Annual Meeting of the JGS Hokkaido branch, Hakodate, Japan, 2022.1.

4. Si, J., Ishikawa, T. Development of a new Thermo-Hydro-Mechanical coupling simulation for prediction of resilient modulus of asphalt pavement in cold region, 2nd Japanese symposium on transportation geotechnics, Fukuoka, Japan, 2022.11.

5. Ren, D., Ishikawa, T., Si, J., Tokoro, T. Effect of hysteresis of soil-water characteristic curve on resilient modulus of subgrade soil under different climatic and stress conditions, Transportation Research Board 102nd Annual Meeting, Washington, USA, 2023.1.

6. Si, J., Ishikawa, T. Evaluation of resilient modulus of asphalt pavement in cold region with Thermo-Hydro-Mechanical coupling simulation. 17th Asian Regional Conference on Soil Mechanics and Geotechnical Engineering, Astana, Kazakhstan, 2023.8.

ACKNOWLEDGEMENT

I am honored to express my deepest appreciation to my supervisor, Prof. Tatsuya Ishikawa, for his exceptional guidance, unwavering support, and invaluable advice throughout the course of my doctoral study. His rigorous academic attitude and hardworking spirit have always been a great source of inspiration to me. Without his mentorship and assistance, this dissertation would not have been possible.

I would also like to extend my sincere gratitude to the members of the doctoral committee, Prof. Yoichi Watabe, Prof. Yoshiaki Fujii, and Prof. Satoshi Nishimura, for their constructive comments and insightful suggestions not only on this dissertation but also on annual evaluations.

Furthermore, I would like to express my heartfelt appreciation to Dr. Kimio Maruyama, who provided me with relevant field and laboratory experimental data, as well as innovative suggestions for this study. My sincere thanks also go to Prof. (Assoc.) Koichi Isobe and Prof. (Asst.) Shoji Yokohama for their support and valuable advice. The research support and precious data provided by Dr. Ueno Chigusa made the validation and verification of this study possible.

I am also deeply indebted to Dr. Yulong Zhu, Dr. Tianshu Lin, and Dr. Bin Luo for their invaluable assistance during my doctoral study. Mr. Daoju Ren not only provided laboratory data support for my research but also offered me much help in daily life. I would also like to acknowledge the students of the Laboratory of Analytical Geomechanics for their generous help throughout these years.

This research was made possible through the financial support of the Hokkaido University Ambitious Doctoral Fellowship and Hokkaido University DX Doctoral Fellowship.

Finally, I would like to extend my special thanks to my beloved parents, family, and friends, especially my girlfriend, Xiaojun Gong. Without their encouragement, support, and confidence in me all through these years, it would not have been possible for me to come to Japan and complete my doctoral study successfully.

TABLE OF CONTENTS

ABSTRACT	I
ACKNOWLEDGEMENT	IV
TABLE OF CONTENTS	V
LIST OF FIGURES	VIII
LIST OF TABLES	XI
1 INTRODUCTION	1
1.1 Background.....	1
1.2 Thesis objectives and research methodology	4
1.3 Thesis organization.....	7
2 LITERATURE REVIEW	9
2.1 Resilient modulus prediction models	9
2.2 Permanent deformation prediction models.....	11
2.3 Environmental impacts and THM coupling simulation.....	12
2.4 Effect of principal stress axis rotation	13
3 NUMERICAL SIMULATIONS FOR EVALUATING THE ENVIRONMENTAL IMPACTS.....	15
3.1 Numerical simulation assumptions.....	15
3.2 Governing equations and basic physical parameters	17
3.2.1 Hydraulic properties	18
3.2.2 Thermal properties.....	19
3.2.3 SFCC derived from SWCC	19
3.3 Analytical procedures	20
3.4 FWD test and field measurement	21
3.5 Numerical model and boundary conditions.....	23
3.5.1 Estimation of precipitation	25
3.5.2 Modeling upper and lower surface thermal boundaries.....	26
3.6 Material properties and input parameters	29
3.7 Comparison results between simulation and measurement	30
3.8 Summary.....	34

4	PAVEMENT INFILTRATION BEHAVIOR CONSIDERING HYDRAULIC	
	PROPERTIES OF AS LAYER	36
4.1	Experimental modeling	36
4.1.1	Design of the model test	36
4.1.2	Model Testing Apparatus	37
4.1.3	Materials of model test	38
4.2	Numerical simulation	39
4.2.1	Governing equations for two-phase flow in porous media.....	39
4.2.2	Retention and permeability relationships	40
4.2.3	Intrinsic permeability.....	41
4.2.4	Numerical model and boundary conditions.....	43
4.2.1	Material properties for the verification.....	44
4.3	Comparison results between simulation and measurement.....	45
4.4	Summary.....	48
5	RESILIENT MODULUS ESTIMATION OF PAVEMENT CONSIDERING THE	
	ENVIRONMENTAL IMPACTS	49
5.1	Evaluation of temperature-dependent resilient modulus of the asphalt layer.....	49
5.2	Effects of soil moisture variations and freeze–thaw action on resilient modulus.....	52
5.2.1	Evaluation of resilient modulus of pavement geo-materials	52
5.2.2	Assessment of physical condition of pavement elements.....	57
5.3	Numerical simulation results	59
5.4	Verification of MEPSCA	64
5.5	Summary.....	71
6	FATIGUE LIFE EVALUATION OF PAVEMENT CONSIDERING THE	
	ENVIRONMENTAL IMPACTS	73
6.1	Analytical procedures	73
6.2	Predicted fatigue life with TPSDM and MEPSCA	74
6.2.1	Fatigue life analysis of asphalt pavements	74
6.2.2	Traffic volume observation	76
6.3	Adoption of MEPDG rutting prediction model.....	77
6.4	Consideration of principal stress axis rotation effect	79
6.5	Comparison of fatigue life prediction.....	82

6.6	Summary.....	86
7	CONCLUSIONS AND RECOMMENDATIONS	87
7.1	Conclusions and recommendations	87
7.2	Future assignments	89
	LIST OF NOTATIONS.....	91
	LIST OF REFERENCES	98

LIST OF FIGURES

Figure 1-1 Types of pavement damage in in seasonally cold region ((a)Fatigue cracks; (b) Rutting).....	2
Figure 1-2 Conceptual schematic of design process.	5
Figure 3-1 Scheme of THM coupled model.....	16
Figure 3-2 Flow chart of THM analysis and convergence analysis.	21
Figure 3-3 FWD testing on test pavement.....	22
Figure 3-4 Field measurement for ground temperature and water content.....	23
Figure 3-5 Boundary condition and finite element mesh.	24
Figure 3-6 The pavement structure of Bibi test pavement.	25
Figure 3-7 Factors affecting hydraulic field in pavements.....	25
Figure 3-8 Factors affecting thermal field in pavements.....	27
Figure 3-9 Ground temperature at different depths.....	31
Figure 3-10 Frost-penetration depth curve over time.....	32
Figure 3-11 Degree of saturation curve over time.....	33
Figure 4-1 Front view of the test apparatus.....	37
Figure 4-2 Schematic diagram of the test apparatus (Unit: mm).....	38
Figure 4-3 Grain size distribution of testing material.....	39
Figure 4-4 Boundary condition and finite element mesh for model test.....	43
Figure 4-5 SWCC of asphalt mixture.....	44
Figure 4-6 Time evolution of the wetting front.....	45
Figure 4-7 Measured and calculated evolution of water content profile during an infiltration process (Two-phase flow model).	46
Figure 4-8 Measured and calculated evolution of water content profile during an infiltration process (Single-phase flow model).	47
Figure 4-9 Process of rainwater infiltration into interface (Two-phase flow model) (1.5hours).	47

Figure 4-10 Process of rainwater infiltration into interface (Single-phase flow model) (1.5hours).	48
Figure 5-1 Relationship between the elastic modulus of the As layer and temperature.....	50
Figure 5-2 Relationship between the elastic modulus of the As layer and temperature (proposed model).....	51
Figure 5-3 The change of the resilient modulus of As layer within one year.....	52
Figure 5-4 Time-depth diagram of a typical pavement structure.	55
Figure 5-5 The relationship between element temperature and recovery period.	58
Figure 5-6 Resilient modulus distribution in different seasons ((a) regular season-sunny day; (b) regular season-rainy day; (c) freezing season; (d) partial thawing season; (e) thawing season).	62
Figure 5-7 Distribution of the resilient modulus and degree of saturation during the freezing and thawing process ((a) resilient modulus; (b) degree of saturation).	63
Figure 5-8 Simulated and measured resilient modulus of base course layer.....	64
Figure 5-9 Simulated and measured resilient modulus of subgrade layer.....	65
Figure 5-10 Simulated and measured resilient modulus of base course layer ((a). section A; (b). section B; (c). section C; (d). section D).....	68
Figure 5-11 Simulated and measured resilient modulus of subgrade layer ((a). section A; (b). section B; (c). section C; (d). section D).	70
Figure 6-1 Flowchart of evaluating fatigue life.....	74
Figure 6-2 Three-layered model for allowable loading number calculation.	75
Figure 6-3 Allowable loading number calculated through TPSDM and MEPDG model.	78
Figure 6-4 Predicted N_{fs} and actual failure loading number.	79
Figure 6-5 Stress variation of pavement under moving wheel loads.....	80
Figure 6-6 Predicted N_{fs} and actual failure loading number considering PSAR effect.	82
Figure 6-7 Comparison of N_{fs} for different sections under various fatigue life prediction models.	83
Figure 6-8 Comparison of $ACC_{N_{fs}}$ for different sections under various fatigue life prediction models.	84

Figure 6-9 Comparison of N_{fa} for different sections under various fatigue life prediction models. 85

Figure 6-10 Comparison of $ACC_{N_{fa}}$ for different sections under various fatigue life prediction models. 85

Figure 7-1 Scheme of the proposed MEPSCA 87

LIST OF TABLES

Table 2-1 Summary of resilient modulus prediction models.....	9
Table 2-2 Summary of permanent deformation prediction models.....	11
Table 3-1 Measured Ground Temperature.	29
Table 3-2 Material input parameters in TH analysis.	29
Table 4-1 Material input parameters in two-phase flow analysis.....	44
Table 5-1 Mechanism of bearing capacity reduction due to freeze-thaw.....	56
Table 5-2 The number of days required for a geomaterial from thawed state to unfrozen state.....	56
Table 5-3 Material input parameters in mechanical analysis.	59
Table 5-4 Selection of weather conditions.	59
Table 6-1 Reliability and coefficient corresponding to the reliability in Japanese pavement design guide.....	81

1 INTRODUCTION

1.1 Background

Asphalt pavement is a commonly used form of infrastructure exposed to various environmental impacts and traffic load actions. Recently, there has been increasing concern about the deepening of asphalt pavement damage. During the initial stage of service, most of the damage is usually on the pavement surface. However, damage can occur in the base and subgrade layers where the pavement has aged severely (Takahashi et al., 2015). Therefore, accurately predicting the fatigue life of asphalt pavement requires a comprehensive understanding of its mechanical response to significant environmental impacts. Asphalt pavement in cold snowy regions such as Hokkaido suffers from freeze-thaw cycles as the 0°C isotherm may penetrate deep into the pavement. Freeze-thaw action deteriorates the pavement structures in two ways as frost-heave and thaw-weakening. The frost heave of soils during freezing caused by an increase in the ice lens finally induces the surface cracking in the asphalt mixture layer. On the other hand, the thaw-weakening means a drop of the bearing capacity for base and subgrade layers caused by suddenly rising water content, which comes from the inflow of snowmelt water or the thawing of ice lenses (Jong et al., 1998; Simonsen and Isacsson, 1999). Therefore, it becomes especially crucial in cold regions where temperature variations, moisture fluctuations, and freeze-thaw action can significantly impact the performance and durability of asphalt pavements (Kabir and Tighe, 2023; Zeiada et al., 2019). To develop a mathematical model of the mechanical response of the subbase course in cold regions and incorporate it into the theoretical design method for pavement structures in the future, a detailed understanding of the mechanical behavior of the subgrade and base course during freeze-thaw is essentially required.

Field examinations and evaluations of most pavements found that fatigue cracking and rutting (Figure 1-1) are the most significant pavement distresses (Abdullah, 2023; Perić et al., 2022). The Mechanistic-Empirical Pavement Design Guide (MEPDG) (AASHTO, 2008) in the United States uses various models to simulate the pavement structure and its

response to traffic load actions, environmental impacts, and other factors that affect pavement performance. The MEPDG considers factors such as pavement material properties, layer thicknesses, and other design inputs to predict pavement distresses such as fatigue cracking and rutting (AASHTO, 2008). The theoretical pavement structure design method (TPSDM), currently used in Japan, relies on mechanical-empirical standards to simply and quickly estimate the failure loading number against rutting and fatigue cracking (Japan Road Association, 2006). Nonetheless, it is essential to address the limitations of the TPSDM compared to the MEPDG, particularly concerning pavement material properties, environmental impacts, and design life aspects. Here, pavement material properties involve mechanical characteristics, like resilient modulus, while environmental impacts involve the influencing temperature variations, moisture fluctuations, and freeze–thaw action on pavement performance. The design life involves considering the impact of traffic loads on predicted fatigue life against cracking and rutting.



Figure 1-1 Types of pavement damage in in seasonally cold region ((a)Fatigue cracks; (b) Rutting).

The resilient modulus (M_r) is a crucial input for mechanistic pavement analysis in the design of traditional flexible pavements with base course and subgrade layers. For the pavement material properties, the TPSDM assumes that the base course and subgrade layers are linear elastic materials with constant moduli under equivalent 49-kN wheel load conditions throughout the year. However, these geomaterials exhibit nonlinear elastic properties with strain levels exceeding 10^{-6} , which can be estimated by resilient modulus (M_r) (Clayton, 2011; Seed et al., 1955). Thus, in the pavement response analysis of the

MEPDG, the relationship between the stress state and resilient modulus is captured by using the universal constitutive equation (Equation (1-1)), which establishes a connection between the resilient modulus and various stress parameters, including bulk stress, octahedral shear stress, and atmospheric pressure at a specific location within the pavement (AASHTO, 2008).

$$M_r = k_1 \cdot p_a \cdot \left(\frac{\theta}{p_a}\right)^{k_2} \cdot \left(\frac{\tau_{oct}}{p_a} + 1\right)^{k_3} \quad (1-1)$$

where k_1 , k_2 , and k_3 are regression constants; p_a is atmospheric pressure; θ is bulk stress; and τ_{oct} is octahedral shear stress.

In addition, the performance of flexible pavements is significantly affected by environmental conditions (Cole et al., 1981; Johnson et al., 1978; Simonsen and Isacsson, 2001; Simonsen et al., 2002). The interaction between environmental conditions, pavement materials, and pavement design should be fully explored. External factors, such as precipitation, temperature, freeze–thaw cycles, and groundwater level, play a crucial role in determining the extent to which the environment can impact pavement performance. Internal factors, including the susceptibility of geomaterials to moisture and freeze–thaw damage and the infiltration potential of the pavement, also play a role in determining how the pavement will react to external environmental conditions (Ishikawa et al., 2019a; Lin et al., 2019b; Peng et al., 2020; Vaitkus et al., 2016). In the numerical simulation, the resilient modulus of any element (including the base course layer and subgrade layer) is affected by the water content and the physical state of the geomaterial (e.g., frozen state, recovering state, and unfrozen state). According to the definitions of the MEPDG, the recovery period refers to the thawed geomaterial that is gradually returning to its state before freezing occurs. Hence, during this period, the resilient modulus is influenced by the number of days that have elapsed since thawing started (AASHTO, 2008). Considering these aspects, it is essential to reproduce the external environmental impacts and explore their influences on the pavement materials during the pavement design process. The MEPDG suggests an Enhanced Integrated Climatic Model (EICM), which captures the change in water content and freeze–thaw action (NCHRP, 2004). Additionally, Ishikawa et al. (2019a) examined the impact of freeze–thaw action and the concurrent seasonal fluctuations in water content, named as climate effect, on the resilient deformation

characteristics of base course materials, while Lin et al. (2022) examined the climate effect on the resilient modulus of subgrade soil to evaluate the mechanical behavior of asphalt pavement in cold regions.

Rutting is a common form of pavement distress, particularly under the condition of repeated traffic loads over time. To improve the reliability of predicting fatigue life, it is essential to consider not only the direct effects of factors such as traffic repetition on rutting but also the rate-hardening behavior of the pavement layers and the contribution of non-subgrade layers to rutting (Lin et al., 2021; NCHRP, 2004). Additionally, the effect of principal stress axis rotation (PSAR) is widely believed to significantly impact the mechanical performance of pavement materials (Gräbe and Clayton, 2009; Inam et al., 2012; Ishikawa et al., 2019b; Ishikawa et al., 2011b; Lekarp and Dawson, 1998; Lin et al., 2019a; Miura et al., 1986). Lin et al. (2021) introduced an adjustment parameter based on the MEPDG rutting depth prediction model (Equation (1-2)) to modify the Japanese rutting failure criterion and proposed the ratio of axial strain, estimated with axial stress and shear stress, as a quantitative measure to describe the increase in axial strain caused by PSAR.

$$\varepsilon_p(N) = \beta_1 K_1 \left(\frac{\varepsilon_0}{\varepsilon_r} \right) e^{-\left(\frac{\rho}{N} \right)^\beta} \varepsilon_v \quad (1-2)$$

where $\varepsilon_p(N)$ is the permanent strain for the layer/sub-layer; N is the number of traffic repetitions; ε_0 , β , and ρ are material properties; ε_r is the resilient strain imposed in laboratory testing to obtain material properties ε_0 , β , and ρ ; ε_v is the average vertical resilient strain in the layer, which is calculated by a multi-layer elastic pavement response model; β_1 is the calibration factor for the unbound granular and subgrade materials; and K_1 is the global calibration coefficient.

1.2 Thesis objectives and research methodology

The objective of this study is to improve the TPSDM by incorporating various factors and elements to account for environmental impacts, traffic load actions, pavement materials, and pavement structure changes, as shown in Figure 1-2, and to form a comprehensive analytical procedure, named as the Mechanistic-Empirical Pavement Structure Coupled Analysis (MEPSCA).

For this purpose, this study attempts to,

(1) develop a three-dimensional (3D) Thermo-Hydro-Mechanical (THM) coupled model by using the Finite Element Method (FEM) to study the temperature and moisture distributions of the pavement with time.

(2) investigate the infiltration behavior of asphalt pavements under rainfall, with a specific focus on the hydraulic properties of the As layer, and to compare the applicability of single-phase and two-phase flow models in simulating such behavior.

(3) replace the constant elastic modulus of the base and subgrade layer in the TPSDM with the resilient modulus that considers the stress state and the combined effects of water content fluctuations and freeze–thaw action based on the moisture, temperature, and stress state obtained from THM analysis.

(4) propose methods to establish the physical state of the geomaterial (e.g., frozen state, recovering state, and unfrozen state).

(5) obtain the mechanical response of the pavement and calculate the fatigue life of the pavement under the environmental impacts.

(6) propose the seamless integration of these advancements when considering the environmental impacts, such as thaw-weakening and moisture fluctuations, into the pavement performance evaluation in terms of transportation geotechnics.

(7) tackle the issue of significant differences between actual performance life and design life, ultimately providing a more comprehensive pavement design method.

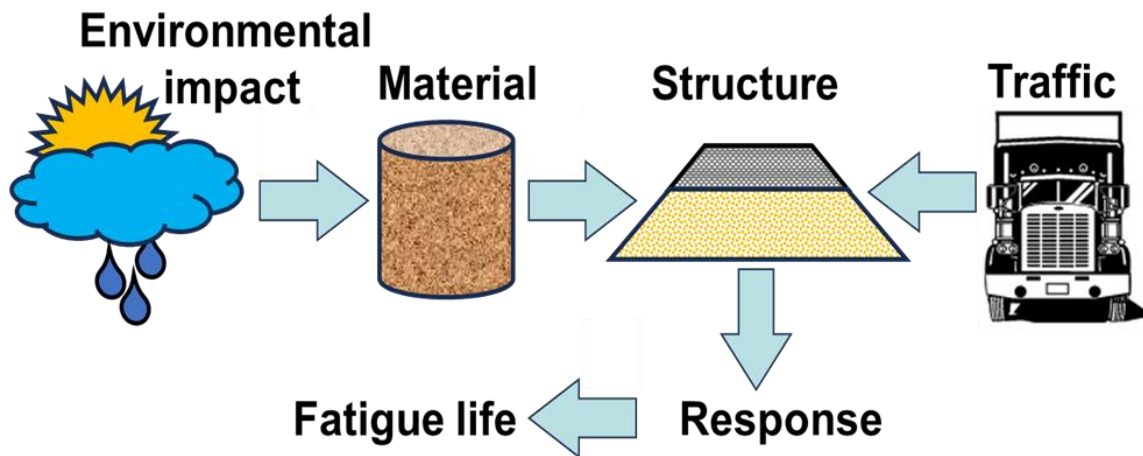


Figure 1-2 Conceptual schematic of design process.

The proposed design method represents a significant change in how pavement design is performed compared to the TPSDM. Site conditions (traffic, environmental impacts, pavement materials properties, and structure) and construction conditions are first considered when proposing a new pavement trial design. The trial design is then evaluated for adequacy by predicting the fatigue life against key distresses. To accomplish this, the following methodological steps have been established, and each is considered a prerequisite for the next step.

(1) This study presents a 3D coupled model of THM processes using the finite element software COMSOL Multiphysics (COMSOL Multiphysics, 2021). Based on a nonlinear elastic model and convergence analysis, the mechanical field is developed within the proposed coupled model. The thermal and hydraulic fields are established by the PDEs (partial differential equations).

(2) This study determines the hydraulic properties of various materials through laboratory experiments, investigates the infiltration behavior of asphalt pavement under rainfall, focuses on the hydraulic properties of the As layer, and compares the applicability of single-phase flow and two-phase flow models to simulate such behavior.

(3) This study uses ODEs (ordinary differential equations) to characterize the physical state of geomaterials and quantify the number of days passed during the recovery period on the element scale.

(4) Modeling the geomaterials with a stress-dependent modulus is a typical coupling problem that involves a circular dependence among resilient modulus, matric suction, temperature, stress, and deformation. This circular dependence can be solved in the WF-PDEs (weak form partial differential equations) to define the stress-dependent modulus.

(5) In a multi-layer elastic model, the structural response results (including stress and strain) can be generated by utilizing the resilient modulus, which is influenced by the stress state and environmental impacts. Based on empirical models, the structural response results (including stress and strain) can then estimate the expected allowable loading number against rutting and fatigue cracking. The method of modifying the rutting failure criterion by incorporating the MEPDG model and the PSAR effect enhances the practicality of the

rutting model. To validate the proposed method, this study conducts a comparative analysis to compare its predictions with those obtained using established pavement design methods.

(6) Field validation is conducted to confirm the effectiveness of the method in real-world scenarios by monitoring pavement moisture content and temperature changes, as well as actual fatigue life and modulus.

1.3 Thesis organization

This dissertation is divided into six chapters.

Chapter 1 introduces the background of this study and the directions for improvement in Japanese theoretical pavement structure design method. The objective, purpose and main technical routes are briefly introduced. The organizational structure of this paper is also outlined.

Chapter 2 provides an overview of several popular prediction models for predicting the resilient modulus of pavement materials, as well as prediction models and their development processes for predicting permanent deformation of pavements. An overview of the THM coupled model used to simulate pavement behavior and the effect of principal stress axis rotation is also provided.

Chapter 3 includes a summary description of important environmental impacts on pavement systems. Basic governing equations describing relevant phenomena are presented in simple form to understand the role played by different contributing factors. Meanwhile, a TH coupled model was established based on soil parameters that were reasonably, simply, and robustly determined through laboratory testing. This model can reproduce the hydraulic and thermal field variations in actual pavement engineering, including ground temperature at different depths, frost-penetration depth, and degree of saturation at different layers.

Chapter 4 designs a physical model experiment to study the infiltration behavior of asphalt pavements under rainfall. After constructing the model experiment, both two-phase flow and single-phase flow models are used to simulate this infiltration behavior. The effectiveness of the numerical model is verified by comparing the numerical simulation results with those of model tests.

Chapter 5 establishes a system for evaluating the environmental impact on the resilient modulus of pavement materials based on the research results from FWD tests, 4PBF tests, and cyclic triaxial tests. Furthermore, a successful method is proposed for determining the physical state of each pavement element using ordinary differential equations in numerical simulations. Through field measurements and comparison with simulated data, the feasibility of the proposed method in predicting the elastic modulus of pavement materials is confirmed.

Chapter 6 replaces the constant elastic modulus of the base layer and subgrade layer with an elastic modulus related to the stress state and complex environmental impacts based on the conclusions of Chapters 3 and 4. Then, the commonly used MEPDG model was considered, and the influence of principal stress axis rotation was considered through multi-ring shear tests to modify the structure of the rutting failure criterion. The applicability of the modified design approach was examined by comparing the predicted fatigue life with the actual measured fatigue performance observed from the test pavement.

Chapter 7 summarizes the findings and conclusions of the study. Recommendations for improving the quality of pavement design are also outlined. Additionally, A brief discussion for improving the fatigue life of pavements is included.

2 LITERATURE REVIEW

Based on the background introduction in the previous chapter, several limitations can be identified in the current TPSDM: assessment of environmental impacts, prediction models for resilient modulus considering factors such as environmental impacts and stress state, and prediction models for fatigue life or permanent deformation. To address these issues comprehensively, this chapter will provide an extensive literature review and investigation.

2.1 Resilient modulus prediction models

This section and the following section provide an overview of the material characteristics and structural layer behavior of geo-materials, which are the primary structural components in pavement systems. It is necessary to thoroughly review the various characterization methods commonly used to simulate the elastic response and permanent deformation behavior of pavement layers in order to facilitate better pavement system design and ultimately ensure adequate performance under repeated moving wheel loads.

In theory, the response of pavement under traffic loads should be purely elastic, such that no permanent deformation accumulates over its service life. Therefore, mechanically based pavement design methods traditionally focus on the elastic response of geo-material layers to predict the critical pavement response under traffic loads. In pavement analysis, the most important input characteristic that describes the repeated load behavior of soil material layers is the "Resilient modulus" (Puppala, 2008). The Resilient modulus, initially proposed by Seed et al. (1955), can capture the influence of stress state on soil stiffness.

Resilient behavior of geo-material can be reasonably characterized by using stress dependent models which express the modulus as nonlinear functions of stress states. Such a characterization model must include in the formulation the two triaxial stress conditions. The currently common resilient modulus prediction models and their development history are shown in Table 2-1

Table 2-1 Summary of resilient modulus prediction models.

Name	Prediction equations
Confining pressure model (Seed et al., 1967)	$M_r = k_1(\sigma_3)^{k_2}$ (2-1)
K- θ model (Monismith et al., 1971)	$M_r = k_1(\theta)^{k_2}$ (2-2)
Shackel model (Shackel, 1973)	$M_r = k_1 \left(\frac{(\tau_{oct})^{k_2}}{(\sigma_{oct})^{k_3}} \right)$ (2-3)
Uzan model (Uzan, 1985)	$M_r = k_1(\theta)^{k_2}(\sigma_d)^{k_3}$ (2-4)
Universal Octahedral shear stress model (Witczak and Uzan, 1988)	$M_r = k_1 p_a \left(\frac{I_1}{p_a} \right)^{k_2} \left(\frac{\tau_{oct}}{p_a} \right)^{k_3}$ (2-5)
Itani model (Itani, 1990)	$M_r = k_1 p_a \left(\frac{\theta}{p_a} \right)^{k_2} (\sigma_d)^{k_3} (\sigma_3)^{k_4}$ (2-6)
Crockford model (Crockford, 1990)	$M_r = k_1 \left(\theta + 3\psi \frac{V_w}{V_t} \right)^{k_2} (\tau_{oct})^{k_3} \left(\frac{\gamma}{\gamma_w} \right)^{k_4}$ (2-7)
UT-Austin model (Pezo, 1993)	$M_r = k_1 (\sigma_d)^{k_2} (\sigma_3)^{k_3}$ (2-8)
Lytton model (Lytton, 1996)	$M_r = k_1 p_a \left(\frac{I_1 - 3f'\theta'\psi}{p_a} \right)^{k_2} \left(\frac{\tau_{oct}}{p_a} \right)^{k_3}$ (2-9)
MEPDG model (NCHRP, 2004)	$M_r = k_1 p_a \left(\frac{\theta}{p_a} \right)^{k_2} \left(\frac{\tau_{oct}}{p_a} + 1 \right)^{k_3}$ (2-10)
Ng model (Ng et al., 2013)	$M_r = k_1 p_a \left(\frac{\theta}{p_a} \right)^{k_2} \left(\frac{\tau_{oct}}{p_a} + 1 \right)^{k_3} \left(\frac{\psi}{\sigma_{net}} + 1 \right)^{k_4}$ (2-11)

where k_1 , k_2 , k_3 and k_4 are regression constants; σ_{oct} is octahedral normal stress; ψ is matric suction; σ_{net} is net mean stress; $\frac{V_w}{V_t}$ is volumetric water content; $\frac{\gamma}{\gamma_w}$ is unit weight of material normalized by the unit weight of water; σ_3 is third principal stress; I_1 is the first stress invariant; f' is saturation factor ($1 < f' < 1/\theta'$); σ_d is deviator stress ($= \sigma_1 - \sigma_3$); θ' is volumetric water content.

It can be seen that scholars currently believe that resilient modulus of geo-materials increases with increasing stress states, especially with confining pressure or bulk stress, and slightly with deviator stress. And more scholars realize that constitutive models that incorporate suction are better able to capture the resilient modulus-suction correlation in actual geo-materials.

2.2 Permanent deformation prediction models

Rutting of permanent deformation is the primary distress mechanism in base course and subgrade layers. Therefore, resistance to rutting is a key performance indicator in designing these foundational layers. At the same time, the permanent deformation of the base course layer and subgrade layer contributes significantly to the overall pavement rutting (Christopher et al., 2006; Dai et al., 2007). The permanent deformation is subject to various factors, including but not limited to the number of load cycles, stress level, stress history, and moisture content. Permanent deformation models for unbound pavement materials are primarily established on the basis of repeated load triaxial tests to characterize permanent deformation behavior. These models can be categorized into two main types: analytical or empirical relationships that depict the variation of permanent strains with the number of load applications and the applied stress, and increment models that are developed from plasticity theory for use in finite element-based calculations (Xiao, 2014). Table 2-2 summarizes well-known examples of the first type, which provide relatively simple and intuitively understandable constitutive relationships to predict the amount of permanent deformation (or strain) at any number of loading applications.

Table 2-2 Summary of permanent deformation prediction models.

Name	Prediction equations
Barksdale model (Barksdale, 1972)	$\varepsilon_p = A + B \log(N)$ (2-12)
Phenomenological model (Monismith et al., 1975)	$\varepsilon_p = AN^B$ (2-13)
Tseng and Lytton model (Tseng and Lytton, 1989)	$\varepsilon_p = \varepsilon_0 e^{-\left(\frac{\rho}{N}\right)^B}$ (2-14)
Paute model (Paute et al., 1996)	$\varepsilon_p = A\left(1 - \left(\frac{N}{100}\right)^{-B}\right)$ (2-15)
Huurman model (Huurman, 1997)	$\varepsilon_p = A\left(\frac{N}{1000}\right)^B + C\left(\exp\left(D\frac{N}{1000}\right) - 1\right)$ (2-16)

$$\begin{array}{l} \text{Ullidetz model} \\ \text{(Ullidetz, 1997)} \end{array} \quad \varepsilon_p = A \left(\frac{\sigma_d}{p_0} \right)^B N^C \quad (2-17)$$

$$\begin{array}{l} \text{MEPDG model} \\ \text{(NCHRP, 2004)} \end{array} \quad \varepsilon_p = \beta_1 K_1 \left(\frac{\varepsilon_0}{\varepsilon_r} \right) e^{-\left(\frac{\rho}{N}\right)^\beta} \varepsilon_v \quad (2-18)$$

$$\begin{array}{l} \text{Wu model} \\ \text{(Wu et al., 2011)} \end{array} \quad \varepsilon_p = \varepsilon_v \cdot A \cdot \left(\frac{(N+1)^{1-B} - 1}{1-B} \right) \quad (2-19)$$

where A , B , C and D are model parameters; p_0 is the normalizing reference stress (often $p_0 = 1$ kPa).

2.3 Environmental impacts and THM coupling simulation

Traffic action can cause fatigue cracking and permanent deformation of weak pavements. But at the same time, "environmental impacts" have been widely used to describe the weak condition because of their non-negligible role. Mechanistic-empirical pavement design methods for flexible pavements are based on the assumption that pavement life is inversely related to the magnitude of the traffic-induced pavement strains. These strains vary with the stiffness of various pavement layers. The stiffness of the asphalt varies with temperature and the stiffness of the unbound base and subgrade materials varies with water content. Because these relationships are nonlinear, the additional pavement life consumed by wheel loads at higher-than-average temperatures or water contents is not offset by savings at lower-than-average temperatures or water contents. Furthermore, the temperature and moisture effects cannot be considered separately and superimposed, they must be considered together (Zuo et al., 2007).

To understand the Thermo-Hydro response of pavements under environmental impacts, there are two approaches: direct experimental testing of moisture and temperature distribution within the soil, and the establishment of mathematical models for numerical simulation to investigate the coupled effect of Thermo-Hydro phenomena. These methods hold significant theoretical and practical implications in predicting various changes in the soil. This section will mainly review numerical simulation research.

The Richards equation developed by Richards in 1931 (Richards, 1931) is considered as the base for modeling water flow through a soil profile. For the thermal-hydro coupled

model of frozen soil, different researchers have proposed theoretical models such as hydrodynamic model (Harlan, 1973), segregation potential model (Konrad and Morgenstern, 1980), and rigid ice model (O'Neill and Miller, 1985) to represent the changes in thermal-hydro characteristics of soil during the freezing and thawing process. This study focuses on the changes in soil water content caused by rainfall and freeze-thaw action, so it mainly reviews the hydrodynamic model. Harlan (1973) proposed a “Hydrodynamic Model” for the interaction between heat and moisture migration in frozen soil by assuming that the water migration law in frozen soil is similar to that of unsaturated soil water movement and combining the mass conservation equation and energy conservation equation. Many scholars use the modifications of Harlan model to study the freezing and thawing process of soil. Hansson et al. (2004) presented a new method to account for phase changes in a fully implicit numerical model for coupled heat transport and variably saturated water flow involving conditions both above and below zero temperature. Dall'Amico et al. (2011) verified the van Genuchten SWCC can be combined with the Clapeyron equation to estimate saturation of liquid water in unsaturated soil subjected to the freezing process.

Accurately predicting the pavement temperature will help pavement engineers to back-calculate the pavement modulus. The ability to predict the temperature and water content distribution of the pavement will aid in evaluating pavement performance. To achieve this, several models have been proposed, such as the EICM (NCHRP, 2004). The limitations of EICM include: (1) the model is one-dimensional, (2) it ignores the coupling effects of different fields. Some other coupled models have been developed for this purpose (Shao et al., 1994; Yavuzturk and Ksaibati, 2002). However, mechanical fields are not coupled in these models. Comprehensive simulation of the impact of coupling effects on pavement mechanics and structural behavior is crucial for pavement fatigue life research.

2.4 Effect of principal stress axis rotation

The MEPDG rutting model does not capture the effect of PSAR, which is a phenomenon caused by moving wheel loads that greatly amplifies the permanent deformation of base and subgrade layers (Gräbe and Clayton, 2009; Inam et al., 2012; Ishikawa et al., 2019b; Ishikawa et al., 2011b; Lekarp and Dawson, 1998; Lin et al., 2019a;

Miura et al., 1986). This because it is based on traditional repeated loading triaxial test with constant confining pressure and no principal stress axis rotation. Ishikawa et al. (2007) developed a multi-ring shear apparatus for laboratory element tests, which could apply cyclic axial stress and shear stress simultaneously. Additionally, the NCHRP Project 4-23 pointed out that shear strength, but not resilient modulus is one of the most significant mechanical properties influencing pavement performance (Saeed et al., 2001). Furthermore, the K-T model (Korkiala-Tanttu, 2009) and UIUC model (Chow et al., 2014) use shear strength to construct a predictive model. As a result, the UIUC model shows high accuracy on permanent strain prediction. Finally, Lin et al. (2019a) used a multi-ring shear device to conduct three tests: monotonic shearing test, cyclic axial loading test, and cyclic axial shear test two kinds of parallel grading aggregate materials, natural crusher-run and recycled crusher-run obtained from demolished concrete structure. Test results show that shear strength is a core factor in permanent deformation behavior compared with resilient properties, while PSAR significantly increases permanent deformation. Not only that, Lin et al. (2021) also introduced an adjustment parameter based on the MEPDG rutting depth prediction model (Equation (2)) to modify the Japanese rutting failure criterion and proposed the ratio of axial strain, estimated with axial stress and shear stress, as a quantitative measure to describe the increase in axial strain caused by PSAR.

3 NUMERICAL SIMULATIONS FOR EVALUATING THE ENVIRONMENTAL IMPACTS

Pavement environment, for the purpose of pavement engineering, refers to the physical processes related to climatic factors that act on a pavement in a given geological and geomorphologic context. This interaction involves climatic factors, soils, and land morphology. Cold region pavement engineering has always been concerned with the study of Thermo-Hydro coupling, and numerical simulation is the best way to apply the achievements of frozen soil physics to practical pavement engineering. Since cold region pavement materials are often in a saturated-unsaturated state, water has an impact on the thermal field. Therefore, it is necessary to establish a Thermo-Hydro coupling model and use various meteorological data as model boundary conditions to analyze the environmental impact on the Thermo-Hydro field of the pavement.

3.1 Numerical simulation assumptions

The scheme of THM coupled model is shown in Figure 3-1. Besides, to establish the THM model, several fundamental assumptions are made, as follows:

The simulation of hydraulic field

The seepage flow of the unfrozen water follows the Darcy's law, and there is no source or drainage in the inner area.

The soil skeleton structure remains unchanged during freezing and thawing without considering frost heave and osmotic pressure for pure water.

The simulation of thermal field

The depression of the freezing point is assumed to be small.

The thermal expansion characteristics of materials are not considered.

The simulation of mechanical field

The pavement materials perform elastic behavior. Each layer is considered to be composed of homogeneous and isotropic material.

The layers are perfectly bound at their interfaces, and the conditions for continuity at the interfaces are satisfied.

The influence of volume strain on the hydraulic field and thermal field is not considered.

The calculation of allowable loading number

The phenomenon of cumulative damage under repeated loads was assumed to be related to the network absorbed by a specimen. The number of loading cycles applied expressed as a percentage of the number to failure at a given stress level would be the proportion of useful life expended. When the total damage, as defined by this concept, reached 100 per cent, the fatigue specimen should fail. (Miner, 1945)

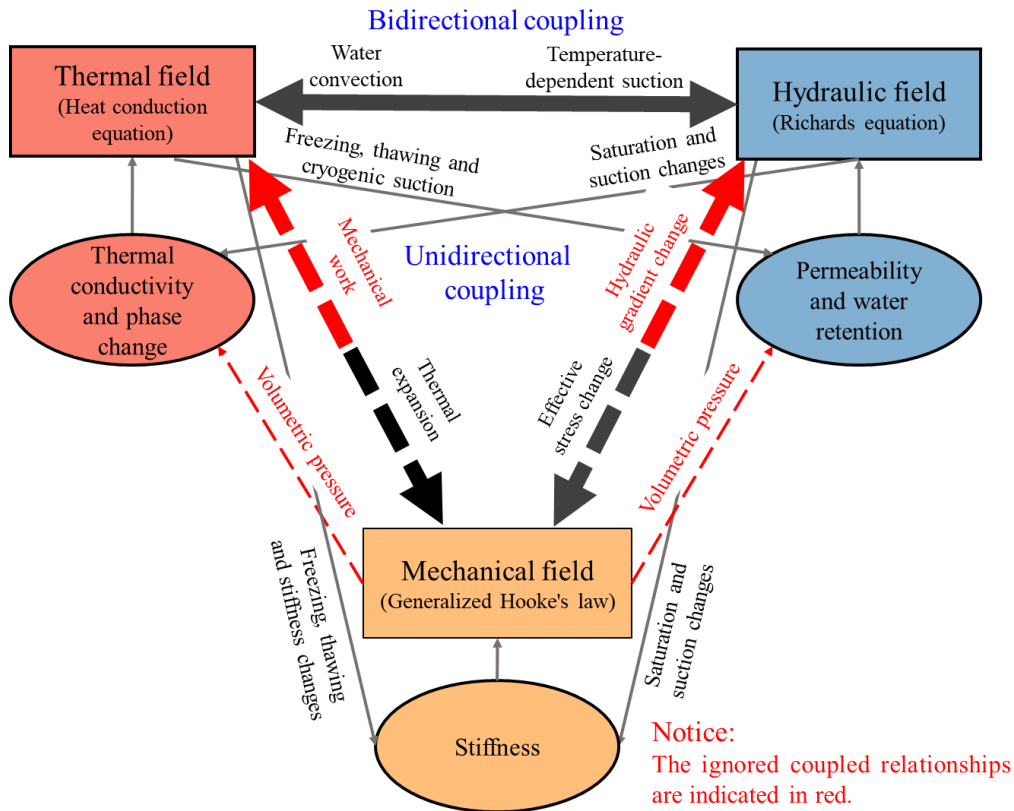


Figure 3-1 Scheme of THM coupled model.

3.2 Governing equations and basic physical parameters

Moisture conditions in pavement systems ensue from the amount of water in soils and pavement materials, its movements, the form under which it occurs, and the phase under which it operates. Like moisture in the air, soil moisture can occur in gaseous, liquid, and solid forms, each significantly modifying the soils properties (Oliver, 1978). Since soils of the base course and subgrade layers of pavement structures are commonly in unsaturated conditions, the unsaturated–saturated seepage flow should be appropriately considered in the hydraulic field. The mass conservation equation can be formulated as Equation (3-1) (Sheppard et al., 1978).

$$C_H \frac{\partial u_w}{\partial t} + \frac{\rho_i}{\rho_w} n \frac{\partial S_i}{\partial t} = \nabla(k_w \nabla h) + f_w \quad (3-1)$$

where C_H is the specific moisture capacity of soil; u_w is the pore-water pressure; k_w is the coefficient of water permeability; h is the total hydraulic potential head which is the sum of the pore-water pressure head and elevation head; n is porosity; ρ_w and ρ_i are the density of water and ice, respectively; S_i is the degree of saturation for ice; t is time; and f_w is the sink/source term of mass.

The left-hand side of Equation (3-1) represents the temporal variation in soil moisture content per unit time. The first term on the right-hand side represents the hydraulic gradient and the change in volume of liquid water caused by gravity, while the second term on the right-hand side represents changes in external sources induced by environmental factors such as precipitation.

The energy conservation equation used in the thermal analysis is as Equation (3-2) (De Vries, 1958):

$$C_{Ta} \frac{\partial T}{\partial t} + L \rho_i n \frac{\partial S_i}{\partial t} + \nabla \cdot (\lambda_T \nabla T) + C_{Tw} \nabla \cdot (\mathbf{v}_w T) = f_e \quad (3-2)$$

where C_{Ta} is the apparent heat capacity of soil; L is the latent heat of fusion of water; λ_T is the thermal conductivity of soil; and C_{Tw} is the volumetric heat capacity of water and \mathbf{v}_w is the flux vector of water; f_e is the sink/source term of energy; and T is temperature.

The left-hand side of Equation (3-2) represents the temporal variation in soil energy, latent heat changes due to phase transition of ice, soil thermal conduction, and convective heat transfer of liquid water per unit time. The right-hand side represents changes in heat source terms caused by meteorological factors such as air temperature and solar radiation.

Generalized Hooke's law can describe the stress–strain relationship of elastic materials, as shown in Equation (3-3) and Equation (3-4) (David M and Lidija, 1999).

$$\{\sigma\} = [D](\{\varepsilon\} - \{\varepsilon_0\}) + \{\sigma_0\} \quad (3-3)$$

$$[D] = \frac{E}{(1+\mu)(1-2\mu)} \begin{bmatrix} 1-\mu & \mu & \mu & 0 & 0 & 0 \\ \mu & 1-\mu & \mu & 0 & 0 & 0 \\ \mu & \mu & 1-\mu & 0 & 0 & 0 \\ 0 & 0 & 0 & \frac{1-2\mu}{2} & 0 & 0 \\ 0 & 0 & 0 & 0 & \frac{1-2\mu}{2} & 0 \\ 0 & 0 & 0 & 0 & 0 & \frac{1-2\mu}{2} \end{bmatrix} \quad (3-4)$$

where $\{\sigma\}$ is the stress tensor; $\{\varepsilon\}$ is the elastic strain tensor; $\{\sigma_0\}$ is the initial stress; $\{\varepsilon_0\}$ is the initial strain; $[D]$ is the stiffness matrix; E is the elastic modulus; and μ is Poisson's ratio.

3.2.1 Hydraulic properties

The soil-water characteristic curve (SWCC) is a curve that represents the relationship between soil water content and matric suction or degree of saturation. It is of great significance for studying water movement in soil. Based on the similarity between soil freezing process and drying process, the SWCC can also be extended to describe the relationship between unfrozen water content and matric suction during freezing process. Regarding the relative permeability of water, the van Genuchten (VG) model is adopted, as shown in Equations (3-5)–(3-6) (Van Genuchten, 1980).

$$k_w = k_{wr} k_s \quad (3-5)$$

$$k_{wr} = (S_e)^{1/2} \left[1 - \left(1 - S_e^{\frac{1}{m}} \right)^m \right]^2 \quad (3-6)$$

$$S_e = \frac{S_r - S_{rr}}{S_{rs} - S_{rr}} = [1 + (\alpha\psi)^\lambda]^{-m} \quad (3-7)$$

where k_s is the permeability of saturated soil; k_{wr} is relative hydraulic conductivity; S_e is the effective degree of saturation; S_r is the degree of saturation; S_{rr} is the residual degree of saturation; S_{rs} is the saturated degree of saturation; α , m , λ are VG model fitting parameters; $m = 1 - 1/\lambda$.

3.2.2 Thermal properties

The method for calculating the effective heat conductivity of the solid–fluid system as the weighted geometric mean of the conductivities of the fluid and the porous matrix is shown in Equation (3-8) (Côté and Konrad, 2005).

$$\lambda_T = (\lambda_s)^{1-n} (\lambda_i)^{\theta_i} (\lambda_w)^{\theta_w} \quad (3-8)$$

where λ_s is the heat conductivity of soil particles; λ_i is the heat conductivity of ice; λ_w is the heat conductivity of water; and θ_w is volumetric water content.

Similarly, the heat capacity of soil is the sum of the volumetric heat capacity of each component weighted by the respective volume, as shown in Equation (3-9) (Johnston et al., 1981).

$$C_{Ta} = (1 - n)C_{Tp} + nS_w C_{Tw} + nS_i C_{Ti} \quad (3-9)$$

where C_{Tp} is the volumetric heat capacity of soil particles and C_{Ti} is the volumetric heat capacity of ice.

3.2.3 SFCC derived from SWCC

The soil freezing characteristic curve (SFCC) is an important property of frozen soils that is required by hydrological models used in cold regions. The curve defines the relationship between unfrozen water content and subzero temperature.

The pressure head decrease obtained during the freezing process can be written as Equation (3-10) (Dall'Amico et al., 2011):

$$\psi = \psi(T) = u_{w0} + \frac{L\rho_w}{T_0}(T - T_0) \quad (3-10)$$

Then, the SWCC of VG model can be combined with the Clapeyron equation to estimate the effective degree of saturation for liquid water in unsaturated soil subjected to freeze–thaw action, as shown in Equation (3-11) (Dall'Amico et al., 2011).

$$S_e = \left[1 + \left(\alpha(u_{w0} + \frac{L\rho_w}{T_0}(T - T_0)) \right)^\lambda \right]^{-m} \quad (3-11)$$

where T_0 is nominal freezing temperature and u_{w0} is pore-water pressure (suction) before freezing.

In this study, the same ice content evaluation model is used as the previous research (Hansson et al., 2004; Liu and Yu, 2011).

When phase changes are involved, the generalized Clapeyron equation (Equation (3-12)) was used to describe the condition for the co-existence of water and ice.

$$\frac{dh}{dT} = \frac{L}{gT} \quad (3-12)$$

where, h is the water head, L is the latent heat of water, and g is gravitational acceleration.

Assuming thermodynamic equilibrium conditions are maintained at the ice-pore/water interface at infinitesimal time intervals, the Clapeyron equation can be used to determine the ice content via Equation (3-13).

$$\frac{d\theta_i}{dT} = \frac{L}{gT} \frac{d\theta}{dh} \quad (3-13)$$

where, θ_i is the volumetric ice content; θ the volumetric water content.

3.3 Analytical procedures

To evaluate the variation of resilient modulus of asphalt pavement depending on the weather conditions in cold regions, a 3D coupled THM FE analysis is conducted following the analytical flow chart shown in Figure 3-2.

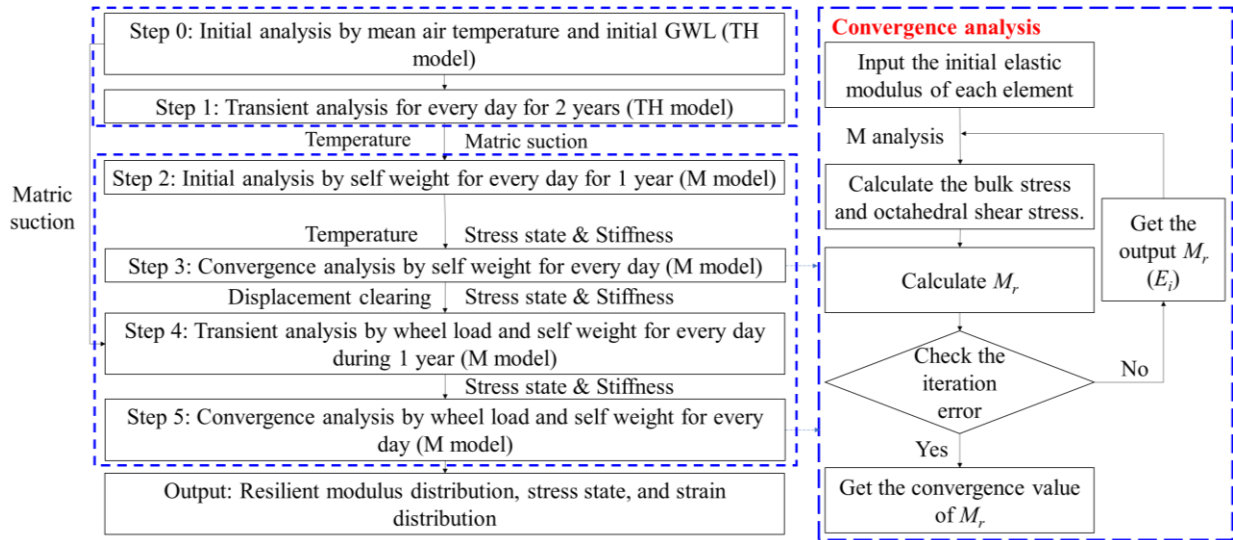


Figure 3-2 Flow chart of THM analysis and convergence analysis.

Among them, modeling the base course layer and subgrade soil with a stress-dependent modulus involves a circular interdependence between the resilient modulus, stress states, and deformation. Therefore, the convergence analysis of M_r is necessary to determine the reliable layer-resilient modulus under a 49-kN wheel load (Lin et al., 2021).

The weak-form PDE-FE presents a significant advantage when addressing a coupling problem that exhibits circular dependence between the inputs of a model and the dependent variables to be resolved. This convergence analysis can be achieved by creating two additional Dependent Variables (DVs) in the WF-PDE to define the stress-dependent modulus. These two DVs will be defined in weak expressions and solved simultaneously with the other three defined DVs (i.e., displacement components) (Zhang et al., 2018b).

3.4 FWD test and field measurement

The FWD is a very useful tool to assess seasonal variations in soil and pavement material properties required to support seasonal damage assessments in pavement design and analysis. In order to comprehend the temporal changes in the bearing capacity of the pavement structure during the thawing season, FWD tests were conducted in accordance with ASTM D4695 (2008) at the same position of the test pavement, 20 times per year from December to March, in 2008 and 2009. The FWD tests utilized a total of six deflection sensors, ranging from the deflection sensor (D_0) directly under the loading plate to the

farthest deflection sensor (D_{150}) at positions of 0, 0.2, 0.3, 0.6, 0.9, and 1.5 m, as shown in Figure 3-3. The measured surface-deflection data from the FWD tests were adjusted for the value under load of 49 kN and temperature of 20°C. The results of the FWD tests were used to estimate the elastic modulus for each layer of the pavement using the static back-analysis program BALM (Back Analysis for Layer Moduli, Matsui et al. 1998). In the back-analysis, it was assumed that the test pavement had a three-layer structure (As layer, base layer, and subgrade layer), in which the subbase course and the anti-frost layer were considered a single layer (Ishikawa et al., 2019a).

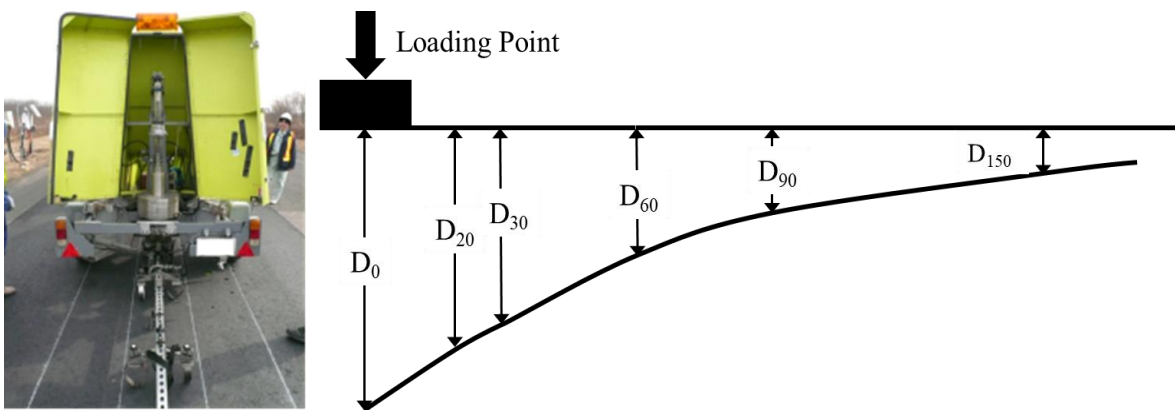


Figure 3-3 FWD testing on test pavement.

Long-term field measurements of ground temperature, soil water content by layer inside the pavement structure were conducted at a test pavement constructed in Hokkaido, Japan in order to examine the relationship between seasonal changes in the freeze/ thaw status or in the water content of pavement structure of each layer.

The test pavement shown in Figure 3-4 is one of typical pavement structures in Hokkaido, in which the top layer of the subgrade is replaced with an anti-frost layer that suppresses frost heave. Figure 3-4 also shows the arrangement of the measuring instruments.

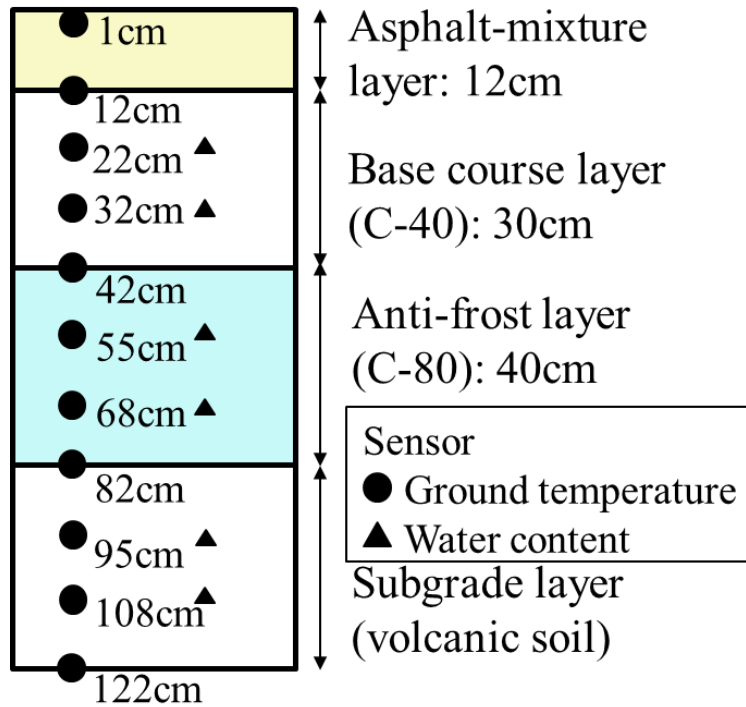


Figure 3-4 Field measurement for ground temperature and water content.

3.5 Numerical model and boundary conditions

The Tomakomai test pavement FE model consists of the asphalt mixture layer (As layer), base course layer (C-40), anti-frost layer (C-80), and subgrade layer. Figure 3-5 shows the size, boundary conditions, and finite element mesh. The inputs required by the environment-related model fall under the following broad categories: (1) Weather-related information (air temperature, precipitation, wind speed, snow depth). (2) Ground water related information. (3) Surface properties. (4) Pavement structure and materials. The time step in simulation is 86.4s.

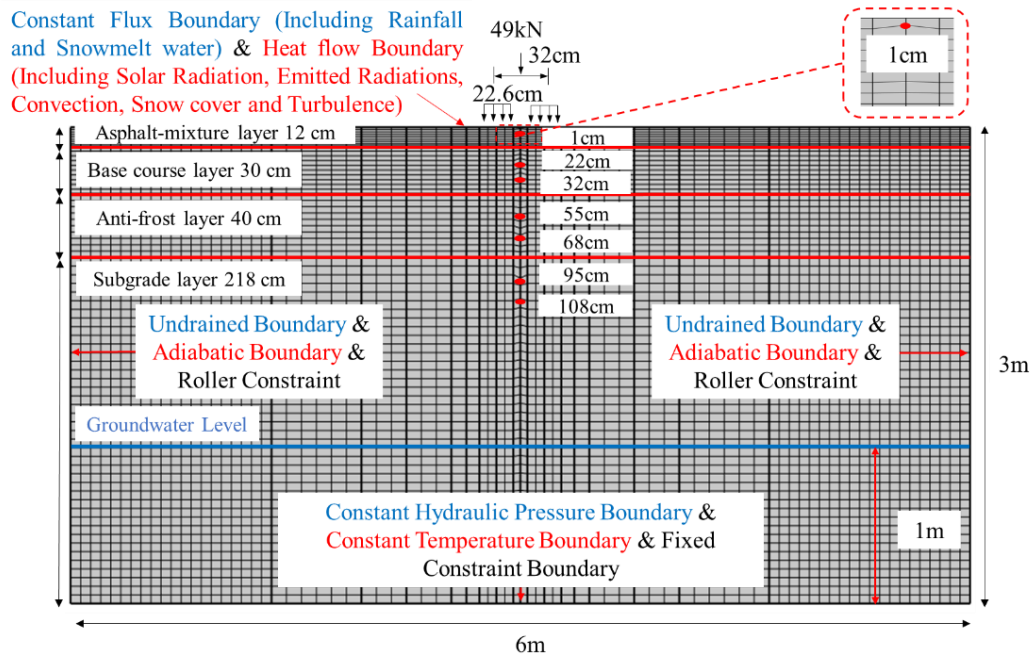


Figure 3-5 Boundary condition and finite element mesh.

In addition, to study the pavement performance and fatigue life the Civil Engineering Research Institute for Cold Region (CERI) designed and constructed eight test pavements in Bibi, Hokkaido (Maruyama et al., 2006). Figure 3-6 illustrates the structures and length of each test pavement. All eight pavement structures consist of asphalt mixture, base layer, and subgrade layer with multiple materials and thickness. Four types of asphalt mixtures are used in test pavement. Fine-graded asphalt mixture has a 0-13 mm gradation distribution. Middle-graded asphalt mixture has the same range of gradation distribution but more coarse aggregate. Coarse-graded and stabilized asphalt mixture have a 0-20 mm and 0-30 mm gradation distribution separately. Two types of base layer material are used as C-40, crusher-run with maximum 40 mm gradation distribution, and C-80, anti-frost crusher-run with maximum 80 mm gradation distribution. The subgrade material is a sandy soil, named as Tomakomai soil, composed of 8% clay, 13% silt, 51% sand, 28% gravel.

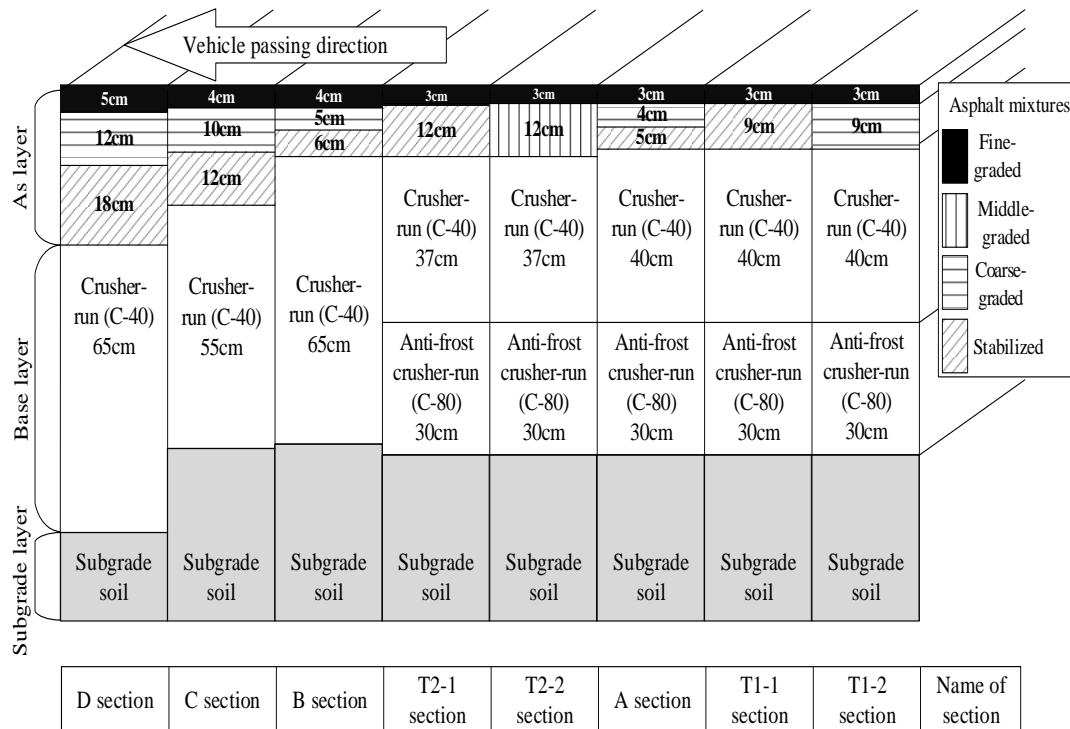


Figure 3-6 The pavement structure of Bibi test pavement.

3.5.1 Estimation of precipitation

As indicated in Figure 3-7, numerous water sources may affect water conditions and, consequently, hydraulic field in pavement systems.

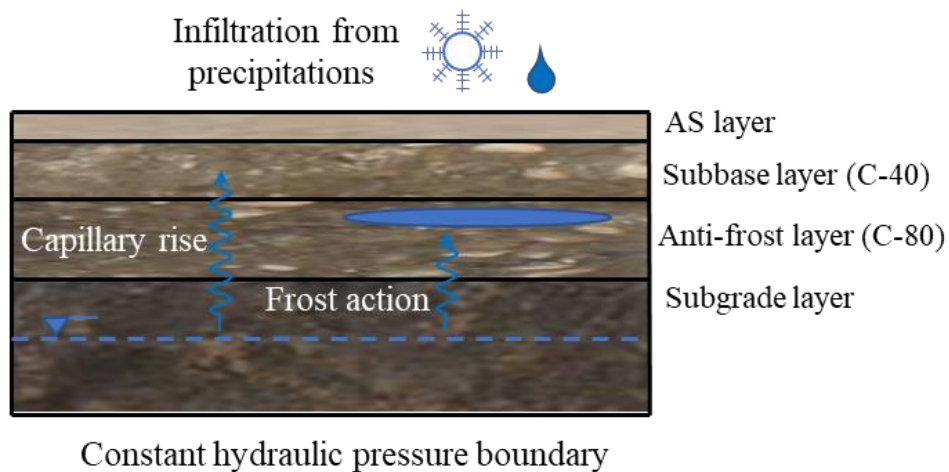


Figure 3-7 Factors affecting hydraulic field in pavements.

The precipitation, as the main reason driving changes in the hydraulic field, is estimated through Equation (3-14) and Equation (3-15) (Murakami et al., 2022).

$$P_{in} = (P_{rain} + SMWE) \quad (3-14)$$

$$SMWE = \frac{\rho_{snow}}{\rho_w} \Delta d_{sn} \quad (3-15)$$

where P_{rain} is rainfall; $SMWE$ is snow-melt water equivalent; ρ_{snow} is snow density; and Δd_{sn} is the value of decreasing snow depth per day.

As for the snow density, Zhu et al. (2021) summarized different models for predicting the snow density and proposed the SY08 (Shinme and Yamashita, 2008)-E86 (Endo, 1986) combination model for calculating snow density in Hokkaido, Japan.

(1) During the midwinter period (SY08 model) (Equation (3-16)):

$$\rho_{snow} = 15.77 \times d_{sn} + 0.11 \times t_2 + 128.1 \quad (3-16)$$

(2) During the early spring period (E86 model) (Equation (3-17)):

$$\rho_{snow} = 239 + 0.861 \times t_1 + 0.01 \times t_1^2 \quad (3-17)$$

where d_{sn} is snow depth; t_1 denotes DOY and t_2 is time in hours measured from the lying snow exist; DOY (DOY is a number from -92 (1st October) to +181 (30th June) and DOY is 1 on 1st January)

3.5.2 Modeling upper and lower surface thermal boundaries

While the temperature regime of a pavement-soil system is influenced by its boundary conditions, it is also impacted by the energy available within the system. Temperature at the top of the system fluctuates significantly between summer highs and winter lows. The temperature of the pavement-soil system is determined by a complex balance that occurs at the interface between the pavement and the air. In this case, the main factors affecting the pavement thermal regime include solar radiation, emitted radiations, convection, and turbulence, as shown in Figure 3-8. This study incorporates these factors when setting the upper surface thermal boundary. It is noted that this study adopted various meteorological data from the Automated Meteorological Data Acquisition System (AMeDAS).

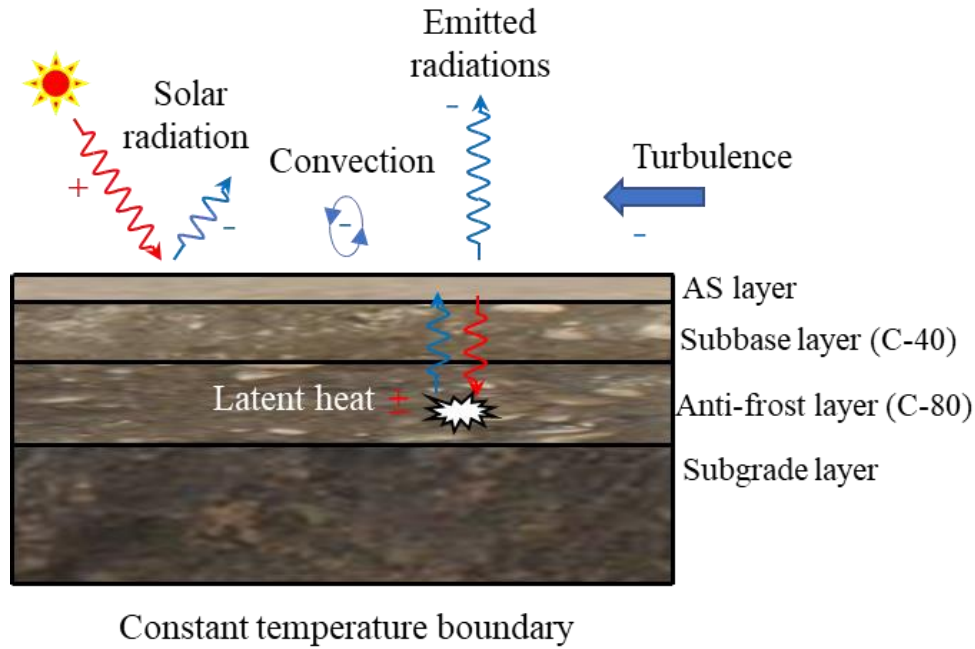


Figure 3-8 Factors affecting thermal field in pavements.

The total solar radiation (Q) received at the surface, shown in Equation (3-18), is the sum of direct and diffuse radiation (Andersland and Ladanyi, 2003).

$$q_s = \alpha_s Q \quad (3-18)$$

where q_s is the net short-wave radiation received and α_s is the absorptivity of the pavement surface to solar radiation, taken as 0.9 in the case of the asphalt mixture or 0.5 in the case of snow cover (Andersland and Ladanyi, 2003).

A perfect radiator emits radiation (q_{er}), and the intensity is proportional to the fourth power of its temperature (T) as predicted by the Stefan–Boltzmann equation (Equation (3-19)) (Doré and Zubeck, 2009):

$$q_{er} = \zeta \epsilon_s (T_s^4 - T_a^4) \quad (3-19)$$

where ζ is the Stefan–Boltzmann constant ($5.67 \times 10^{-8} \text{ W/m}^2 \text{ K}^4$); ϵ_s is surface emissivity, taken as 0.9 in case of the asphalt mixture (Doré and Zubeck, 2009); and T_s and T_a are the temperatures of the surface and the atmosphere, respectively.

Convection, which necessitates the presence of moving fluid like air, is an additional crucial mechanism that contributes to the removal of heat from pavement surfaces. To

extract heat from the pavement surface, it must initially be transferred to a thin film of air via conduction and radiation. The temperature discrepancy between the heated thin film of air and the surrounding air mass induces a pressure discrepancy, which in turn triggers air mass movement. The heat will then relocate and dissipate. The presence of wind-induced turbulence will increase the fluid's motion and its capacity for dispersion. Heat extraction by convection (q_c) is a function of the temperature difference between the ground surface and the atmosphere, as expressed in Equation (3-20) (Doré and Zubeck, 2009).

$$q_c = h_c(T_s - T_a) \quad (3-20)$$

where h_c is the convective heat transfer coefficient.

The coefficient h_c is a function of the surface drag coefficient, air density, specific heat of air, air Prandtl number, and wind speed. Due to the difficulty of measuring or determining these parameters, Zarling and Braley (1988) have proposed the following dimensional relationship (Equation (3-21)) to determine the convective heat transfer coefficient for a smooth surface as a function of wind speed:

$$h_c = 5.678 + 1.056U \quad (3-21)$$

where U is wind speed. From Equation (3-19), it can be inferred that the convective heat flux will double if wind speed goes from 0 to 5 km/h.

The energy flux through the snow (q_{sn}) when there is snow cover on the ground is estimated using Equation (3-22) (Bras, 1990).

$$q_{sn} = -\lambda_{sn} \frac{(T_s - T_a)}{d_{sn}} \quad (3-22)$$

where λ_{sn} is the thermal conductivity of snow cover, taken as 0.255 W/m·°C (Takeichi et al., 1987).

On the other hand, this study assumes that the heat flow from inside the earth is negligible. Then, the temperature (T_z) at the depth of the lower surface thermal boundary (z) can be calculated as Equation (3-23) and Equation (3-24) (Andersland and Ladanyi, 2003):

$$T_z = T_m + A_z \cdot \exp\left(-z \sqrt{\frac{\pi}{\alpha_u p_d}}\right) \cdot \sin\left(\frac{2\pi t}{p_d} + \varphi - z \sqrt{\frac{\pi}{\alpha_u p_d}}\right) \quad (3-23)$$

$$\alpha_u = \frac{\pi}{p_h} \left[\frac{z_2 - z_1}{\ln\left(\frac{A_{z1}}{A_{z2}}\right)} \right]^2 = \frac{\pi}{8,766h} \left[\frac{1.22 - 0.95}{\ln\left(\frac{24.52}{21.96}\right)} \right]^2 = 5.17 \times 10^{-2} \text{ m}^2/\text{day} \quad (3-24)$$

where T_m is the mean annual ground surface temperature; A_z is the ground surface temperature amplitude; φ is the initial phase; p_d is the period (365 days); z is the depth of the lower surface thermal boundary, set as 3 m in this study; and α_u is the thermal diffusivity, $5.17 \times 10^{-2} \text{ m}^2/\text{day}$ (Andersland and Ladanyi, 2003); z_1, z_2 is the depth; A_{z1}, A_{z2} is the observed annual temperature range, as shown in Table 3-1.

Table 3-1 Measured Ground Temperature.

	Depth/cm	
	122	95
Maximum temperature/°C	22.93	24.95
Minimum temperature/°C	0.97	0.43
Observed annual temperature range/°C	21.96	24.52

3.6 Material properties and input parameters

The material input parameters used in this study are listed in Table 3-2. For all layers, the soil parameters are determined reasonably simply and robustly from laboratory tests. The parameters in Equation (3-5) to Equation (3-7) were obtained through parameter fitting and based on the water retention and permeability test data (Furuki et al., 2022; Kaneko et al., 2021; Ren et al., 2023). The thermal conductivity and volumetric heat capacity are based on the thermal properties test (Pavement Engineering Committee, 2016). The dry density of soil, porosity, and Poisson's ratio are based on the field surveys.

Table 3-2 Material input parameters in TH analysis.

Parameters	Unit	As Layer	Base Course Layer	Anti-Frost Layer	Subgrade Layer
Thermal conductivity (λ_T)	W/m·°C	1.45	2.51	2.13	1.61
Dry density of soil (ρ_d)	kg/m ³	2400	1800	1800	1200
Saturated degree of saturation (S_{rs})	%	100	100	100	100

Residual degree of saturation (S_{rr})	%	20	32.30	32.30	25.41
Poisson's ratio (μ)	-	0.35	0.35	0.35	0.4
van Genuchten fitting parameter (α)	1/kPa	2.33	12.17	12.17	0.985
van Genuchten fitting parameter (λ)	-	1.94	1.56	1.56	1.71
Permeability of saturated soil (k_s)	m/s	1.5×10^{-4}	1.0×10^{-3}	1.0×10^{-3}	1.72×10^{-7}
Volumetric heat capacity of soil particles (C_{Tp})	J/m ³ ·°C	1.8×10^6	1.8×10^6	1.8×10^6	0.86×10^6
Porosity (n)	-	0.07	0.24	0.24	0.55

3.7 Comparison results between simulation and measurement

Figure 3-9 compares ground temperature changes at different depths obtained through FE simulation and measurement data. From Figure 3-9, it is revealed that the fluctuation in ground temperature becomes remarkable at the shallow part of pavement structure. This indicates that the closer to the ground, the more significant the environmental impacts on the ground temperature. From comparing the ground temperature and freezing duration between simulation results and measurement data, it is recognized that the annual change in the ground temperatures obtained from the proposed FE simulation is almost consistent with the measured results, irrespective of the ground depth.

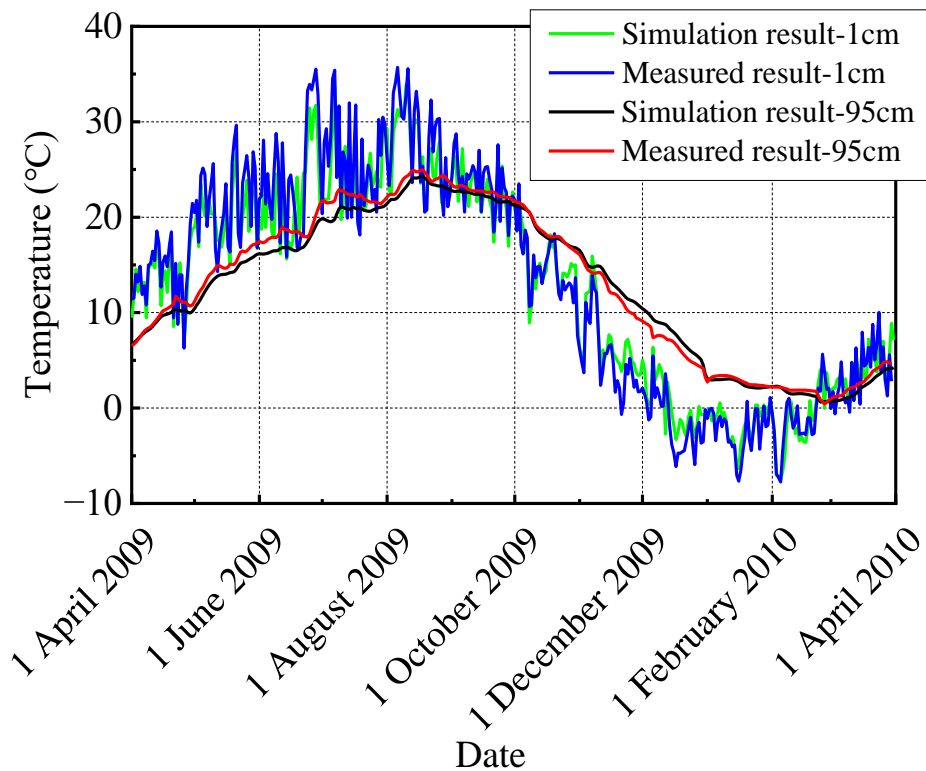


Figure 3-9 Ground temperature at different depths.

Figure 3-10 compares the variation of frost-penetration depth with time between the measurement data and the simulation results. Here, the frost-penetration depths of both measurements and simulations were estimated by the linear interpolation of ground temperatures at the adjacent depths at a position of 0 °C isotherm. The frost-penetration depth reached the anti-frost layer in 2009 and decreased dramatically as the temperature rose, starting in March. It is seen that the FE simulation poorly reproduces the measured frost-penetration depth as compared to the ground temperature. A reason for this is that when the ground temperature becomes close to 0 °C the linear interpolation is not precise. Meanwhile, Figure 3-10 shows the changes in the frost penetration depth under three other conditions: dry conditions, saturated conditions, and static water content distribution (water content distribution controlled by groundwater level). It can be seen from Figure 3-10 that there is little change in the frost penetration depth between the static water content distribution and the dynamic water content distribution. However, in dry conditions, the change in frost penetration depth is more significant due to the smaller heat capacity and no latent heat effect. If water content distribution is not considered, the frost penetration

depth will be overestimated during the cooling process and underestimated during the warming process. The comparison results in the thermal field indicate that the proposed FE simulation is reliable for estimating the thermal field of the asphalt pavement.

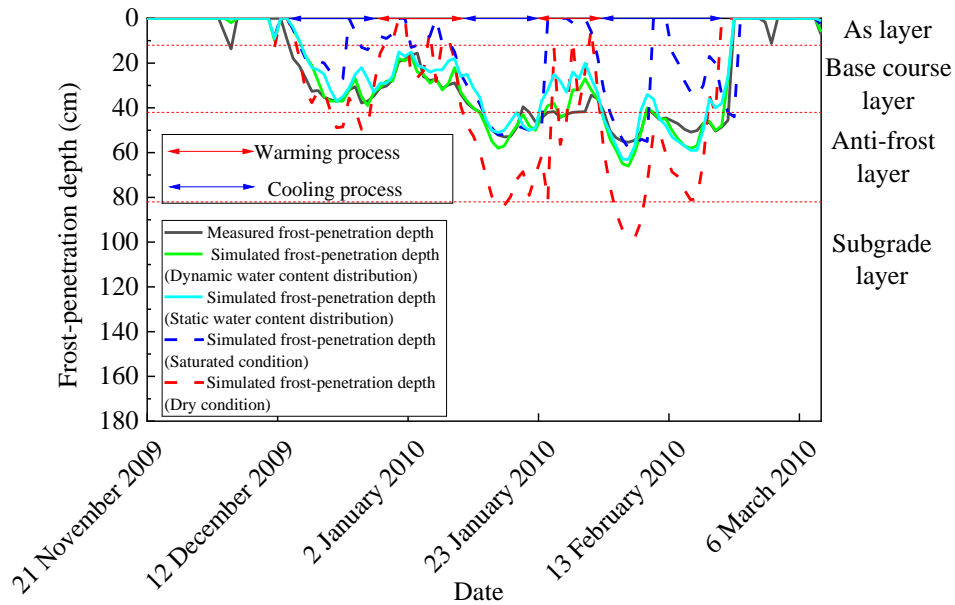


Figure 3-10 Frost-penetration depth curve over time.

Furthermore, as shown in Figure 3-11, there is a noticeable trend of the degree of saturation of the base course layer rapidly decreasing after late December 2009. This is due to the freezing of pore water at a ground temperature lower than the freezing temperature. During the thawing season in March, the water accumulated by frost heave during winter and snowmelt water contribute to high moisture levels in the pavement structure. This change in water content, observed from the regular season to the thawing season, significantly affects the mechanical behavior of the base course and subgrade layers. After rainfall events, liquid water migration is significantly increased, leading to a dominance of liquid water infiltration. The comparison results in Figure 3-11 in the hydraulic field demonstrate the high reliability of the proposed finite element simulation to evaluate the infiltration behavior of the asphalt pavement.

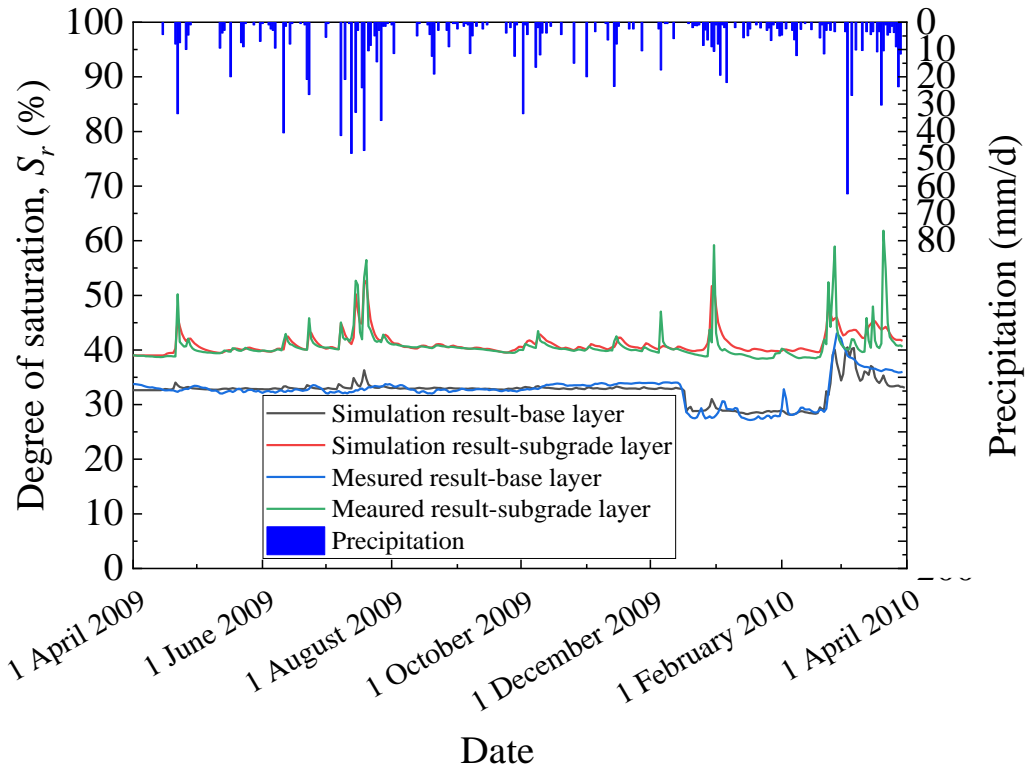


Figure 3-11 Degree of saturation curve over time.

According to Figure 3-11, the moisture balance over time can be categorized into four distinct seasons.

In autumn, heavier precipitation and reduced evaporation at the pavement surface lead to a slight increase in moisture content during October and November. At the end of November, interstitial water freezes due to freezing temperatures, which can be considered the start of winter for pavement engineering purposes. At the beginning of winter, the unfrozen water content of the base course layer decreases. In comparison to the base course layer, the subgrade soil process occurs less conspicuously. Due to limitations in measuring instruments that typically measure unfrozen water content in soils rather than total water content.

The moisture balance fluctuates the most during spring. During this season, water accumulated during winter is released over a relatively short period of time, as indicated by the sharp rise in unfrozen water content in the base and subgrade soils. Additionally, precipitation and snow melting contribute to high moisture contents in the system through

infiltration. Excess water in the system will progressively drain out of the system in late spring and early summer seasons.

During summer, residual excess moisture in the pavement system will continue to drain. Although intense precipitation may temporarily affect moisture balance, as observed in July in Figure 3-11, the effect of that specific precipitation event is more noticeable in the subgrade soil than in the pavement base.

In general, the moisture field in pavements has a significant impact on its response to temperature variations and external stresses. Optimal pavement performance requires low moisture contents with minimal fluctuations throughout the year.

3.8 Summary

This chapter includes a summary description of important environmental impacts on pavement systems. Basic governing equations describing relevant phenomena are presented in simple form to understand the role played by different contributing factors. Meanwhile, a TH coupled model was established based on soil parameters that were reasonably, simply, and robustly determined through laboratory testing. This model aims to reproduce the hydraulic and thermal field variations in real pavement engineering, including ground temperature at different depths, frost-penetration depth, and degree of saturation at different layers. The mainly findings of the chapter are as follows:

- (1) A comparison between ground temperature changes at different depths obtained through FE simulation and measurement data shows that the fluctuation in ground temperature is more significant at the shallow part of the pavement structure. This indicates that the closer to the ground, the more significant the environmental impacts on the ground temperature.
- (2) There is little change in the frost penetration depth between the static water content distribution and the dynamic water content distribution. However, in dry conditions, the change in frost penetration depth is more significant due to the smaller heat capacity and no latent heat effect. If water content distribution is not considered, the frost penetration depth will be overestimated during the cooling process and underestimated during the warming process.

- (3) Due to the freezing of pore water at a ground temperature lower than the freezing temperature, there is a noticeable trend of the degree of saturation of the base course layer rapidly decreasing after late December 2009. During the thawing season in March, the water accumulated by frost heave during winter and snowmelt water contribute to high moisture levels in the pavement structure. This change in water content, observed from the regular season to the thawing season, significantly affects the mechanical behavior of the base course and subgrade layers. After rainfall events, liquid water migration is significantly increased, leading to a dominance of liquid water infiltration.
- (4) From the comparison of the ground temperature, freezing duration, frost-penetration depth, and degree of saturation between simulation results and measurement data, the proposed THM simulation method could reasonably reproduce the changes in temperature and water content in the asphalt pavement, which is the prerequisite for accurately predicting the resilient modulus.
- (5) The moisture field in pavements has a significant impact on its response to temperature variations and external stresses. Optimal pavement performance requires low moisture contents with minimal fluctuations throughout the year.

4 PAVEMENT INFILTRATION BEHAVIOR CONSIDERING HYDRAULIC PROPERTIES OF AS LAYER

Current Japanese pavement design guide and MEPDG do not consider the pavement infiltration behavior considering the hydraulic properties of As layer. In this chapter, a physical model experiment is designed and constructed to study the infiltration behavior of asphalt pavements under rainfall. After constructing the model experiment, both two-phase flow and single-phase flow models are used to simulate this infiltration behavior. The physical model experiment and coupled analysis provide references for studying the application of asphalt hydraulic properties in pavement engineering.

4.1 Experimental modeling

4.1.1 Design of the model test

In this study, a two-dimensional soil tank model was used for rainfall experiments. The upper layer of the soil tank was made of asphalt mixture, and the lower layer was made of C-40. The lower layer material used air-dried C-40 as the sample, which was divided into three layers and compacted using a vibrator to achieve a degree of compaction of D_c above 93%. After compacting the second layer, three EC-5 moisture meters was buried in it. Since water easily penetrates between the acrylic plates and the material in the soil tank, grease was applied to the side of the material before the experiment to prevent this from happening. There was a small gap between the asphalt material and the side of the tank, so before the experiment, oil-based clay or grease was used to fill the gap to prevent water leakage. After building the two layers of material, a rainfall simulator was installed above the soil tank to simulate rainfall. At this time, the rainfall intensity output by the rainfall simulator was set to 1.5 mm/h by adjusting the water level in the overflow tank in advance (Figure 4-2).

In order to collect water flowing out of the drainage slots on the side of the soil tank, a container was set up in the drainage area, and the experiment lasted for 24 hours. A fixed-

point camera was installed to observe the water movement on the front of the soil tank (Figure 4-1). In addition, to record changes in saturation and volumetric water content measured by the moisture meters, a data recording device automatically recorded the voltage value of the soil moisture meters every 10 minutes during the test period.

4.1.2 Model Testing Apparatus

The test apparatus used in this study is shown in Figure 4-1 and Figure 4-2. The soil tank has a length of 550 mm, a width of 150 mm, and can be used to construct a model pavement with a height of up to 380 mm. In addition, because it is surrounded by a 20-mm-thick acrylic plate (semi-transparent), the infiltrating water flow into the pavement can be observed from the front. To maintain a constant rainfall intensity, an overflow tank is utilized for simulating rainfall.



Figure 4-1 Front view of the test apparatus.

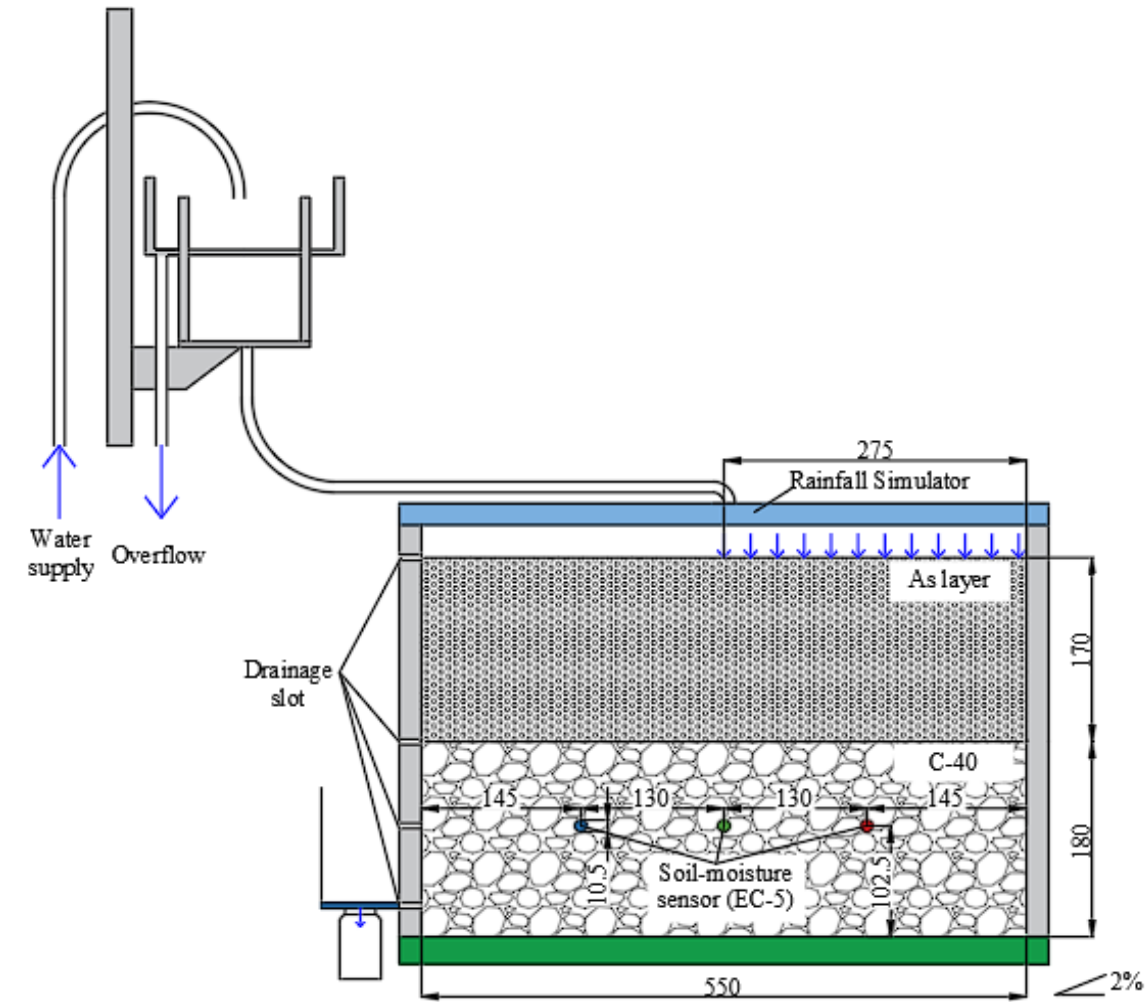


Figure 4-2 Schematic diagram of the test apparatus (Unit: mm).

4.1.3 Materials of model test

Two types of materials were used in this model test, among which the particle size distribution curves for the asphalt mixture and C-40 are shown in Figure 4-3. All materials were kept dry before the test.

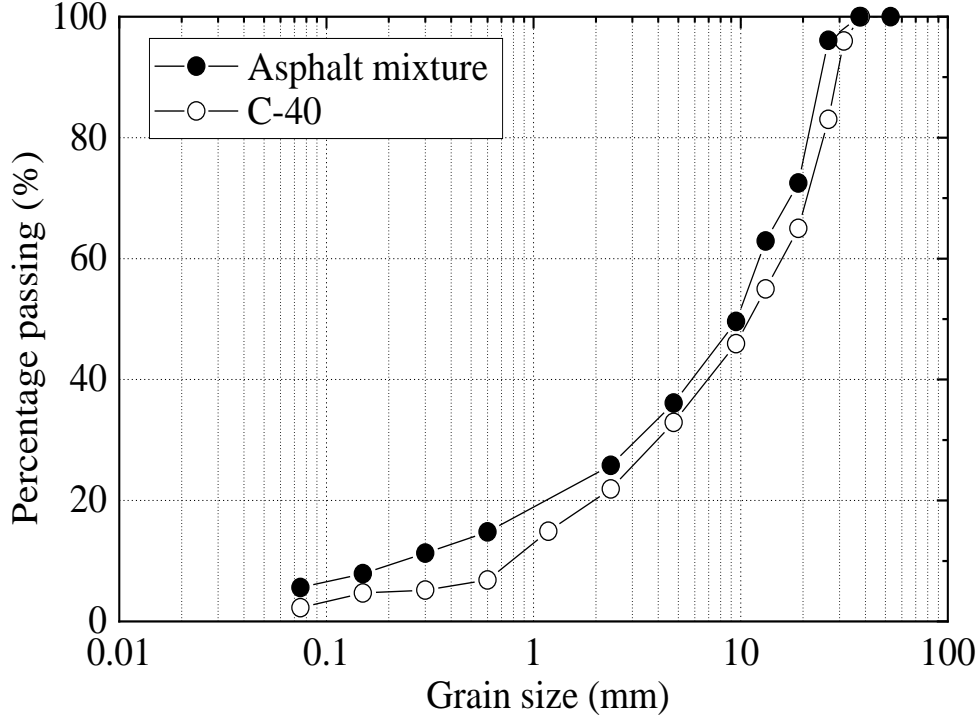


Figure 4-3 Grain size distribution of testing material.

4.2 Numerical simulation

4.2.1 Governing equations for two-phase flow in porous media

Two-phase flow in porous media follows separate equations for the wetting (water) and nonwetting (air) fluids, as show in Equation (4-1) and Equation (4-2).

$$(\theta_s - \theta_r) \frac{\partial S_{e,w}}{\partial t} + \nabla \cdot \left[-\frac{\kappa_{int} k_{r,w}}{v_w} \nabla (p_w + \rho_w g \nabla D_{x,y}) \right] = 0 \quad (4-1)$$

$$(\theta_s - \theta_r) \frac{\partial S_{e,g}}{\partial t} + \nabla \cdot \left[-\frac{\kappa_{int} k_{r,nw}}{v_g} \nabla (p_g + \rho_g g \nabla D_{x,y}) \right] = 0 \quad (4-2)$$

where θ_s is the total porosity or saturated volume fraction; θ_r is the residual volume fraction, so the difference $(\theta_s - \theta_r)$ is the available pore space for phases to move; $S_{e,w}$ and $S_{e,g}$ are the effective saturation of water and air, respectively; κ_{int} is the intrinsic permeability of a given porous medium; $k_{r,w}$ and $k_{r,g}$ are the relative permeability of water and air, respectively; v_w and v_g are the dynamic viscosity of water and air, respectively; p_w and p_g are pressure of water and air, respectively; ρ_g is density of air; and $D_{x,y}$ is the coordinate (for example, x, y) of vertical elevation.

Capillary pressure (p_c) is typically defined as the pressure difference between the non-wetting (air) and wetting (water) phases. In simulation and experimental processes, it is often convenient to express capillary pressure in terms of pressure head (h_c), as shown in Equation (4-3). However, when deriving coupled governing equations for two-phase flow, it is important to consider that both air and water are subjected to their respective pressure controls. This transformation requires careful attention to density differences.

$$h_c = (p_g - p_w) / \rho_w g = h_g - h_w \quad (4-3)$$

The available pore space can be filled with a fluid at a given time, which is related to the effective saturation of each phase, as shown in Equation (4-4).

$$S_{e,w} + S_{e,g} = 1 \quad (4-4)$$

The specific capacity of water depends on the variation of effective saturation relative to capillary pressure head. Similarly, the specific capacity of air, C_G is defined in Equation (4-5).

$$C_G = (\theta_s - \theta_r) \frac{\partial(1-S_{e,w})}{\partial h_c} = -C_H \quad (4-5)$$

Using Equation (4-3), Equation (4-4), and Equation (4-5) in Equation (4-1) and Equation (4-2) simplifies the numerical model. The governing equations become Equation (4-6) and Equation (4-7).

$$C_H \frac{\partial}{\partial t} h_w + \nabla [-k_{ws} k_{r,w} (\nabla h_w + \nabla D)] = C_H \frac{\partial}{\partial t} h_g \quad (4-6)$$

$$C_H \frac{\partial}{\partial t} h_g + \nabla \left[-k_{gs} k_{r,g} \left(\frac{\rho_w}{\rho_g} \nabla h_g + \nabla D \right) \right] = C_H \frac{\partial}{\partial t} h_w \quad (4-7)$$

where, k_{ws} and k_{gs} are the saturated coefficient of permeability of water and dry air permeability, respectively.

4.2.2 Retention and permeability relationships

Similar to the VG model (Van Genuchten, 1980) for single-phase flow, the two-phase flow model also adopts a VG model to express the relationship between retention and permeability. The differences are: 1. In two-phase flow, the independent variable is the matric suction considering the change of air pressure, i.e., $(h_g - h_w)$. 2. The retention and

permeability relationships of air and water are different. Equation (4-8) and Equation (4-9) shows the hydraulic properties relative to the wetting fluid (water) in VG model.

$$S_{e,w} = \begin{cases} [1 + |\alpha h_c|^\lambda]^{-m} & h_c > 0 \\ 1 & h_c \leq 0 \end{cases} \quad (4-8)$$

$$k_{wr} = (S_{e,w})^{1/2} \left[1 - \left(1 - (S_{e,w})^{\frac{1}{m}} \right)^m \right]^2 \quad (4-9)$$

For the nonwetting fluid (air), the properties arise from the definitions for the wetting phase (water), as shown in Equation (4-10) to Equation (4-11).

$$S_{e,g} = 1 - S_{e,w} \quad (4-10)$$

$$k_{gr} = (1 - S_{e,w})^{1/2} \left(1 - (S_{e,w})^{\frac{1}{m'}} \right)^{m'} \quad (4-11)$$

where m' is a curve fitting parameter related to pore-size distribution, which is assumed to be 2.9 (Fredlund et al., 2012).

4.2.3 Intrinsic permeability

For the governing equations, there is still an important variable to be determined, which is the dry air permeability. In fact, the intrinsic permeability is used to predict the dry air permeability of each material (Zhang and Ke, 2017). Intrinsic permeability is a fluid flow property related to the nature of a porous medium. Intrinsic permeability is computed by taking the properties of the pore fluid into consideration. Bear (1972) called intrinsic permeability the “medium’s permeability” and described it as “an average (or macroscopic) medium property that measures the ability of the porous medium to transmit fluid through it.” The mathematical relationship between intrinsic permeability and hydraulic conductivity can be written as Equation (4-12):

$$k = \frac{\rho' g}{\nu} K \quad (4-12)$$

where g is gravitational acceleration; ρ' is density; ν is dynamic viscosity of the fluid.

Intrinsic permeability can be used to convert flow properties used in one discipline (e.g., geotechnical engineering) to flow properties used in another discipline (e.g., petroleum and soil science disciplines). The concept of intrinsic permeability also has an

important role to play in unsaturated soil mechanics. For example, the measurement of saturated water coefficient of permeability can be used to calculate a value for air coefficient of permeability for a dry soil at the same void ratio. Or vice versa, air flow measurements in the laboratory or field on a dry soil can be used to compute saturated coefficient of permeability. Saturated soil water coefficient of permeability measurements can also be used in conjunction with a SWCC to estimate the air permeability function for an unsaturated soil. The properties of the pore fluid can provide an estimate of the relative ease with which air and water can flow through a soil (Fredlund et al., 2012).

Assuming that the soil skeleton is not affected by suction changes and ignoring the Klinkenberg effect, the permeability of either the water phase or the air phase only depends on the ratio of the phase in the porosity of the material. Based on the concept of intrinsic permeability (Equation (4-12)), calculating the saturated water permeability and the maximum air permeability at the dry state are the same. A relationship exists between the coefficients of water phase and air phase permeability. Hence the dry air permeability can be calculated from the saturated coefficient of permeability of water.

Since the intrinsic permeability is a constant, the flow volumes of air and water can be compared. Using the dynamic viscosity corresponding to 20°C, the volumetric flow rate of air will be 56.4 times that of water, as shown in Equation (4-13).

$$\frac{Q_g}{Q_w} = \frac{v_w}{v_g} = \frac{1.009}{0.0179} = 56.4 \quad (4-13)$$

where Q_w and Q_g are the volumetric flow rate of water and air, respectively.

The ratio of dry air permeability to saturated coefficient of permeability of water must take into consideration the relative densities of air and water. The ratio of dry air permeability to saturated coefficient of permeability of water corresponding to 20°C and standard pressure (i.e., 101.3 kPa) is shown in Equation (4-14)

$$\frac{k_{gs}}{k_{ws}} = \frac{\rho_g v_w}{v_g \rho_w} = \frac{1.196}{0.0179} \frac{1.009}{998.2} = \frac{1}{14.8} \quad (4-14)$$

Equation (4-14) shows that the dry air permeability is 14.8 times smaller than saturated coefficient of permeability of water. The information from Equation (4-13) and Equation (4-14) may initially appear to be contradictory. This may be the reason why seemingly

contradictory statements about the ease of air and water flow through soils are often encountered in the literature.

4.2.4 Numerical model and boundary conditions

The numerical model was developed based on the 2D soil tank model test conducted in this study. Figure 4-4 shows the model size, finite element mesh, and boundary conditions. The soil tank is divided into an As layer ($h=170$ mm) and a base course layer ($h=180$ mm), with a model width of 550 mm and a slope angle of 2% as specified in Japanese pavement design standard.

As shown in Figure 4-4, five types of boundary conditions were used to simulate the model test. There are four drainage slots in the soil tank, located on the left boundary of the model, which are set as permeable boundaries (water) and atmosphere boundaries (air) in the simulation. The upper boundary is set as an atmosphere boundary (air), and the upper right boundary is set as a flux boundary (water). The remaining boundaries are impermeable boundaries (water and air). The time step in simulation is 3.6s. In addition, since the experimental materials were in a dry state before the experiment, the initial state of the model was set to the matric suction corresponding to the dry state of the material.

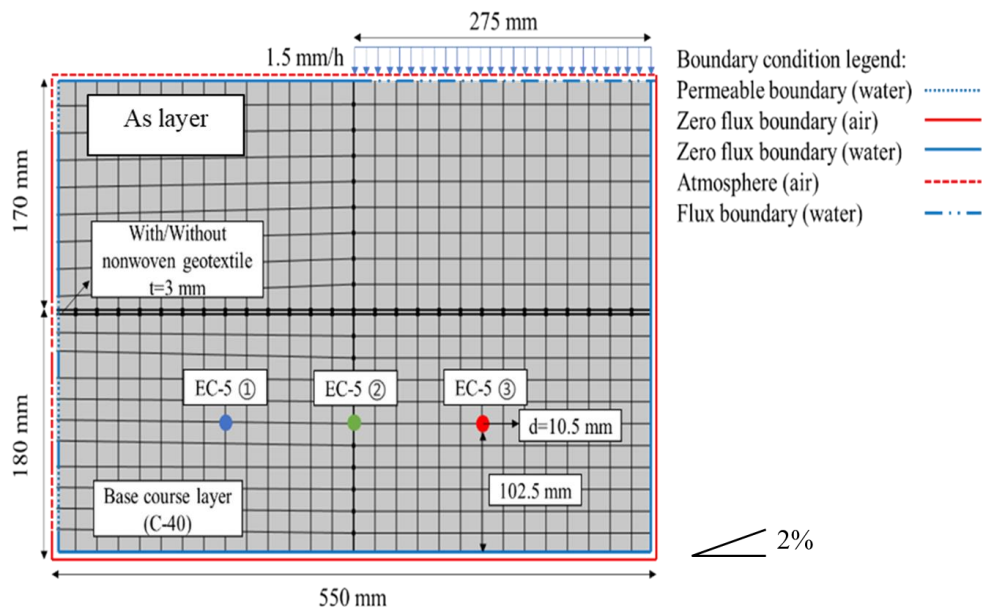


Figure 4-4 Boundary condition and finite element mesh for model test.

4.2.1 Material properties for the verification

According to Table 4-1, in this study, the SWCC fitting parameters and unsaturated hydraulic conductivity of each material were analyzed based on the laboratory test results. In particular, the SWCC of the asphalt mixture used in the study is shown in Figure 4-5.

Table 4-1 Material input parameters in two-phase flow analysis.

Parameters	Unit	As Layer	Base Course Layer
Porosity (n)	-	0.07	0.24
van Genuchten fitting parameter (α)	1/kPa	1.98	12.17
van Genuchten fitting parameter (λ)	-	3.32	1.56
Permeability of saturated soil (k_s)	m/s	2.8×10^{-4}	1.01×10^{-3}
Residual volumetric water content (θ_r)	-	0.007	0.059

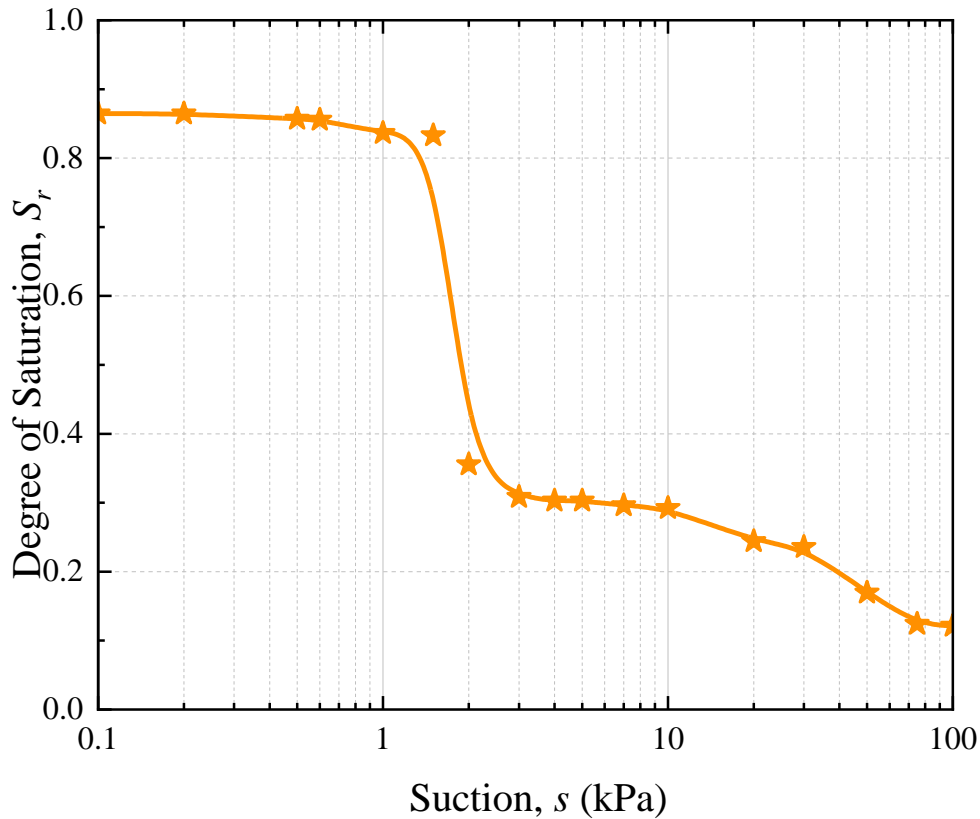


Figure 4-5 SWCC of asphalt mixture.

4.3 Comparison results between simulation and measurement

Figure 4-6 illustrates the evolution of the moisture front over time in both simulation and model tests. From the comparison results, it can be seen that numerical simulation can better simulate the trend of the wetting front, but due to the non-uniformity of materials, there is a certain deviation between the simulated and discrete experimental results.

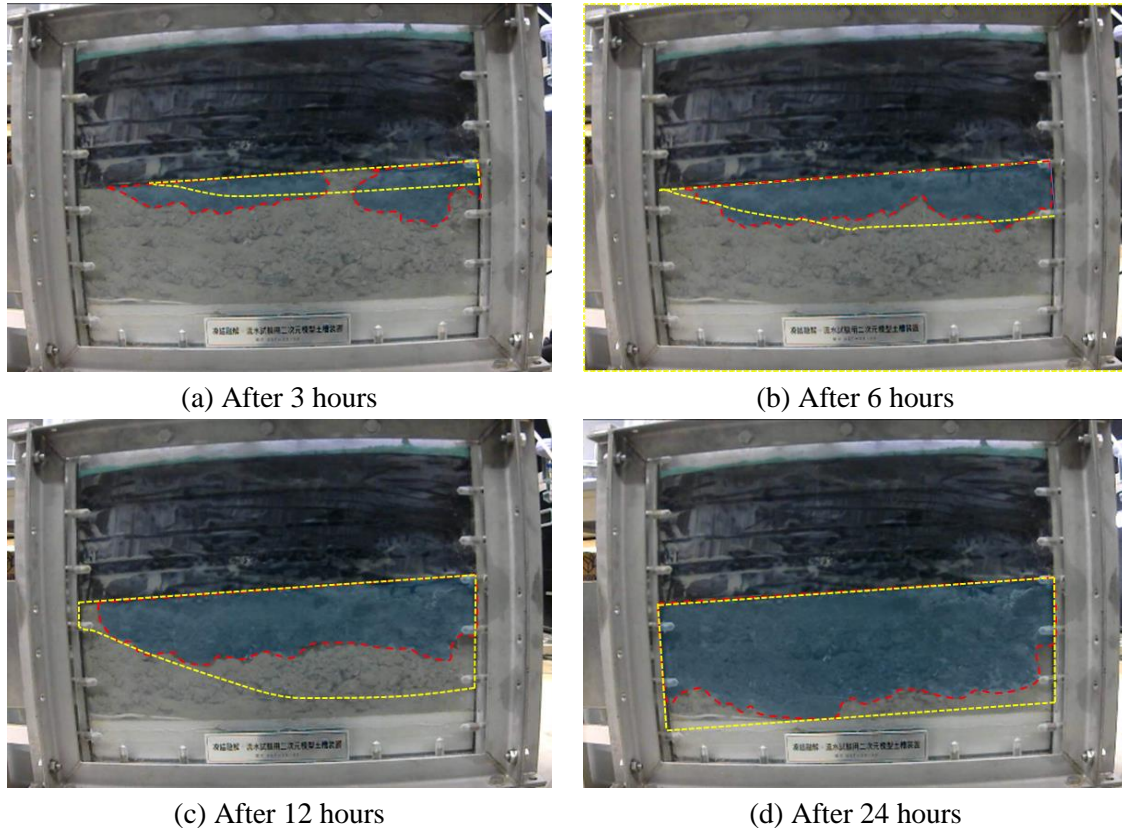


Figure 4-6 Time evolution of the wetting front.

(Red line: measured wetting front; Yellow line: simulated wetting front)

Figure 4-7 and Figure 4-8 show the evolution of water content profile measured and calculated by two-phase flow and single-phase flow models during the infiltration process. It can be seen from Figure 4-7 and Figure 4-8 that the water content of the base course layer is relatively low in the initial state. However, after continuous rainfall for 6 hours, the volumetric water content significantly increased within two hours due to the continuous decrease in matric suction at the measurement point. By comparing the results of two-phase flow and single-phase flow, it can be observed that air flow does not seriously affect the infiltration behavior under low rainfall intensity. By comparing with the measured results,

the numerical simulation well simulates the evolution process of soil moisture content. It should be noted that point ③ does not seem to fit well with the measured results. However, from the shape of the wetting front, the simulation results are consistent with the actual infiltration process. This may be due to the non-uniformity of the material causing water accumulation in some locations earlier.

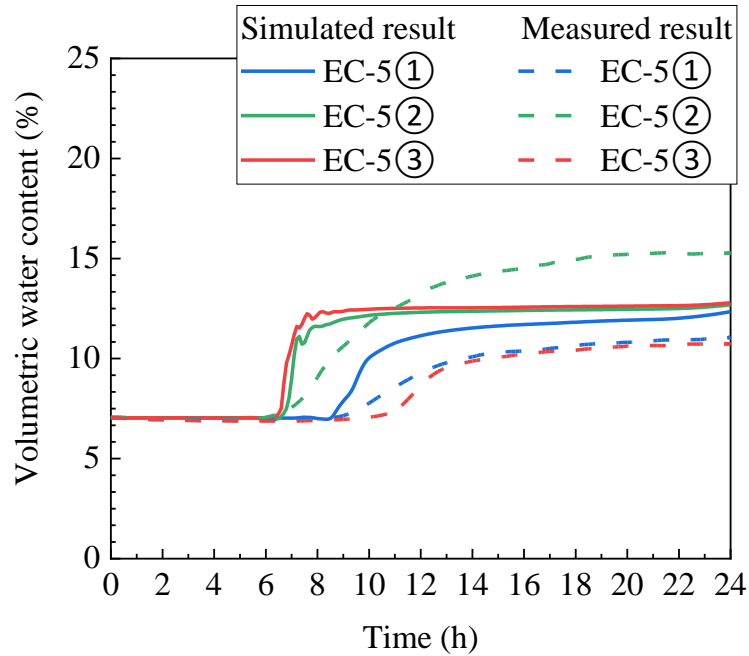


Figure 4-7 Measured and calculated evolution of water content profile during an infiltration process (Two-phase flow model).

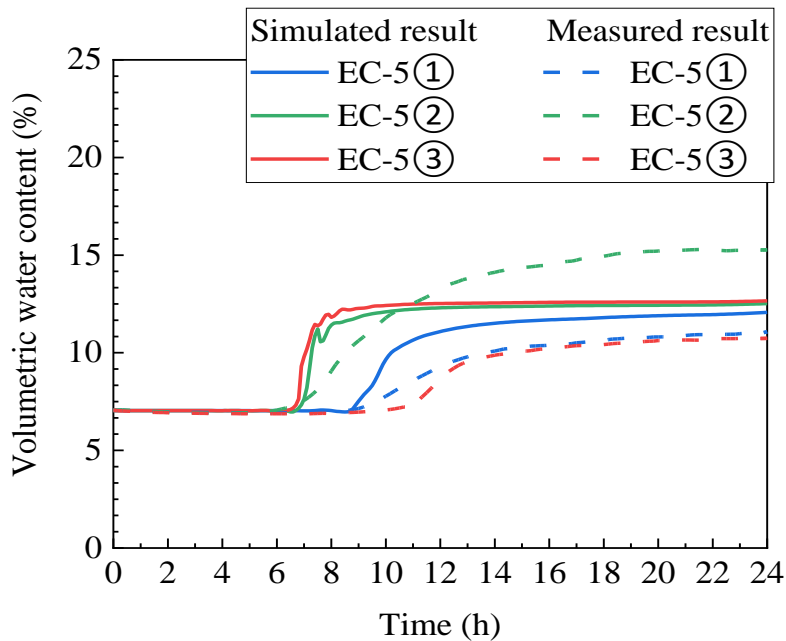


Figure 4-8 Measured and calculated evolution of water content profile during an infiltration process (Single-phase flow model).

Figure 4-9 and Figure 4-10 show the process of rainwater infiltration and lateral movement. From Figure 4-9 and Figure 4-10, it can be seen that when the wetting front reaches the top of the base course layer, due to the relatively low permeability, most of the infiltrating water will accumulate to a certain extent. With the continuous infiltration, some of the infiltrating rainwater will break through the interface without significant lateral flow and reach the base course layer. By comparing the results of two-phase flow and single-phase flow, it can be observed that air flow does not seriously affect the infiltration behavior under low rainfall intensity.

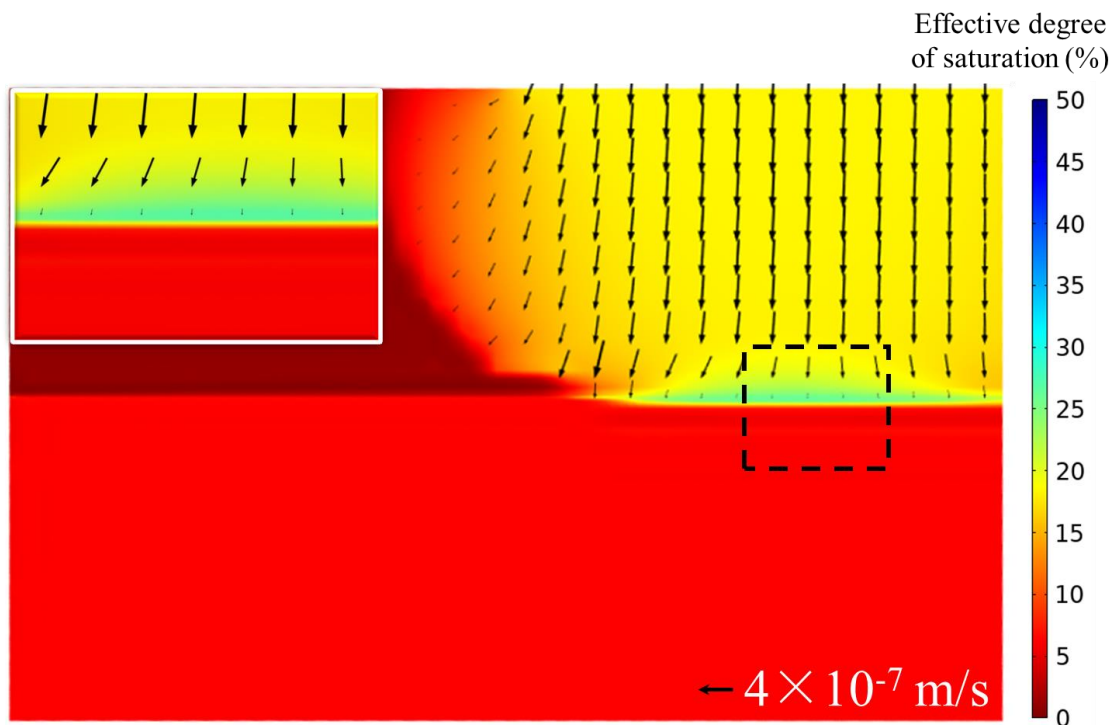


Figure 4-9 Process of rainwater infiltration into interface (Two-phase flow model) (1.5hours).

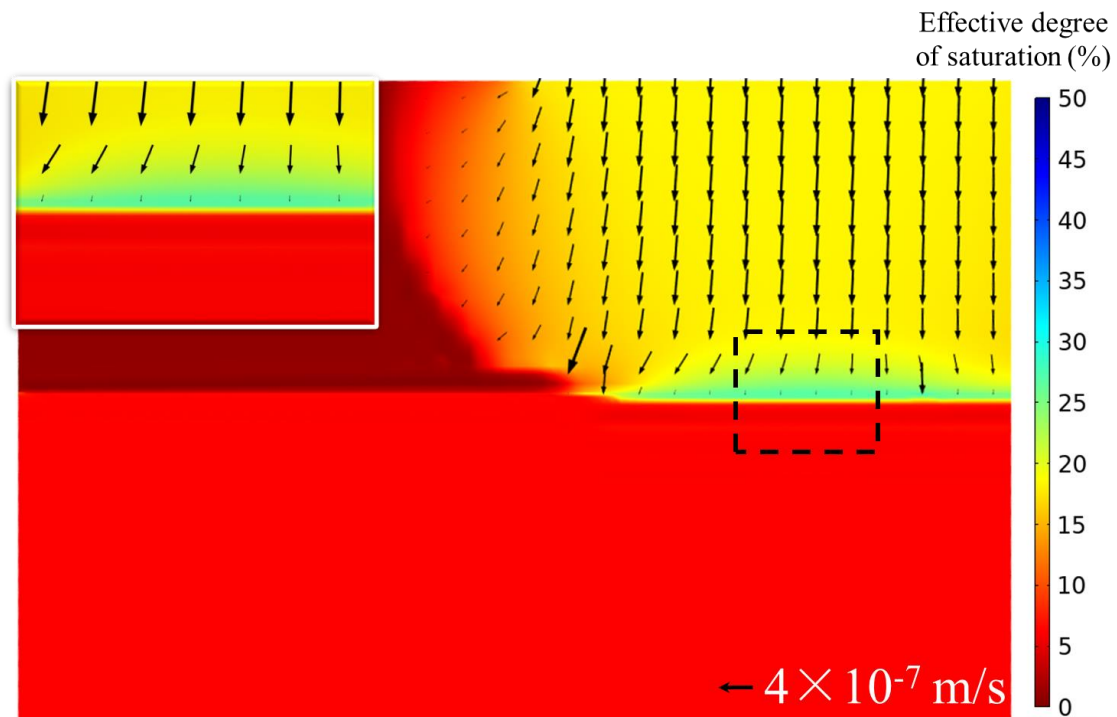


Figure 4-10 Process of rainwater infiltration into interface (Single-phase flow model) (1.5hours).

4.4 Summary

This chapter determines the hydraulic properties of various materials through laboratory experiments, investigates the infiltration behavior of asphalt pavement under rainfall, focuses on the hydraulic properties of the As layer, and compares the applicability of single-phase flow and two-phase flow models to simulate such behavior. The main findings of this chapter are summarized as follows:

- (1) The infiltration behavior of asphalt pavements can be evaluated through seepage analysis by considering hydraulic properties of As layer.
- (2) Model tests and soil/water/air coupled FE analysis show that single-phase flow model can adequately simulate pavement infiltration behavior and air flow does not seriously affect the infiltration behavior under low rainfall intensity.

5 RESILIENT MODULUS ESTIMATION OF PAVEMENT CONSIDERING THE ENVIRONMENTAL IMPACTS

It is widely acknowledged that environmental impacts such as temperature and moisture directly affect pavement material behavior and pavement performance. However, the effect of moisture on asphalt mixtures is insignificant compared to geomaterials. On the other hand, temperature affects both the asphalt and unbound layers significantly. Consequently, it is essential to assess the resilient pavement modulus in response to environmental impacts following the acquisition of temperature and water content data in the preceding section.

5.1 Evaluation of temperature-dependent resilient modulus of the asphalt layer

In present Japanese design guide, resilient modulus of As layer (E_1) changes with temperature as shown in Equation (5-1) and Equation (5-2). Meanwhile, Maruyama et al. (2012) proposed a new fitting equation (Equation (5-3)) to predict the temperature-dependent resilient modulus of asphalt layer. The fitting performance of these two prediction model is shown in Figure 5-1. From the Figure 5-1, it can be seen that since the two models did not consider the variation of the resilient modulus below 0°C during fitting process, they can only partially reflect the real situation. Therefore, it is necessary to propose a new fitting equation to address this issue.

$$M_p = M_a \left[1 + \frac{2.54}{h_1 + 10.16} \right] - \frac{25.4}{9(h_1 + 10.16)} + \frac{10}{3} \quad (5-1)$$

$$E_1 = -278.4M_p + 10930 \quad (5-2)$$

$$E_1 = \frac{1}{\left[\frac{1}{8500} + \{9.373 \times 10^{-19} \times (1.118^{T_1})\} \right]} \quad (5-3)$$

where M_p is the monthly mean temperature of asphalt mixture at depth of h_1 (°C); M_a is monthly mean air temperature (°C); h_1 is the depth equals to one-third of the height of

asphalt mixture (cm); T_1 is the average temperature of the As layer; E_1 is the elastic modulus of the As layer.

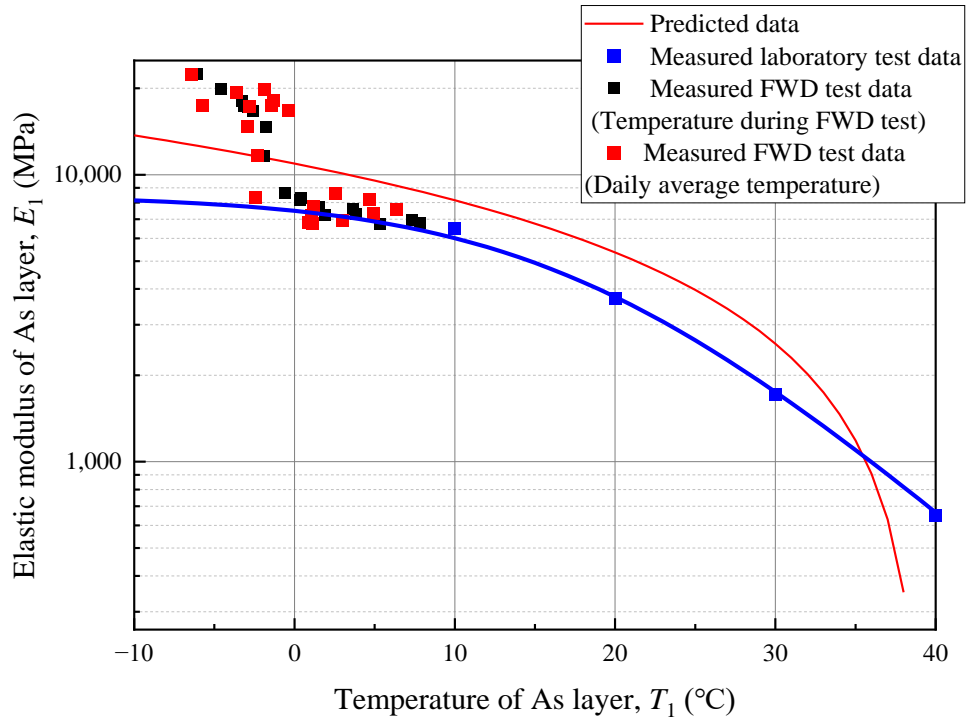


Figure 5-1 Relationship between the elastic modulus of the As layer and temperature.

Zhang et al. (2018a) proposed a reasonable method for predicting the elastic modulus of the As layer at different temperatures based on the elastic modulus of the asphalt mixture obtained from laboratory element tests, as shown in Equation (5-4).

$$E_1 = a \times \arctan (bT_1 + c) + d \quad (5-4)$$

where a , b , c , d are regression constants. When $T_1 < 10$ °C, the relationships between the elastic modulus of the As layer (E_1) obtained from FWD (Falling Weight Deflection) tests (Ishikawa et al., 2011a) and the temperature of the As layer (T_1 , daily average or during FWD test) are shown in Figure 5-2.

To complement the measured data of E_1 at higher T_1 , the E_1 - T_1 relationships obtained from 4PBF (Four-Point Bending Fatigue) tests (Maruyama et al., 2008) are added when $T_1 \geq 10$ °C. In addition, the regression analysis using Equation (5-4) is conducted on the E_1 - T_1 relationships. The regression results are shown in Figure 5-2. Here, by averaging the temperatures measured at two monitoring points with different depths shown

in Figure 5-2, the temperature of the As layer (T_1) was calculated at a depth of 6 cm under the ground surface. It is noted that the regression result was obtained by fitting the relationship between the elastic modulus of the As layer and the temperature during the FWD test or 4PBF test separately. It is recognized that Equation (5-4) can reflect the relationships between the elastic modulus of the As layer and the temperature during tests. Accordingly, through the daily average temperature of the As layer, the change in the daily average elastic modulus of the As layer with time can be estimated. Finally, Figure 5-3 shows the change of the resilient modulus of the asphalt layer with the temperature of the asphalt layer within one year.

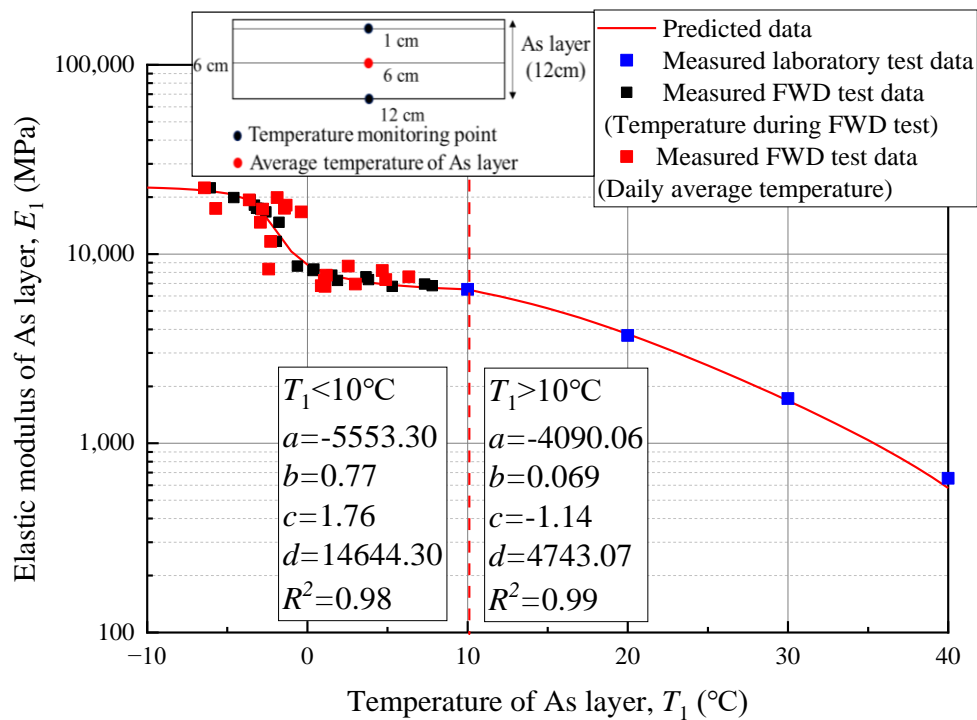


Figure 5-2 Relationship between the elastic modulus of the As layer and temperature (proposed model).

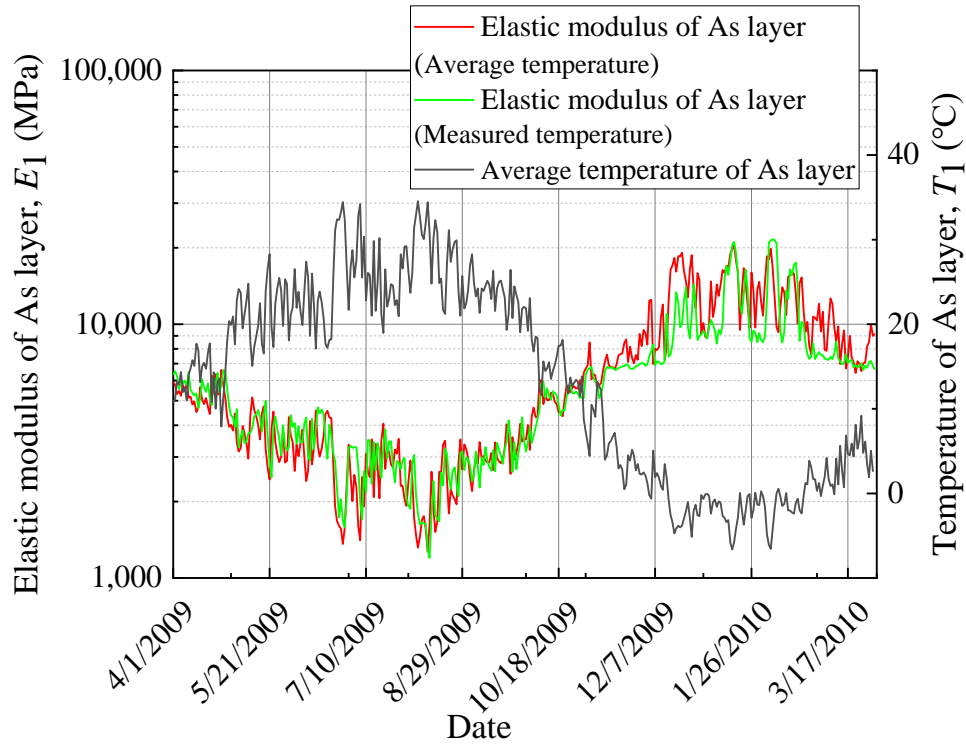


Figure 5-3 The change of the resilient modulus of As layer within one year.

5.2 Effects of soil moisture variations and freeze–thaw action on resilient modulus

5.2.1 Evaluation of resilient modulus of pavement geo-materials

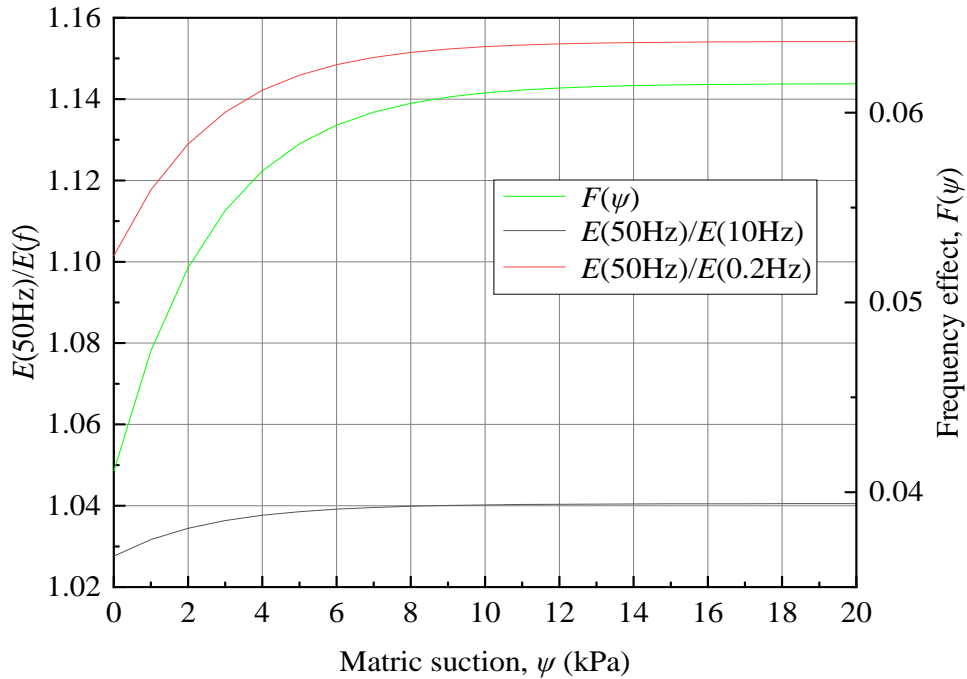
Moisture and temperature are the two environmentally driven variables that can significantly impact the resilient modulus of geomaterials. However, moisture has two distinct effects: it can influence the state of stress through suction or pore water pressure, and it can affect the soil structure by destroying cementation between particles. In freezing temperatures, the water in the soil freezes, causing the resilient modulus to increase to values higher than before freezing. This process may also create ice lenses, resulting in areas of significantly reduced strength in the pavement upon thawing. Only considering constant modulus will lead to inaccuracy and large variability (Fan et al., 2022). Therefore, in this study, evaluating the resilient modulus of the base and subgrade layers affected by moisture fluctuations and freeze–thaw action is necessary.

Lin et al. (2022) proposed a simple model to estimate the climate effect on the resilient modulus by considering the synergistic effects between water content and freeze–thaw action, as shown in Equation (5-5).

$$M_r = F_{clim} \cdot k_1 p_a \left(\frac{\sigma_{ii}}{p_a} \right)^{F_{clim} \cdot k_2} \left(\frac{\tau_{oct}}{p_a} + 1 \right)^{F_{clim} \cdot k_3} \left(\frac{\psi}{\sigma_{net}} + 1 \right)^{F_{clim} \cdot k_4} \quad (5-5)$$

where F_{clim} is the climatic factor; σ_{ii} is bulk stress (kPa), defined as $\sigma_1 + \sigma_2 + \sigma_3$; σ_{net} is net mean stress (kPa), defined as $(\sigma_{ii}/3 - u_a)$; and u_a is pore air pressure, set as 0 kPa in this study.

Meanwhile, the influence of loading frequency needs to be considered when using the results of laboratory element tests, as the loading frequency used in the FWD test is 50 Hz (Pavement Engineering Committee, 2002), while the loading frequencies in Ishikawa et al. (2019a) and Lin et al. (2022) are 10 Hz and 0.2 Hz, respectively. Equation (5-6) to Equation (5-8) were proposed to describe the loading rate effect on the resilient modulus (Kim et al., 1997).



$$\frac{E(f)}{E(0.5 \text{ Hz})} = 1 + F(\psi) * \log (f) \quad (5-6)$$

$$F(\psi) = 0.06153 - 0.02043 \times 0.68826^\psi \quad (5-7)$$

$$E(50 \text{ Hz}) = \left(\frac{E(50 \text{ Hz})}{E(0.5 \text{ Hz})} / \frac{E(f)}{E(0.5 \text{ Hz})} \right) E(f) = \left(\frac{1+F(\psi) \times \log(50)}{1+F(\psi) \times \log(f)} \right) E(f) \quad (5-8)$$

where f is the loading frequency; $E(0.5 \text{ Hz})$ is the resilient modulus obtained at $f = 0.5 \text{ Hz}$; $E(f)$ is the predicted resilient modulus at any frequency (f); and $F(\psi)$ is referred to as the frequency effect, which is affected by matric suction (ψ) (Lin et al., 2022). Through Equation (5-8), derived from Equation (5-6) and Equation (5-7), the resilient modulus of base course layer, $E_2(10 \text{ Hz})$ obtained from Ishikawa et al. (2019a) and the resilient modulus of subgrade soil, $E_3(0.2 \text{ Hz})$ obtained from Lin et al. (2022) were converted to the resilient modulus ($E_2(50 \text{ Hz})$ and $E_3(50 \text{ Hz})$) of FWD test.

To help visualize possible changes in resilient modulus caused by changes in the physical state with time, a time-depth diagram for a typical pavement structure is presented in Figure 5-4. Here, the frozen state (blue, denoted M_{rF}) is one where the soil temperature is lower than freezing temperature, while the recovering state (red, denoted M_{rR}) is one where the soil temperature is higher than freezing temperature after freezing. Another state is the unfrozen state (orange, denoted M_{rU}). Notably, the coexistence of these four physical states is possible within a given layer. The following section presents the algorithm utilized in MEPSCA, which delineates a methodology for acquiring composite moduli for layers where multiple material states coexist and/or the resilient modulus fluctuates with depth and time.

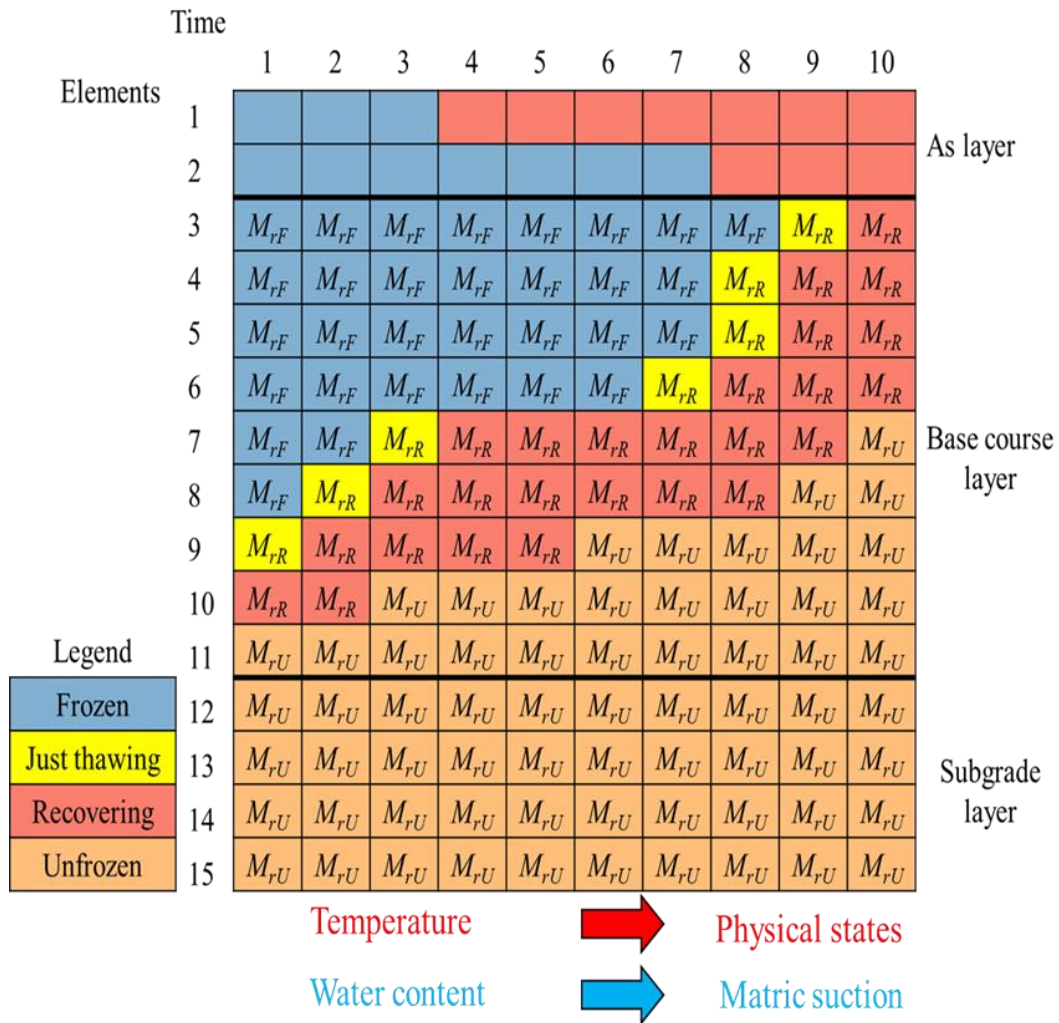


Figure 5-4 Time-depth diagram of a typical pavement structure.

The following description outlines a methodology for estimating physical states, demonstrating the calculation of adjustment factors for each element in all three cases. For the behavior of base and subgrade layers, the absolute modulus of frozen geomaterials is obtained according to the on-site FWD test (Si et al., 2022). Table 5-1 summarizes the mechanism of bearing capacity reduction due to freeze-thaw (Ishikawa et al., 2019a). Though the resilient modulus estimated by Equation (5-5) can evaluate the minimum resilient modulus during just thawing state, there is a possibility that with time passing the reduced resilient modulus recovers to an unfrozen state. Therefore, for recovering geomaterials, the resilient modulus exhibits a time-dependent increase that ranges from the just thawing state (M_{rmin}) to the unfrozen state (M_{rU}). This increase can be quantified by

the recovery ratio (RR) on a scale from 0 to 1, as shown in Equation (5-9) (NCHRP, 2004). Accordingly, the configuration method of climatic factors (F_{clim}) during the recovery period in numerical simulation can be obtained, as shown in Equation (5-10).

$$RR = \frac{T_{R,S}}{T_R} \quad (5-9)$$

$$F_{clim} = (F_{clim,min} + RR(1 - F_{clim,min})) \quad (5-10)$$

where $T_{R,S}$ is the number of days elapsed from thawing started in numerical simulation; T_R is the number of days required for a given geomaterial from thawed state to unfrozen state (NCHRP, 2004), as shown in Table 5-2; and $F_{clim,min}$ is the minimum of climatic factor during just thawing state.

Table 5-1 Mechanism of bearing capacity reduction due to freeze-thaw.

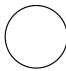
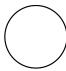
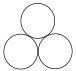









Water content conditions	Particle moisture content		Soil structure Image	Change amount	Bearing capacity Variability (Factor)
	Before freeze-thaw	After freeze-thaw			
Dry				None	None
Air-dried				None	Reversible (Change of friction)
Wet				Medium	Irreversible (Change of structure)
Saturated				Large	Irreversible (Change of structure)

Table 5-2 The number of days required for a geomaterial from thawed state to unfrozen state.

	Sands or gravels	Silts or clays	Clays
P_{200PI}	<0.1	0.1~10	>10
T_R (days)	90	120	150

where P_{200} is the percent passing the No. 200 sieve (0.075mm); PI is plasticity index.

5.2.2 Assessment of physical condition of pavement elements

However, when the temperature exceeds the freezing temperature, the physical state of a geomaterial cannot be determined solely based on temperature, as it may exist in an unfrozen or thawed state. Consequently, in this study, Equation (5-11) to Equation (5-16) and five intermediate variables (IVs) were employed to ascertain the recovery state of soil elements and the number of days elapsed since thawing started ($T_{R,S}$). Figure 5-5 illustrates the correlation between temperature and various intermediate variables during simulation. Initially, the IV_0 is defined, followed by obtaining IV_2 through two integrations (Equation (5-11) to Equation (5-13)). This latter variable is employed to describe the physical condition of each element, as shown in Equation (5-14). Notably, when IV_2 is greater than zero and the temperature is also above freezing temperature the element is in a recovering state. Conversely, when IV_2 is equal to zero and the temperature is above freezing temperature the element remains in an unfrozen state. Finally, when the temperature drops below freezing temperature the element transitions into a frozen state.

$$IV_0 = \begin{cases} 1, & T \leq T_0 \\ 0, & T > T_0 \end{cases} \quad (5-11)$$

$$IV_1 = \int IV_0 dt \quad (5-12)$$

$$IV_2 = \begin{cases} 0, & T \leq T_0 \\ IV_1, & T > T_0 \end{cases} \quad (5-13)$$

$$\begin{cases} T \leq T_0, & \text{Frozen state} \\ IV_2 > 0 \wedge T > T_0, & \text{Recovering state} \\ IV_2 = 0 \wedge T > T_0, & \text{Unfrozen state} \end{cases} \quad (5-14)$$

To precisely quantify the number of days elapsed in the recovery period (excluding the frozen period) of each element, the normalization of IV_2 to obtain IV_3 is undertaken (Equation (5-15)), followed by the integration of the latter to derive $T_{R,S}$, as shown in Equation (5-16).

$$IV_3 = \begin{cases} 0, & IV_2 \leq 0 \\ 1, & IV_2 > 0 \end{cases} \quad (5-15)$$

$$T_{R,S} = \int IV_3 dt \quad (5-16)$$

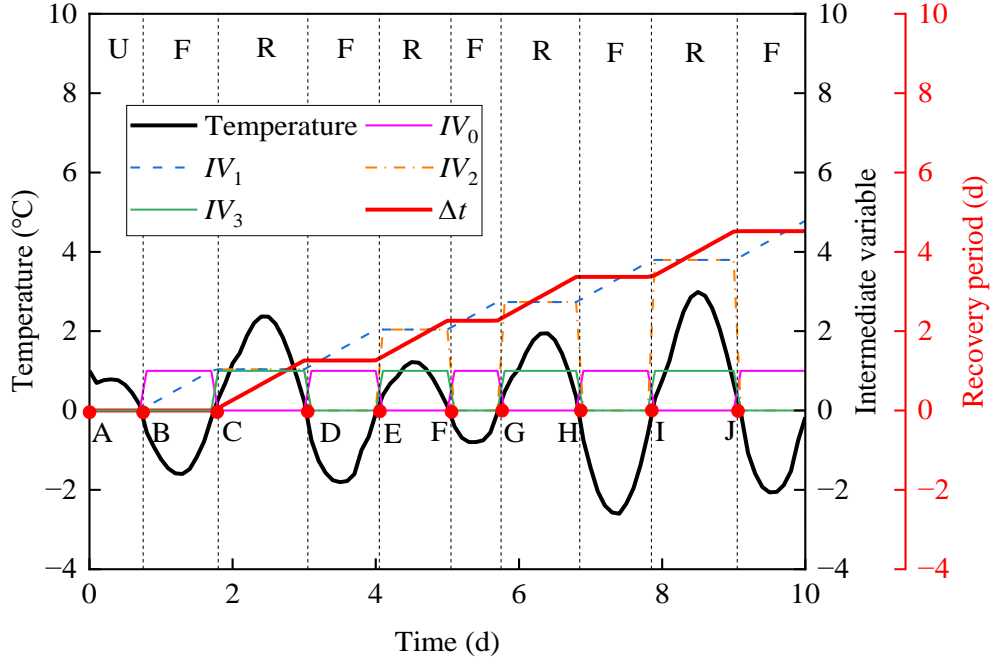


Figure 5-5 The relationship between element temperature and recovery period.

In summary, the expressions for the resilient modulus of the base and subgrade layers as a function of climatic factors and loading frequency can be derived, as shown in Equation (5-17) and Equation (5-18).

$E_2(50 \text{ Hz}) =$

$$\begin{cases} M_{rF} = 1120 \text{ MPa} \\ M_{rU} = \frac{E(50 \text{ Hz})}{E(10 \text{ Hz})} k_1 p_a \left(\frac{\sigma_{ii}}{p_a} \right)^{k_2} \left(\frac{\tau_{oct}}{p_a} + 1 \right)^{k_3} \left(\frac{\psi}{\sigma_{net}} + 1 \right)^{k_4} \\ M_{rmin} = \frac{E(50 \text{ Hz})}{E(10 \text{ Hz})} F_{clim,min} \cdot k_1 p_a \left(\frac{\sigma_{ii}}{p_a} \right)^{F_{clim,min} \cdot k_2} \left(\frac{\tau_{oct}}{p_a} + 1 \right)^{F_{clim,min} \cdot k_3} \left(\frac{\psi}{\sigma_{net}} + 1 \right)^{F_{clim,min} \cdot k_4} \\ M_{rR} = \frac{E(50 \text{ Hz})}{E(10 \text{ Hz})} F_{clim} \cdot k_1 p_a \left(\frac{\sigma_{ii}}{p_a} \right)^{F_{clim} \cdot k_2} \left(\frac{\tau_{oct}}{p_a} + 1 \right)^{F_{clim} \cdot k_3} \left(\frac{\psi}{\sigma_{net}} + 1 \right)^{F_{clim} \cdot k_4} \end{cases} \quad (5-17)$$

$E_3(50 \text{ Hz}) =$

$$\begin{cases} M_{rF} = 200 \text{ MPa} \\ M_{rU} = \frac{E(50 \text{ Hz})}{E(0.2 \text{ Hz})} k_1 p_a \left(\frac{\sigma_{ii}}{p_a} \right)^{k_2} \left(\frac{\tau_{oct}}{p_a} + 1 \right)^{k_3} \left(\frac{\psi}{\sigma_{net}} + 1 \right)^{k_4} \\ M_{rmin} = \frac{E(50 \text{ Hz})}{E(0.2 \text{ Hz})} F_{clim,min} \cdot k_1 p_a \left(\frac{\sigma_{ii}}{p_a} \right)^{F_{clim,min} \cdot k_2} \left(\frac{\tau_{oct}}{p_a} + 1 \right)^{F_{clim,min} \cdot k_3} \left(\frac{\psi}{\sigma_{net}} + 1 \right)^{F_{clim,min} \cdot k_4} \\ M_{rR} = \frac{E(50 \text{ Hz})}{E(0.2 \text{ Hz})} F_{clim} \cdot k_1 p_a \left(\frac{\sigma_{ii}}{p_a} \right)^{F_{clim} \cdot k_2} \left(\frac{\tau_{oct}}{p_a} + 1 \right)^{F_{clim} \cdot k_3} \left(\frac{\psi}{\sigma_{net}} + 1 \right)^{F_{clim} \cdot k_4} \end{cases} \quad (5-18)$$

The material input parameters used in mechanical analysis are listed in Table 5-3. The value of constants k_1 to k_4 and F_{clim} in Equation (5-5) are determined through regression analysis on resilient modulus test results of C-40 and Tomakomai soil (Lin et al., 2021; Ren et al., 2023).

Table 5-3 Material input parameters in mechanical analysis.

Parameters	Unit	As layer	Base course layer	Anti-frost layer	Subgrade layer
Regression constants (k_1)	-	-	3.042	3.042	0.526
Regression constants (k_2)	-	-	0.886	0.886	1.293
Regression constants (k_3)	-	-	-1.696	-1.696	-2.650
Regression constants (k_4)	-	-	1.076	1.076	1.008
Regression constants (F_{clim})	-	-	0.749	0.749	0.948

5.3 Numerical simulation results

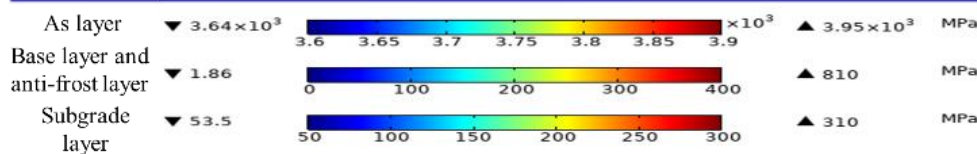
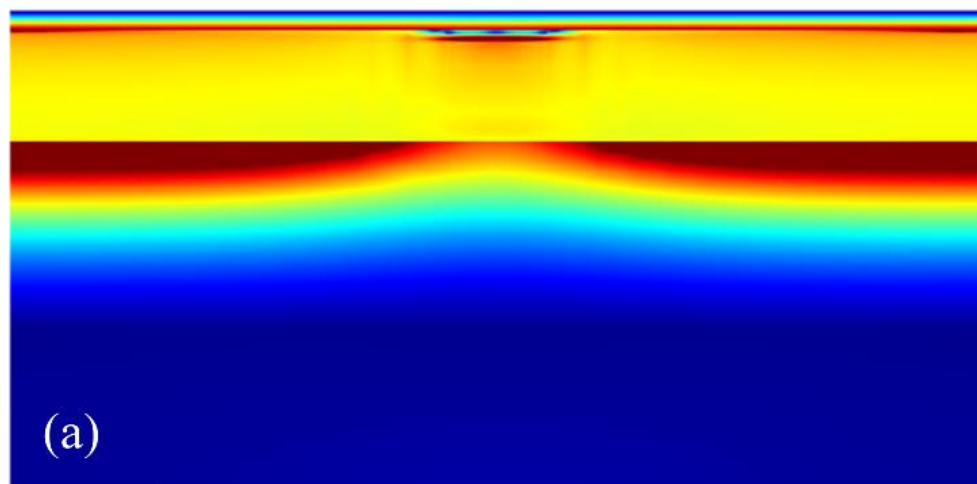
To analyze the impact of weather conditions on the resilient modulus, five specific weather conditions shown in Table 5-4 have been selected for separate evaluation. This analysis involves studying the distribution of the resilient modulus under each weather condition. Additionally, comparative analysis considers specific on-site testing dates for different projects. Furthermore, the Bibi test pavement’s service period from 1990 to 2004 resulted in most of the measured results being within this period.

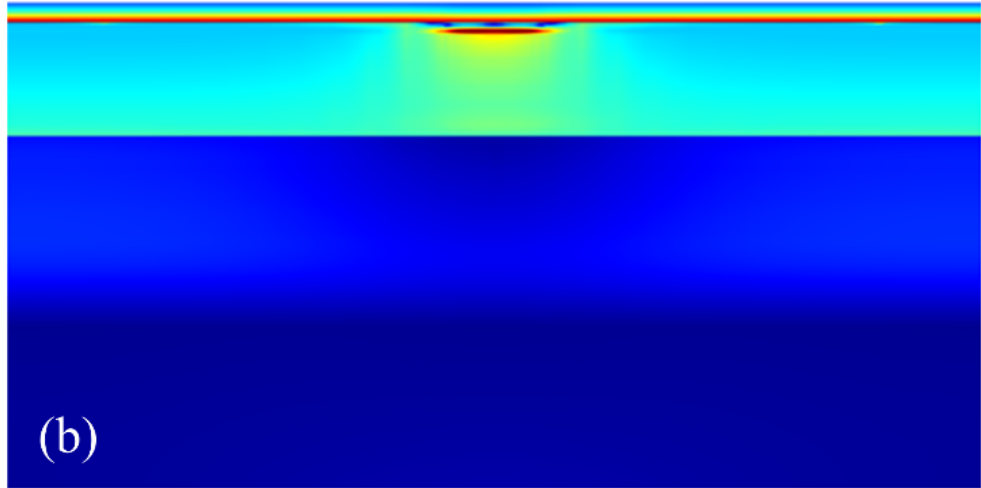
Table 5-4 Selection of weather conditions.

	Regular Season -Sunny Day	Regular Season -Rainy Day	Freezing Season	Partial Thawing Season	Thawing Season
Date	10 May 2009	20 July 2009	7 February 2010	22 February 2010	4 March 2010

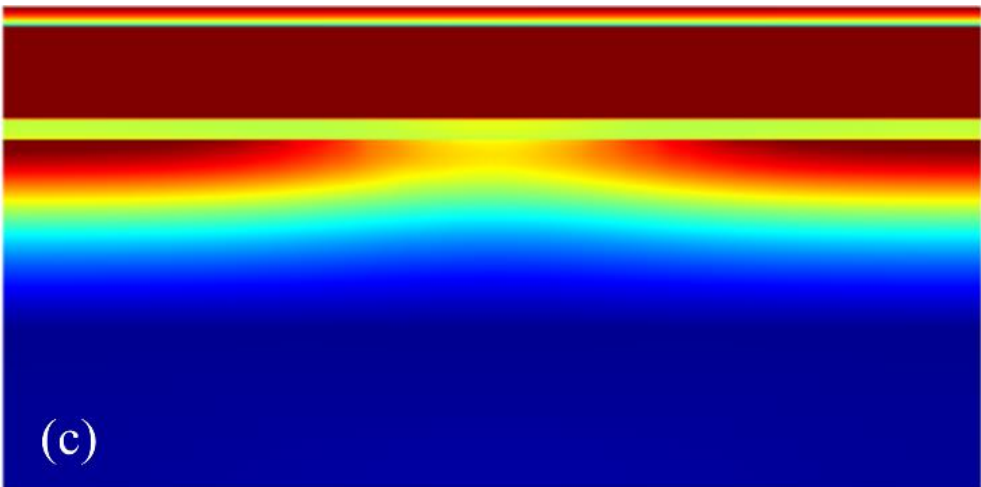
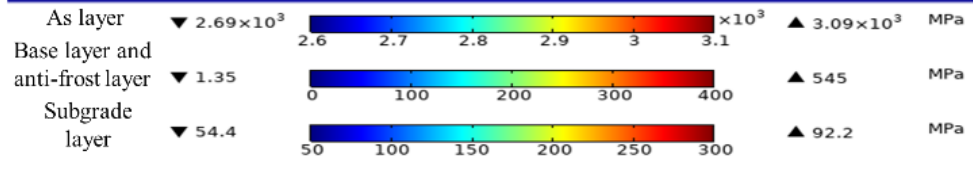
Situation description	No rainfall	Rainfall reaches the maximum	Frost-penetration depth reaches the maximum	A typical Sandwich-Structure	Snowmelt water reaches the maximum
-----------------------	-------------	------------------------------	---	------------------------------	------------------------------------

The distributions of resilient modulus within the pavement in different seasons are plotted in Figure 5-6. The temperature affects the fatigue life through stiffness of As layer that decreases with increasing temperature (Tangella et al., 1990). It is evident that the As layer exhibits a varying resilient modulus distribution with depth, which is mainly attributed to temperature. In winter, the surface temperature is lower than the internal temperature, while in the regular and thawing seasons the surface temperature is higher than the internal temperature. From Figure 5-6, it can be found that the resilient modulus increases as the depth increases due to the bulk stress of soils increasing, and the octahedral shear stress is weakened along with the depth. Under the center of wheel loads, the resilient modulus at the surface of the base course layer changes significantly due to the stress concentration in this area. It can also be found that in the thawing season and rainy days, higher water content dramatically reduces the resilient modulus of the base course layer and subgrade layer, and freezing action improves the resilient modulus of the base course layer. Moreover, the resilient modulus above the groundwater level increases with increasing the matric suction away from the groundwater level. The resilient modulus below the groundwater level increases with increasing bulk stress as the matric suction keeps zero.

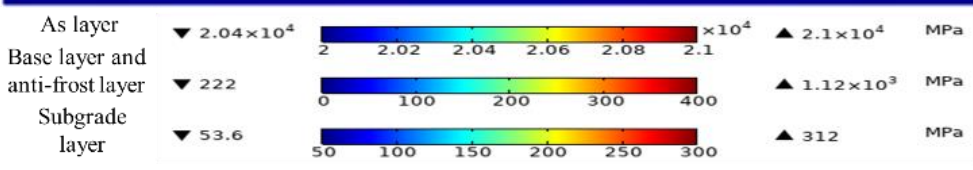




(b)



(c)



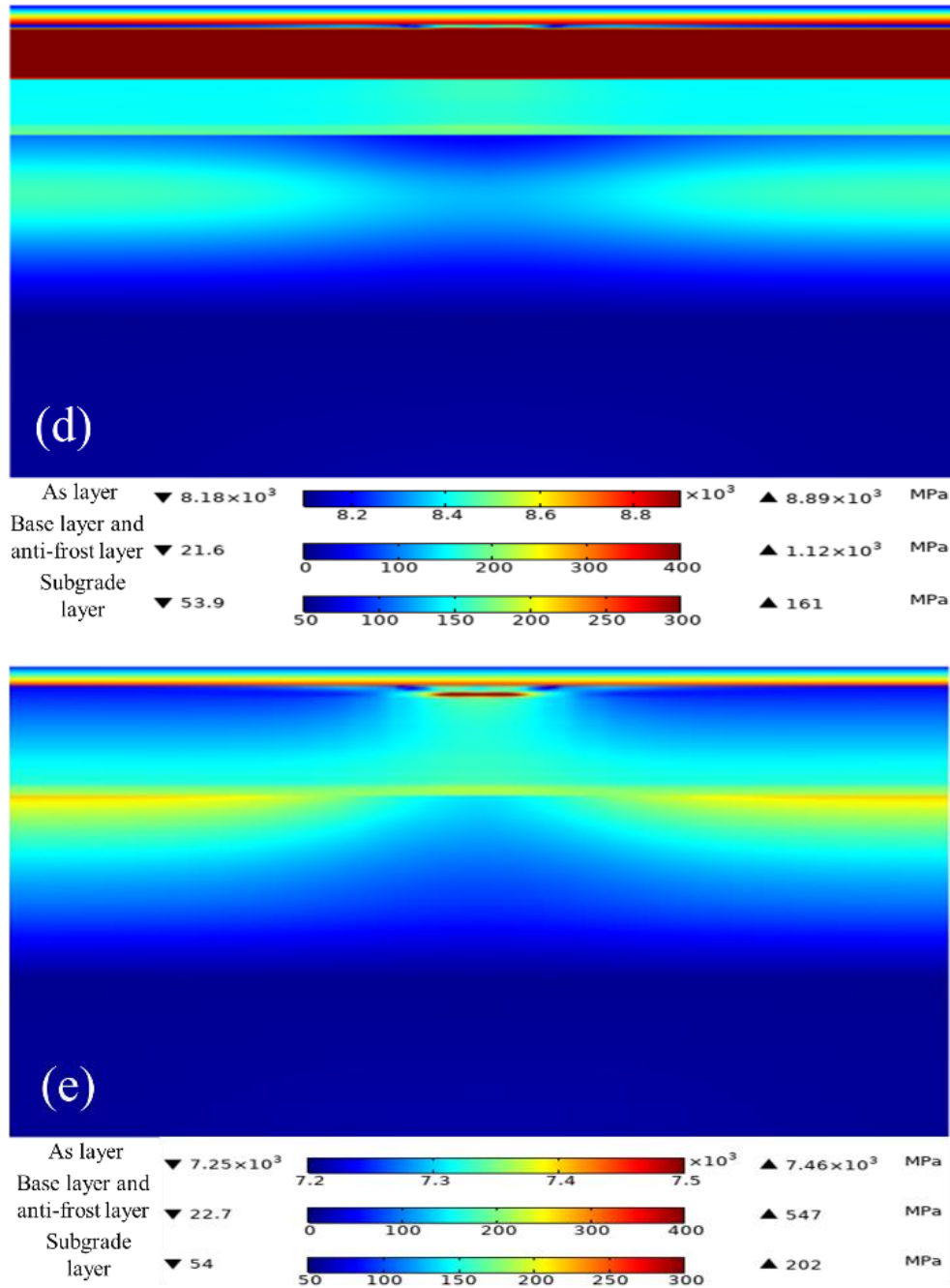


Figure 5-6 Resilient modulus distribution in different seasons ((a) regular season-sunny day; (b) regular season-rainy day; (c) freezing season; (d) partial thawing season; (e) thawing season).

To verify the efficiency and effectiveness of the developed MEPSCA, an essential investigation was conducted to study the reduced bearing capacity of the base and subgrade layers during the thawing season in cold regions. Figure 5-7 displays the distribution of the degree of saturation and resilient modulus of the As layer, base layer, and anti-frost layer

without a wheel load as of 22 February 2010, when thawing had progressed after freezing, as the previous analysis results determined. The depth in Figure 5-7 indicates the distance from the ground surface. While the As and base layers have thawed, the base layer has only thawed near the upper area, with most other parts still frozen. The degree of saturation near the thawed base layer has increased, resulting in decreased resilient modulus near the upper area of the base layer. This is because when rainwater or snowmelt flows into the base layer, the frozen area has lower permeability than the thawed area, resulting in stagnant water at the upper boundary of the frozen area. These results partially reflect the importance of evaluating the environmental impacts on the fatigue life of pavement structures in cold regions.

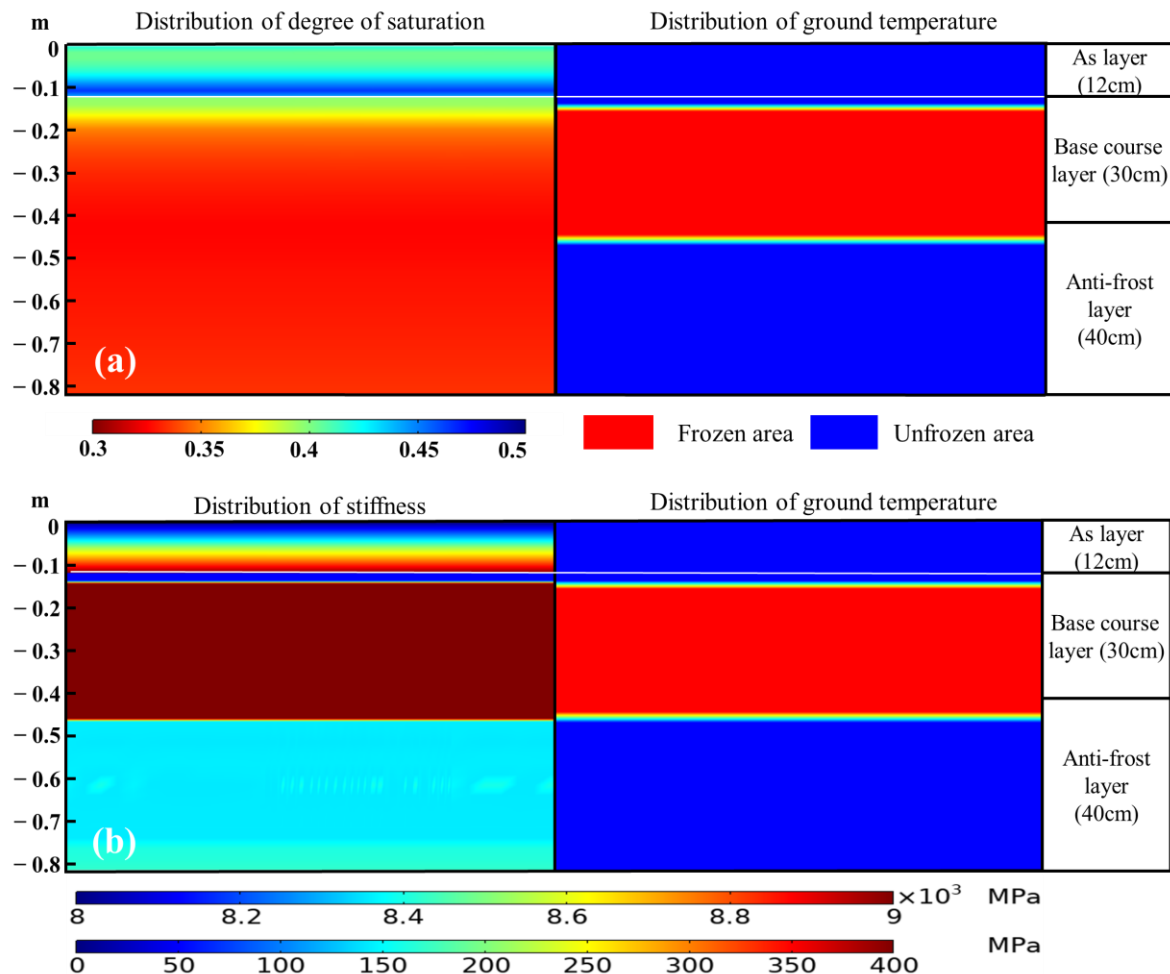


Figure 5-7 Distribution of the resilient modulus and degree of saturation during the freezing and thawing process ((a) resilient modulus; (b) degree of saturation).

5.4 Verification of MEPSCA

The resilient modulus estimated through FE simulation is compared with the measured resilient modulus in Figure 5-8 and Figure 5-9. Although the MEPSCA can provide the resilient modulus of each element, to make a reasonable comparison with the measured value it is necessary to use the average method to evaluate the overall resilient modulus of the pavement. It is important to note that, for comparison with measured data, the volume average resilient modulus within a range of 1.5 m on both sides of the load center is calculated in the FE simulation, which is consistent with the deflection recorded by the FWD test within a range of 1.5 m around the load center.

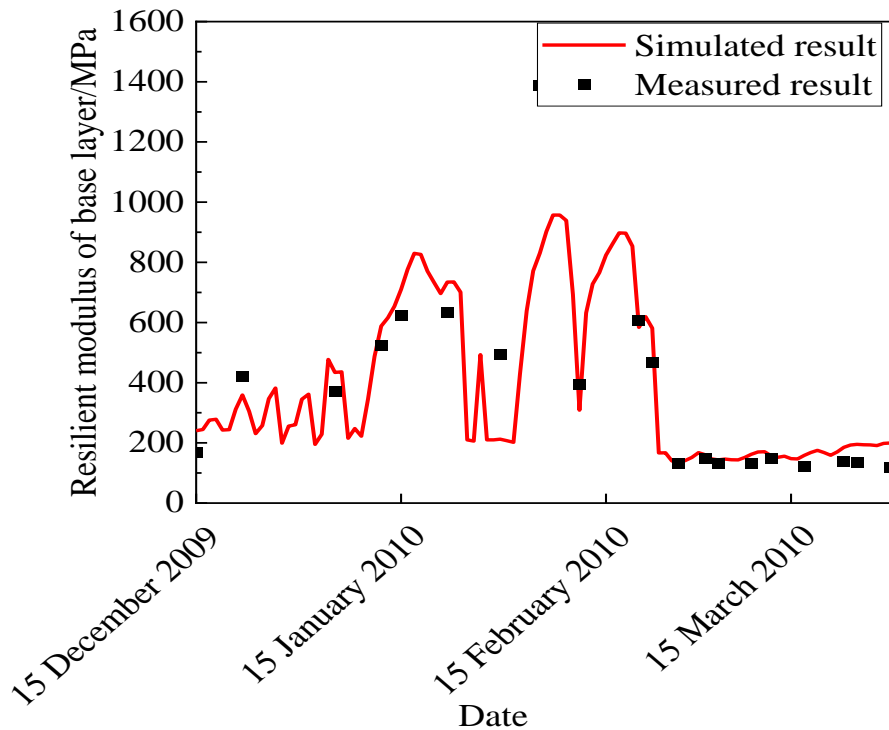


Figure 5-8 Simulated and measured resilient modulus of base course layer.

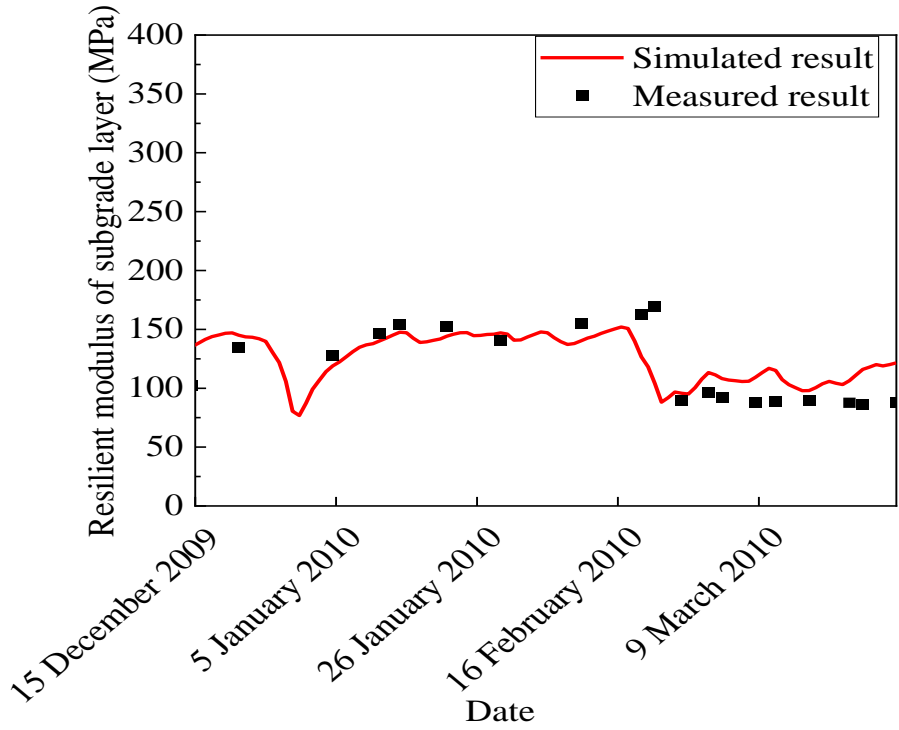


Figure 5-9 Simulated and measured resilient modulus of subgrade layer.

Based on Figure 5-8 and Figure 5-9, it can be seen that the resilient modulus of the base course layer is greatly affected by the frost-penetration depth during the freezing season. Due to the influence of weather conditions in the thawing season, the resilient modulus decreases dramatically, which may significantly impact the fatigue life of the pavement. On the other hand, the resilient modulus of the subgrade layer resilient modulus is notably influenced by changes in water content. Overall, the simulation method proposed in this study can effectively capture the variation of pavement resilient modulus over time.

To further validate the fatigue life prediction of the Bibi test pavement, the resilient modulus of the pavement will be simulated and verified using two different methods, including the MEPDG and MEPSCA. The implementation of the MEPDG method is carried out through the AASHTOWare Pavement ME Design (AASHTOWare Pavement ME Design, 2021).

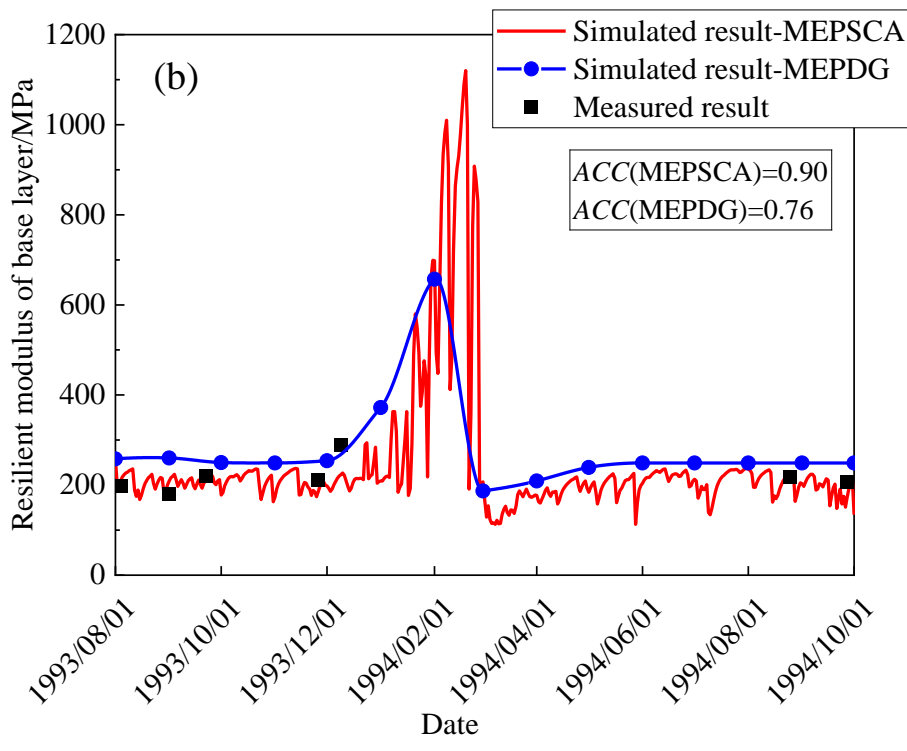
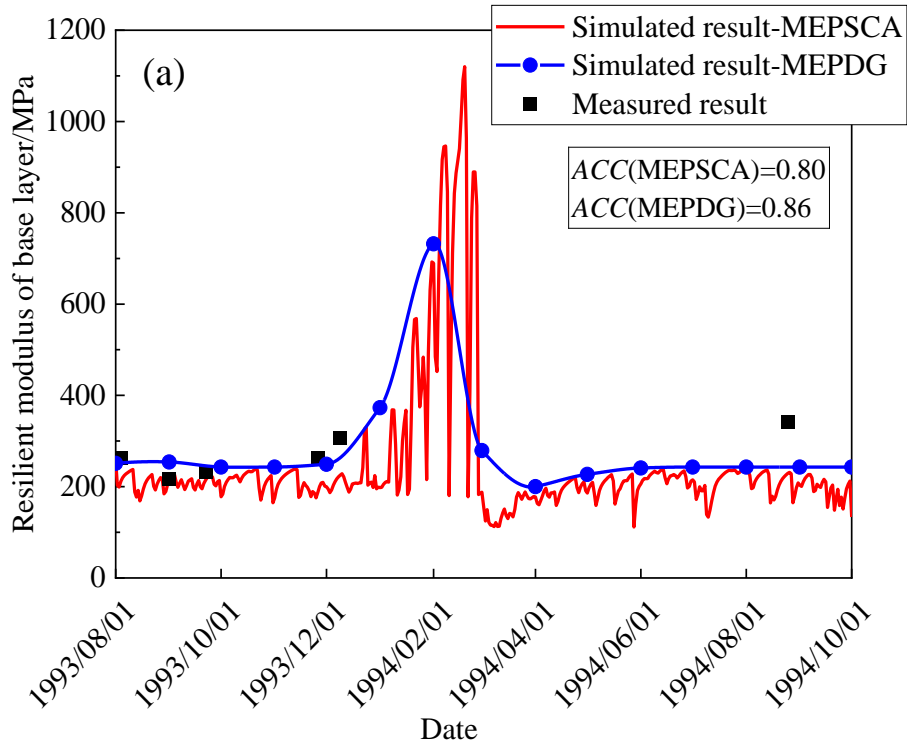
Validating the simulation results of the resilient modulus is crucial because it is a critical parameter in predicting the fatigue life of the pavement. Accuracy (*ACC*) is defined to evaluate the difference between measured and simulated results from the MEPDG or

MEPSCA. Equation (5-19) specifies this term, and a greater accuracy value indicates a better match between the measured and simulated results.

$$ACC = \frac{\sum_{i=1}^N (1 - \frac{|u_i - z_i|}{u_i})}{N'} \quad (5-19)$$

where u_i is the measured resilient modulus of i -th measurement; z_i is the simulated resilient modulus of i -th measurement; and N' is the number of measurements.

After examining the comparison results presented in Figure 5-10 and Figure 5-11, it appears that both the MEPSCA and MEPDG can predict the resilient modulus of the pavement well. However, the MEPSCA method seems to calculate a daily representative resilient modulus, which can offer more precise and applicable results than a monthly representative value. This is because daily calculations can account for more extreme impacts of freezing–thawing and changes in water content on the resilient modulus, which can significantly influence the performance of pavement structures. In addition, the accuracy of the daily calculations exceeds 0.8, which indicates that the MEPSCA is a reliable method for predicting the resilient modulus.



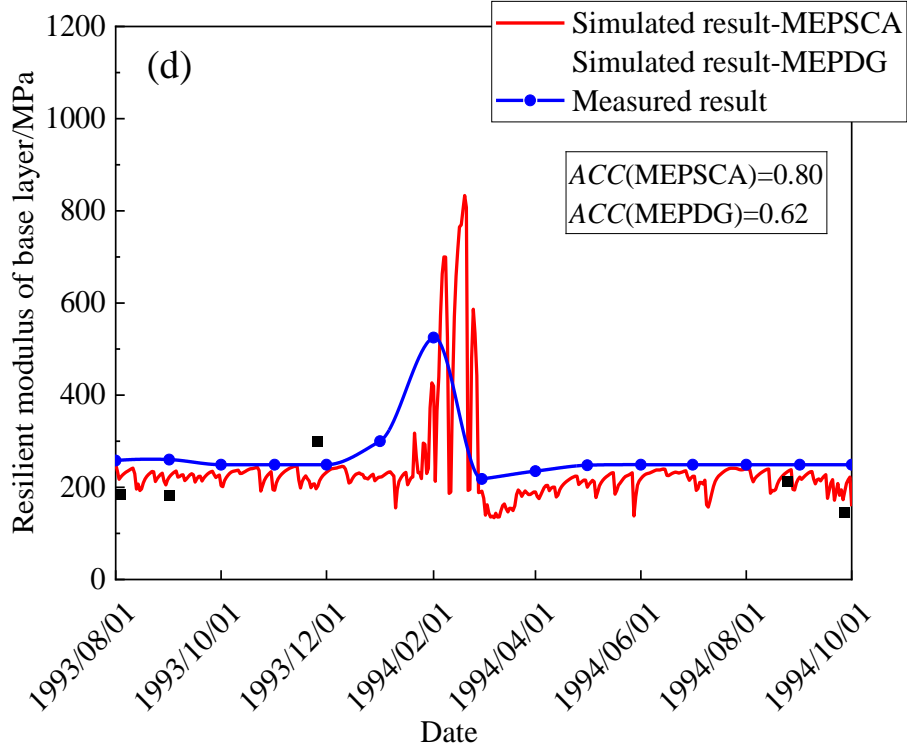
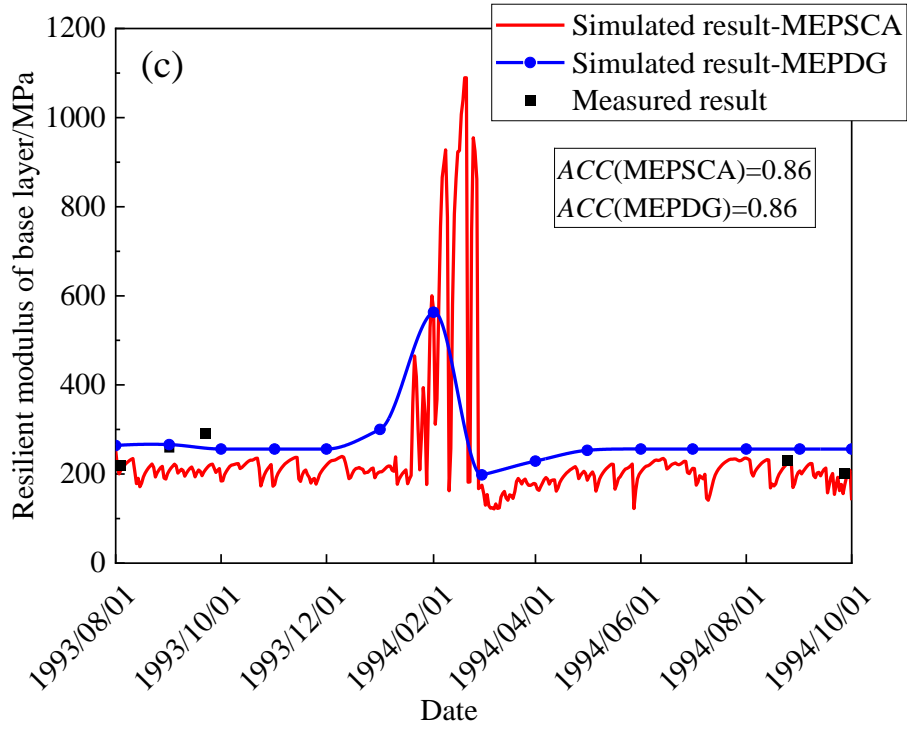
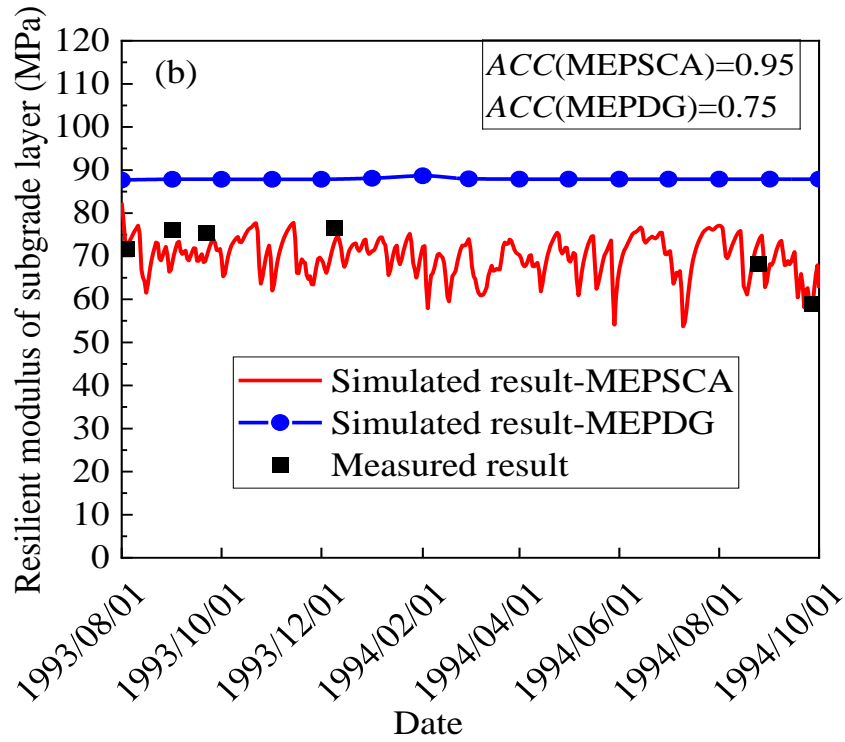
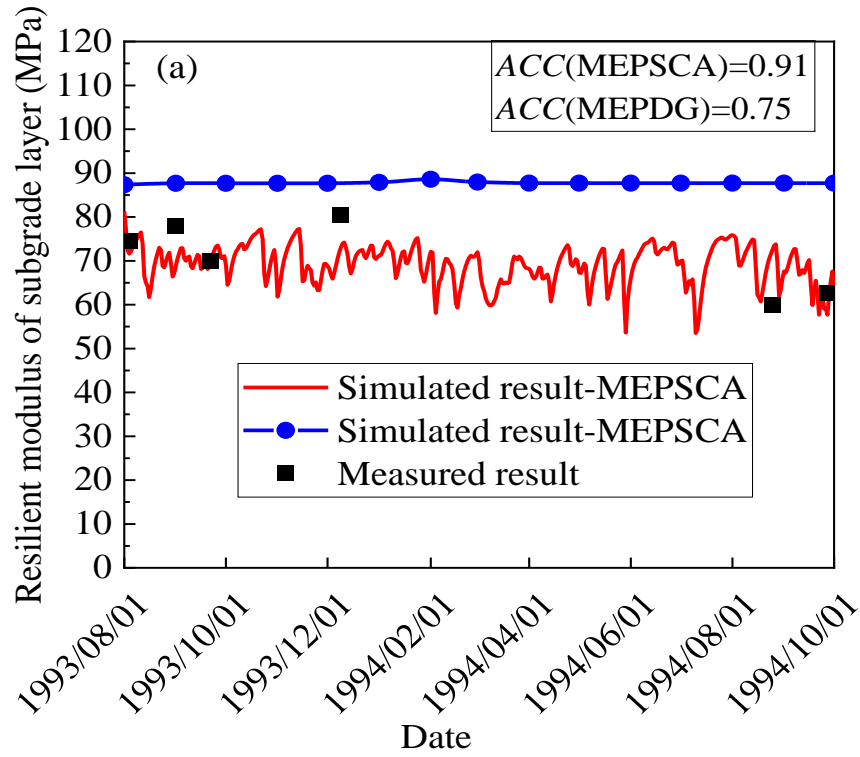


Figure 5-10 Simulated and measured resilient modulus of base course layer ((a). section A; (b). section B; (c). section C; (d). section D).



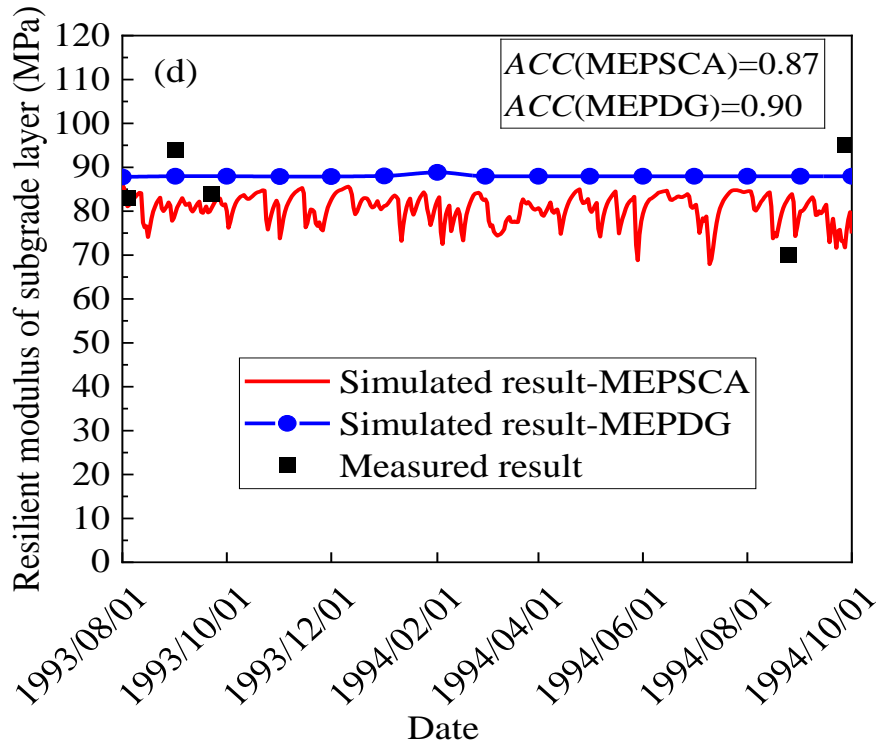
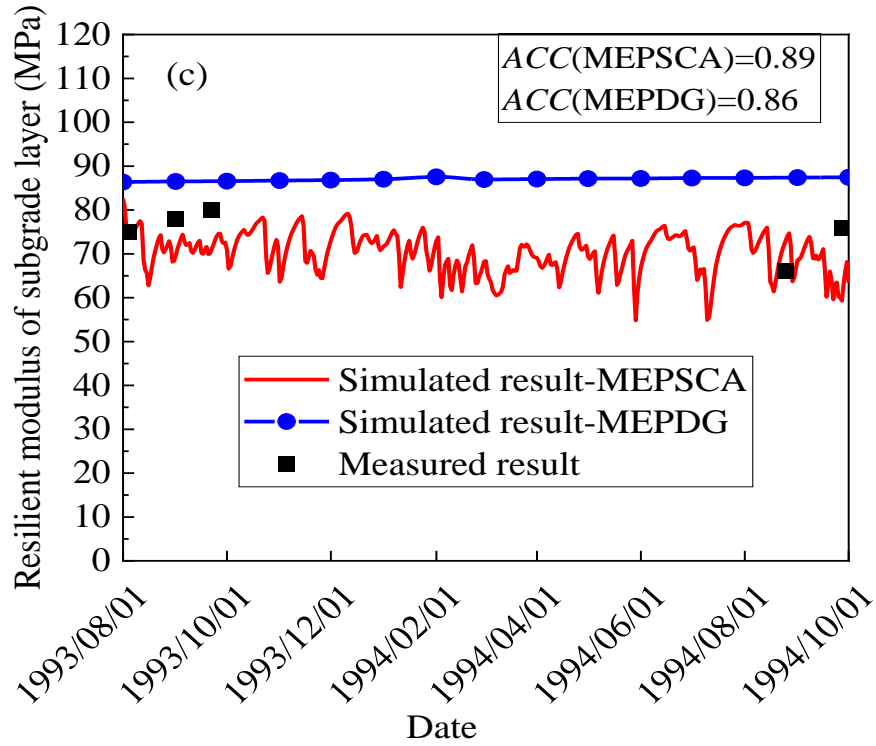


Figure 5-11 Simulated and measured resilient modulus of subgrade layer ((a). section A; (b). section B; (c). section C; (d). section D).

5.5 Summary

Based on the research results from FWD tests, 4PBF tests, and cyclic triaxial tests, this chapter establishes a system for evaluating the environmental impact on the resilient modulus of pavement materials. Furthermore, a successful method is proposed for determining the physical state of each pavement element using ordinary differential equations in numerical simulations. Through field measurements and comparison with simulated data, the feasibility of the proposed method in predicting the elastic modulus of pavement materials is confirmed. The main conclusions of this chapter are summarized as follows:

- (1) By fitting field measurement data and laboratory experimental data, it is possible to validate that the proposed prediction equation can reasonably evaluate temperature-dependent resilient modulus of asphalt layers.
- (2) The theoretical method for establishing the physical state of each element is visually demonstrated. It can be seen that the proposed method can assign different physical states and resilient moduli to each element, including frozen state, recovering state, and unfrozen state.
- (3) It is evident that the As layer exhibits a varying resilient modulus distribution with depth, which is mainly attributed to temperature.
- (4) Resilient modulus increases as the depth increase due to the bulk stress of soils increasing, and the octahedral shear stress is weakened along with the depth. Under the center of wheel loads, the resilient modulus at the surface of base course layer changes significantly, which is due to the stress concentration in this area.
- (5) Freeze-thaw action and fluctuation in water content significantly impact the resilient modulus. In rainy days and thawing season, the sudden increase of water content leads to a significant decrease in the resilient modulus inside the pavement, which may seriously affect the fatigue life of the pavement. On the other hand, the resilient modulus in the pavement increases significantly in the freezing season.
- (6) While the As and base layers have thawed, the base layer has only thawed near the upper area, with most other parts still frozen. The degree of saturation near the

thawed base layer has increased, resulting in decreased resilient modulus near the upper area of the base layer. These results partially reflect the importance of evaluating the environmental impacts on the fatigue life of pavement structures in cold regions.

- (7) Both the MEPSCA and MEPDG can predict the resilient modulus of the pavement well. However, the MEPSCA method seems to calculate a daily representative resilient modulus, which can offer more precise and applicable results than a monthly representative value.

6 FATIGUE LIFE EVALUATION OF PAVEMENT CONSIDERING THE ENVIRONMENTAL IMPACTS

As discussed in the introduction, the TPSDM have some limitations, such as the lack of consideration of the environmental impacts on the base and subgrade layers, the lack of consideration of the effects of principal stress axis rotation, etc. In order to overcome these limitations, this chapter is based on the conclusions of Chapters 3 and 4 and replaces the constant elastic modulus of the base layer and subgrade layer with an elastic modulus related to the stress state and complex environmental impacts. Then, the commonly used MEPDG model was considered, and the influence of principal stress axis rotation was considered through multi-ring shear tests to modify the structure of the rutting failure criterion. The applicability of the modified design approach was examined by comparing the predicted fatigue life with the actual measured fatigue performance observed from the test pavement.

6.1 Analytical procedures

After conducting the mechanical analysis and getting the resilient modulus of each element, this section is to predict fatigue life of asphalt pavement against rutting and fatigue cracking with MEPSCA and improve it by introducing MEPDG rutting prediction model and PSAR effect. The process follows the flowchart shown in Figure 6-1.

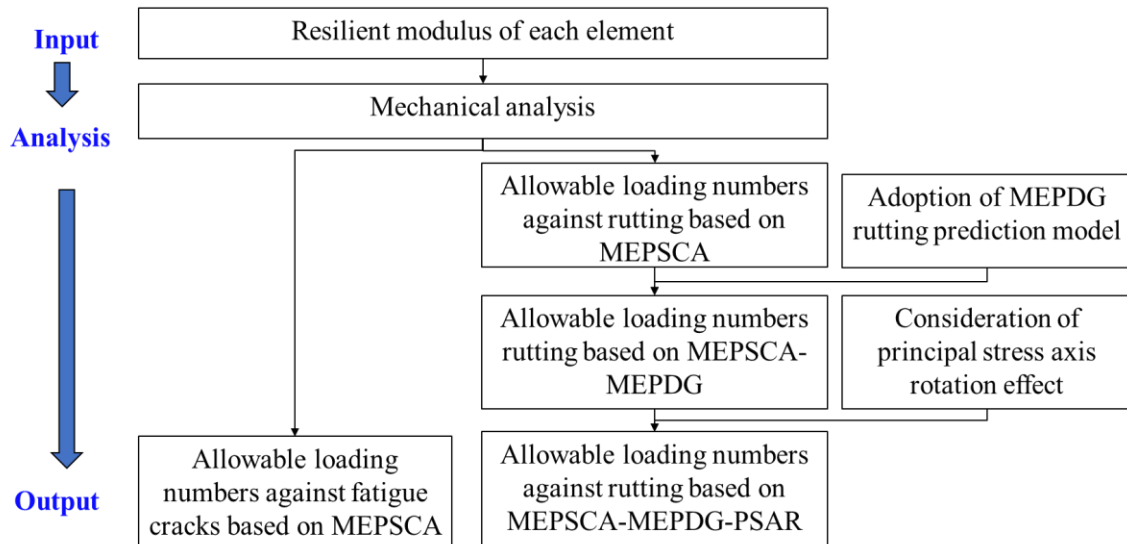


Figure 6-1 Flowchart of evaluating fatigue life.

6.2 Predicted fatigue life with TPSDM and MEPSCA

6.2.1 Fatigue life analysis of asphalt pavements

The TPSDM utilizes Equation (6-1)-Equation (6-3) and Equation (6-4)-Equation (6-11) to establish criteria for pavement failure caused by rutting and fatigue cracking (Japan Road Association, 2006). These criteria are then used to calculate the allowable numbers of equivalent 49-kN wheel loads against rutting (N_{fs}) and fatigue cracking (N_{fa}). The design process employs a TPSDM method that utilizes a simplified three-layered model consisting of the As, base course, and subgrade layers, as illustrated in Figure 6-2.

From the perspective of the mass conservation equation and energy conservation equation, the solutions of 2D and 3D models are similar under symmetric boundary conditions. However, in the process of calculating the mechanical response and fatigue life of the pavement, both 3D model should be considered. Although the 2D model can be faster and less computationally intensive, it is based on the assumption of plane strain, which means that there is no displacement in the longitudinal direction of the pavement. This means that the 2D model cannot reflect the real situation under the equivalent 49-kN wheel loads. Additionally, when considering the effect of PSAR, $(\tau_{yz})_{max}$ needs to be

obtained. Therefore, the 3D model was ultimately selected as the object of analysis, which is more reliable.

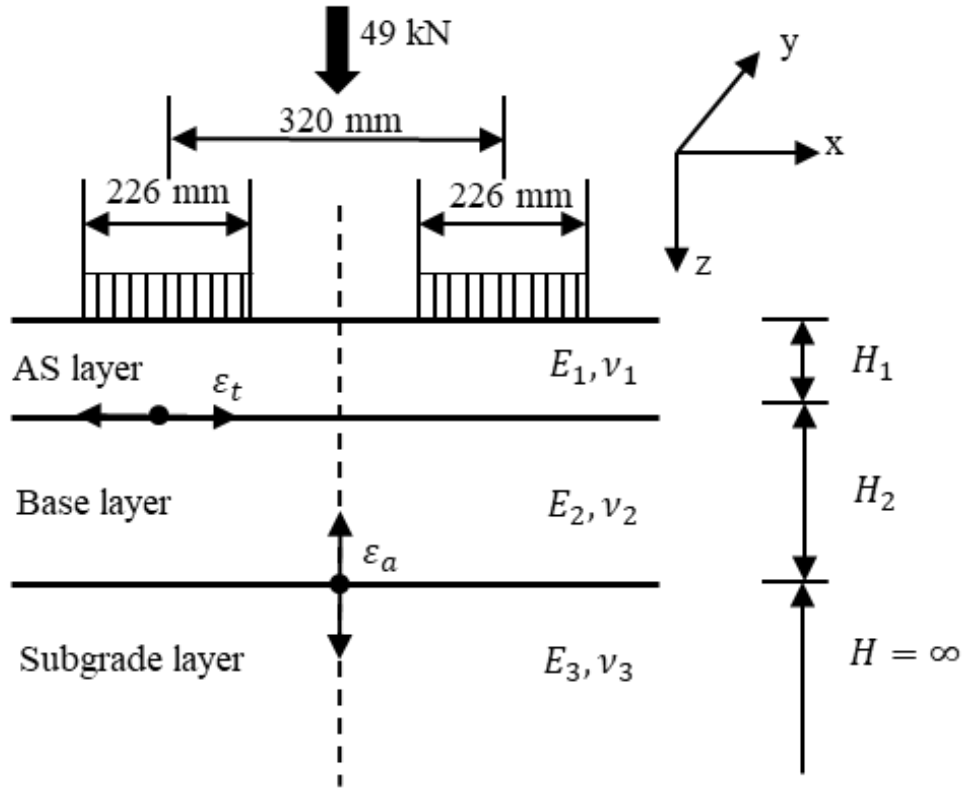


Figure 6-2 Three-layered model for allowable loading number calculation.

$$N_{fs} = \beta_{s1} \cdot \{1.365 \times 10^{-9} \cdot \varepsilon_a^{-4.477 \cdot \beta_{s2}}\} \quad (6-1)$$

$$\beta_{s1} = 2134 \quad (6-2)$$

$$\beta_{s2} = 0.819 \quad (6-3)$$

$$N_{fa} = \beta_{a1} \cdot C_a \cdot \{6.167 \times 10^{-5} \cdot \varepsilon_t^{-3.291 \cdot \beta_{a2}} \cdot E_1^{-0.854 \cdot \beta_{a3}}\} \quad (6-4)$$

$$C_a = 10^M \quad (6-5)$$

$$M = 4.84 \times \left(\frac{VFA}{100} - 0.69 \right) \quad (6-6)$$

$$\beta_{a1} = K_a \times \beta_{a1} \quad (6-7)$$

$$K_a = \begin{cases} \frac{1}{8.27 \times 10^{-11} + 7.83 \cdot e^{-0.11 H_a}}, & H_a < 18 \text{ cm} \\ 1, & H_a \geq 18 \text{ cm} \end{cases} \quad (6-8)$$

$$\beta_{a1} = 5.229 \times 10^4 \quad (6-9)$$

$$\beta_{a2} = 1.314 \quad (6-10)$$

$$\beta_{a3} = 3.018 \quad (6-11)$$

where β_{s1} , β_{s2} , β_{a1} , β_{a2} , and β_{a3} are the compensation rates for failure criteria based on the actual situation of Japanese pavement; C_a is the material parameter; M is a factor that relates the VFA to C_a ; VFA is Voids Filled with Asphalt; K_a is a correction factor, which relates to the thickness of asphalt mixture, H_a ; ε_a is the compressive strain on the top surface of the subgrade layer; and ε_t is the tensile strain on the lower surface of the As layer.

In the TPSDM, the monthly representative E_1 and constant E_2 and E_3 are used to calculate the allowable loading number under monthly temperature conditions (Japan Road Association, 2006). However, in contrast, the MEPSCA employs the resilient modulus that varies with environmental impacts and stress states to determine the daily allowable loading number. As a result, the failure loading number, $N_{f,s,i}$ and $N_{f,a,i}$ are calculated using Equation (6-12) and Equation (6-13), respectively, the primary difference being that k represents either months or days.

$$D_{a,s} = \sum_{i=1}^k \frac{N_i}{N_{f,a,i}} \quad (6-12)$$

$$N_{f,d} = \frac{1}{D_{a,s}} \quad (6-13)$$

where $D_{a,s}$ is damage rate; k is the number of environmental conditions, taken as 12 months in the TPSDM and 365 days in the MEPSCA.

6.2.2 Traffic volume observation

Between 1990 and 2004, CERI tracked the test pavement's traffic volume for the duration of its operation. Total traffic volume, defined as the average yearly daily number of vehicles (cars and trucks) in one lane, is 4974 per day per lane. The average yearly daily truck volume in one lane is 1714 trucks per day per lane. Wheel loads for all vehicles follow the standard distribution and vary from 15 to 80 kN. During the whole life of the test pavement, CERI converted the traffic volume to a 49-kN wheel load number of 2398 per

day per lane, because the Japanese design guide calculates the allowable number of equivalent 49-kN wheel loads for rutting and fatigue cracking.

6.3 Adoption of MEPDG rutting prediction model

Figure 6-3 shows the relationship between loading number, N_{fs} , and vertical strain, ε_a , in TPSDM model and MEPDG model. It is noted that N_{fs} -TPSDM model is much larger than N_{fs} -MEPDG model when ε_a locates between 50 to 550E-6, which is the normal range for ε_a . In other words, TPSDM model greatly overestimate the allowable loading number compares with MEPDG model. To overcome the limitations of the Japanese rutting failure criterion explained in the introduction, Lin et al. (2021) modified the failure criteria of the TPSDM (Equation (6-14) and Equation (6-15)), referring to the MEPDG rutting depth prediction model (Equation (1-2)). A logistic function is used to build the relation between β_m and ε_a , as shown in Figure 6-3. Within the logistic function, A_1 and A_2 are lower and upper limit separately and the A_1 is force as positive value. Similarly, this study introduced a daily adjustment parameter (β_m) to modify the MEPCA model and calculate allowable loading number against rutting, resulting in the development of the MEPSCA-MEPDG model.

$$N_{fs} = \beta_m \cdot \beta_{s1} \cdot \{1.365 \times 10^{-9} \cdot \varepsilon_a^{-4.477 \cdot \beta_{s2}}\} \quad (6-14)$$

$$\beta_m = A_2 + \frac{A_1 - A_2}{1 + (\varepsilon_a/x_0)^p} \quad (6-15)$$

where A_1, A_2 are lower and upper limits of β_m , equal to 0.00493 and 0.67672, respectively; x_0 is the fitting parameter, equal to 0.03; and p is fitting parameter, equal to 2.61871.

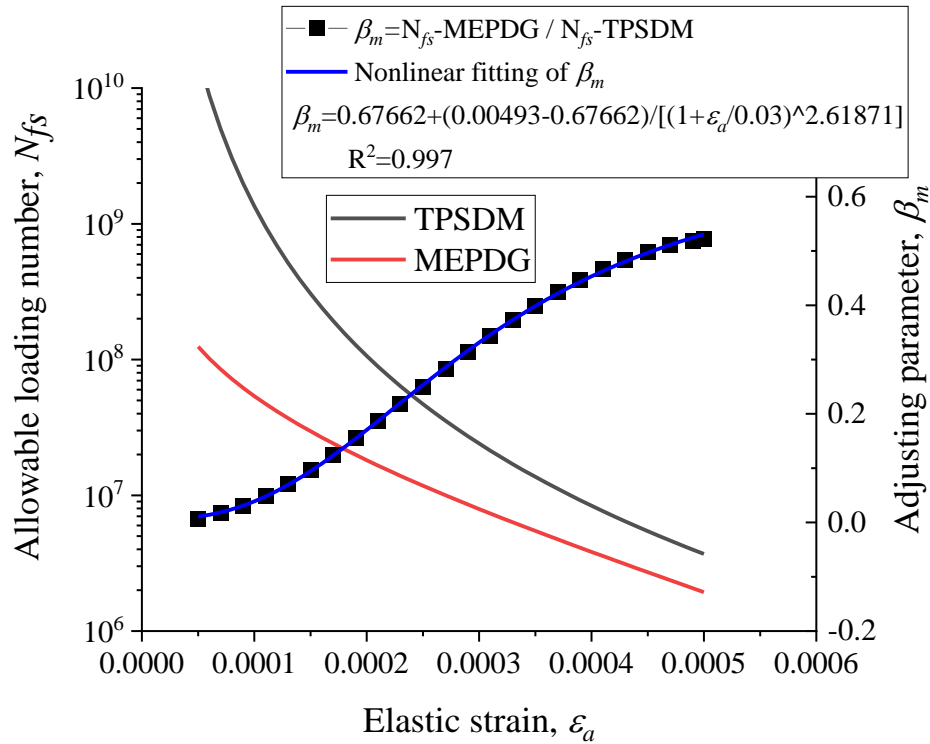


Figure 6-3 Allowable loading number calculated through TPSDM and MEPDG model.

The MEPSCA-MEPDG model is compared to the TPSDM and MEPSCA models, and the results are presented in Figure 6-4. As shown in Figure 6-4, the MEPSCA-MEPDG model can predict significantly smaller N_{fs} than the other two models. It is worth noting that the MEPSCA-MEPDG model has demonstrated its advantages over the other two models in predicting N_{fs} . However, there are still some deviations compared to the actual N_{fs} , which suggests that other factors that need to be identified may affect the mechanical response. It is important to continue refining and improving the model to minimize the deviations between predicted and actual results.

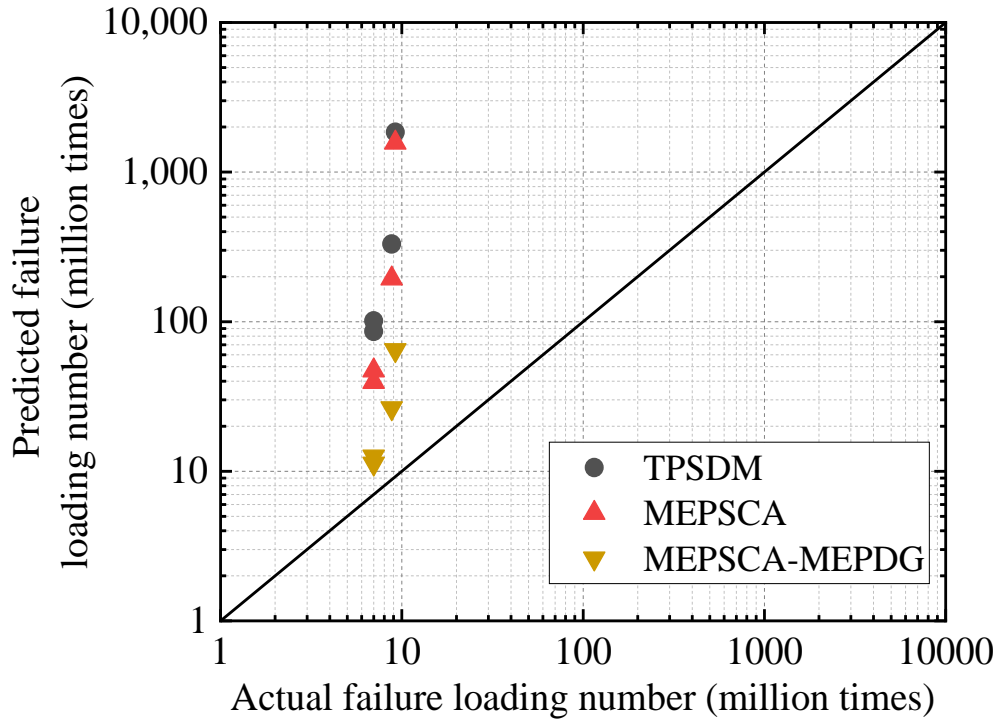


Figure 6-4 Predicted N_{fs} and actual failure loading number.

6.4 Consideration of principal stress axis rotation effect

The stress history of each pavement element varies based on its position, as shown in Figure 6-5. As the wheel loads approach the element under consideration, the principal stresses act obliquely, resulting in positive shear stress. This shear stress intensifies as the load approaches a specific point where the effect of oblique loading decreases and becomes zero when the load is directly above the element. Upon moving away from the element, the shear stress turns negative and increases as the principal stresses become oblique, decreasing as the load moves further away. In addition, the vertical stresses increase until the wheel load is above the element and decrease as it moves away from it.

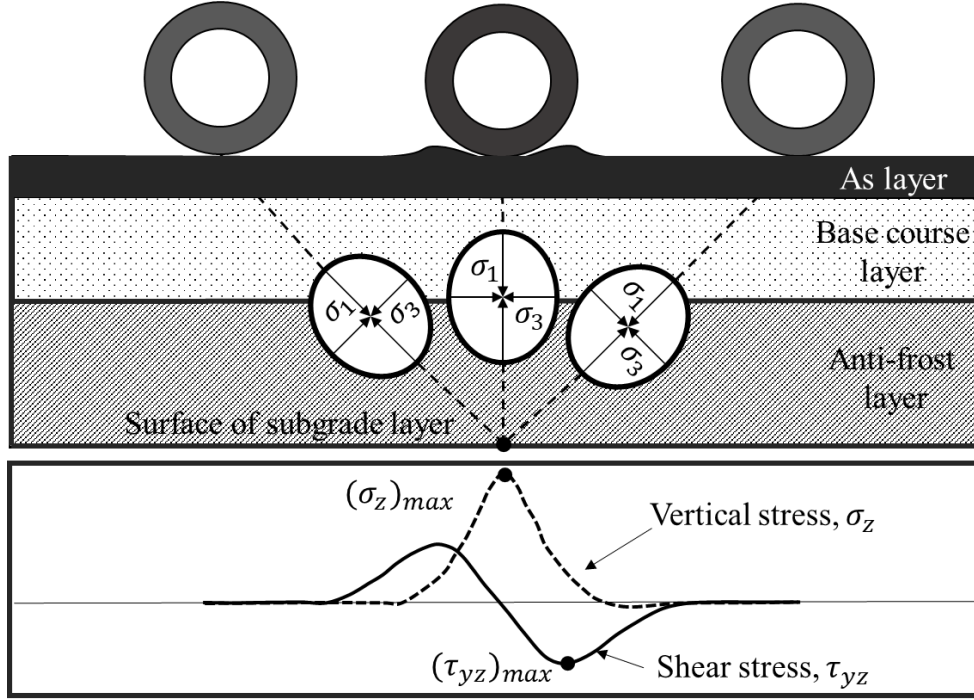


Figure 6-5 Stress variation of pavement under moving wheel loads.

To investigate the permanent strain amplification caused by principal stress axis rotation, Lin et al. conducted tests using a multi-ring shear apparatus and subsequently modified the proposed model using Equation (6-16) and Equation (6-17) (Lin et al., 2021). Based on the findings, the present study further modified the MEPCA-MEPDG model by incorporating daily axial strain ratios, resulting in the development of the MEPSCA-MEPDG-PSAR model.

$$(R_s)_{ave} = \exp(\beta_{PASR} \frac{(\tau_{yz})_{max}}{(\sigma_z)_{max}}) \quad (6-16)$$

$$N_{fs} = \beta_m \cdot \beta_{s1} \cdot \{1.365 \times 10^{-9} \cdot \varepsilon_a^{-4.477 \cdot \beta_{s2}}\} / (R_s)_{ave} \quad (6-17)$$

where $(R_s)_{ave}$ is the ratio of axial strain; $(\sigma_z)_{max}$ is the maximum vertical stress at surface of subgrade layer; $(\tau_{yz})_{max}$ is the maximum shear stress at surface of subgrade layer; and β_{PSAR} is the material constant.

Figure 6-6 illustrates the correction effect of the MEPSCA model, highlighting the significant amplification effect of the PSAR effect on the mechanical response of pavements. It indicates that the MEPSCA-MEPDG-PSAR model can predict values much closer to the actual fatigue life, thus affirming its reliability for predicting fatigue life. The

PSAR effect has demonstrated its potential to improve the accuracy of the proposed model, and it is vital to incorporate it into the model to refine predictions. It is worth noting that the MEPSCA-MEPDG-PSAR model helps to design pavements, avoiding the risks of over-design and under-design. In addition, according to the Japanese pavement design guide, when the predicted failure loading number is equal to the standard or actual failure loading number (Equation (6-18)), the reliability is 50%. This means that there is a 50% probability of failure when reaching the standard or actual failure fatigue life.

$$\frac{N_{f,p}}{\gamma_R} = N_{fa,d} \quad (6-18)$$

Where, $N_{f,p}$ is predicted failure loading number; $N_{fa,d}$ is standard failure loading number; γ_R is coefficient corresponding to the reliability, which is set according to Table 6-1.

Table 6-1 Reliability and coefficient corresponding to the reliability in Japanese pavement design guide.

Reliability	Coefficient corresponding to the reliability
50	1
60	1.3
70	1.8
80	2.6
90	4

This can provide reference for actual engineering. When below the solid black line, it means that the probability of failure is greater than 50%. For pavements with different reliability requirements, different verification lines should be selected to evaluate the design results.

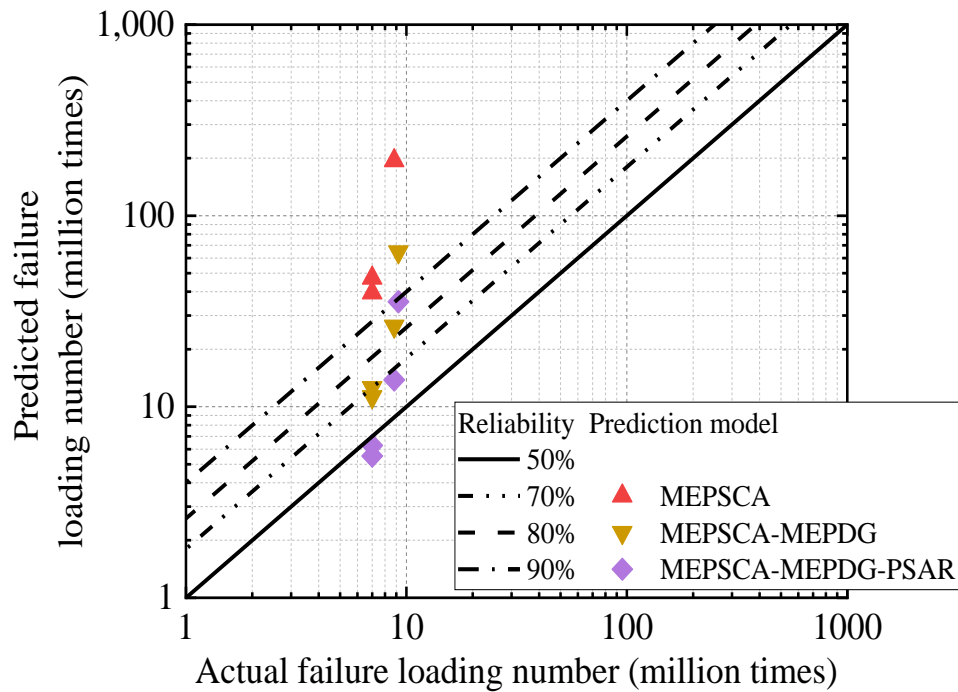


Figure 6-6 Predicted N_{fs} and actual failure loading number considering PSAR effect.

6.5 Comparison of fatigue life prediction

The three fatigue life prediction models mentioned earlier consider environmental impacts, the MEPDG rutting model, and the PSAR effect of modifying the current Japanese theoretical pavement structure design method. To enhance the clarity and comprehensiveness of the discussion on fatigue life prediction models for pavement structures, this section will summarize the various models developed previously. Additionally, Figure 6-7 and Figure 6-9 illustrate the values of N_{fs} and N_{fa} for the Bibi test pavement under these models, along with the reduction rate of fatigue life (R_{Nf}) and the absolute errors of the various prediction models. Figure 6-7 and Figure 6-9 provide a visual representation of the performance of the different models in predicting the fatigue life of pavement structures. R_{Nf} is used to represent the ratio of three modified models predicting fatigue life to the TPSDM predicting fatigue life, as defined in Equation (6-19). All R_{Nf} values are less than 1, indicating that environmental impacts, the MEPDG rutting prediction model, and PSAR effects will reduce the fatigue life of the pavement. ACC_{Nf} is used to evaluate the applicability of modified models, as defined in Equation (6-20).

$$R_{Nf} = \frac{N_f(\text{Modified model})}{N_f(\text{TPSDM})} \quad (6-19)$$

$$ACC_{Nf} = 1 - \left| \frac{N_f(\text{prediction}) - N_f(\text{Actual})}{N_f(\text{prediction})} \right| \quad (6-20)$$

As fatigue cracking failure was not observed in sections C and D during their service life, there is no actual measured N_{fa} for these two sections in the comparison results. Moreover, according to the results predicted by MEPDG, fatigue cracking failure did not occur in sections C and D. Nonetheless, the N_{fa} obtained from other sections provides valuable insights into the performance of the different fatigue life prediction models.

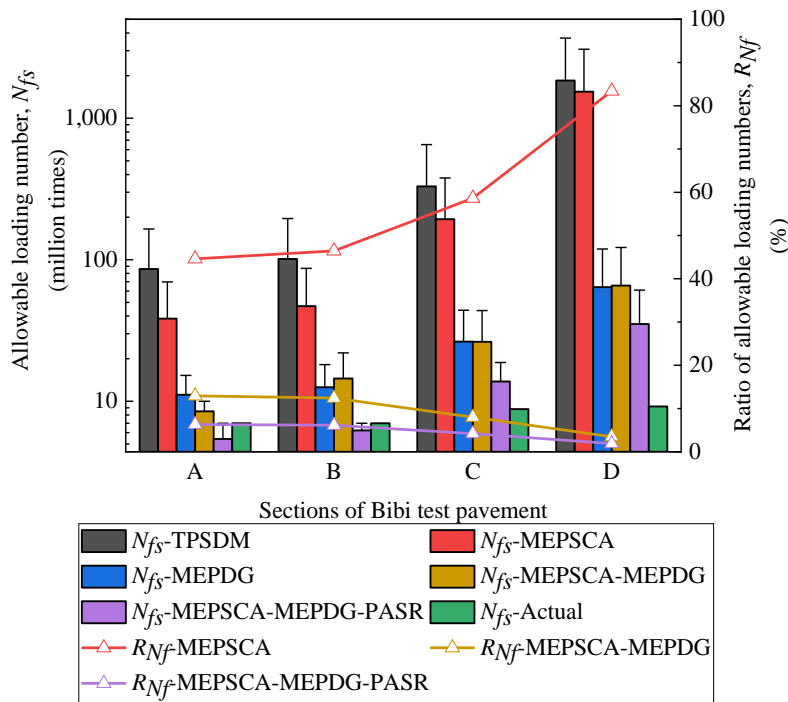


Figure 6-7 Comparison of N_{fs} for different sections under various fatigue life prediction models.

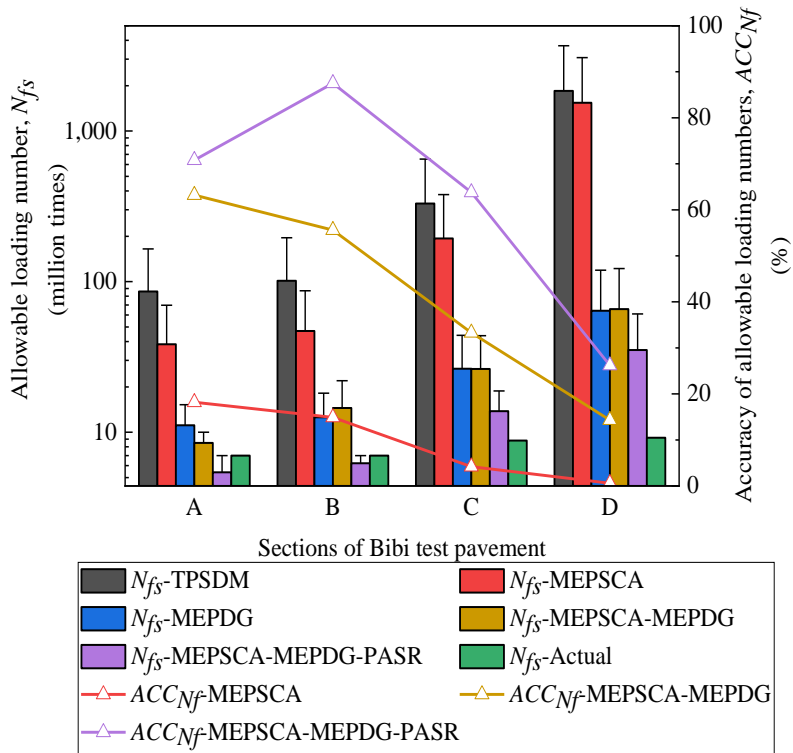


Figure 6-8 Comparison of ACC_{Nfs} for different sections under various fatigue life prediction models.

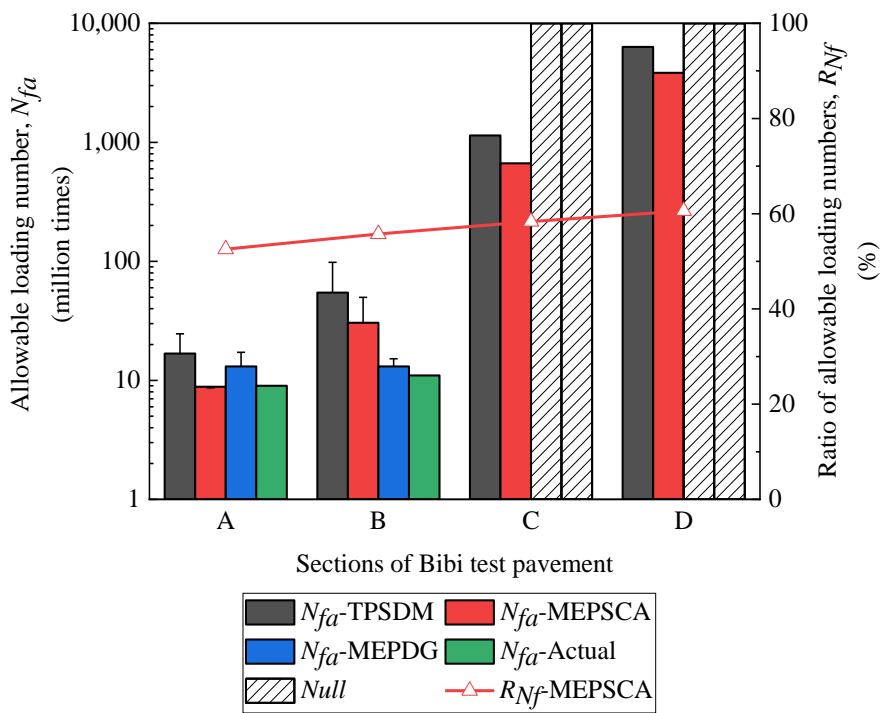


Figure 6-9 Comparison of N_{fa} for different sections under various fatigue life prediction models.

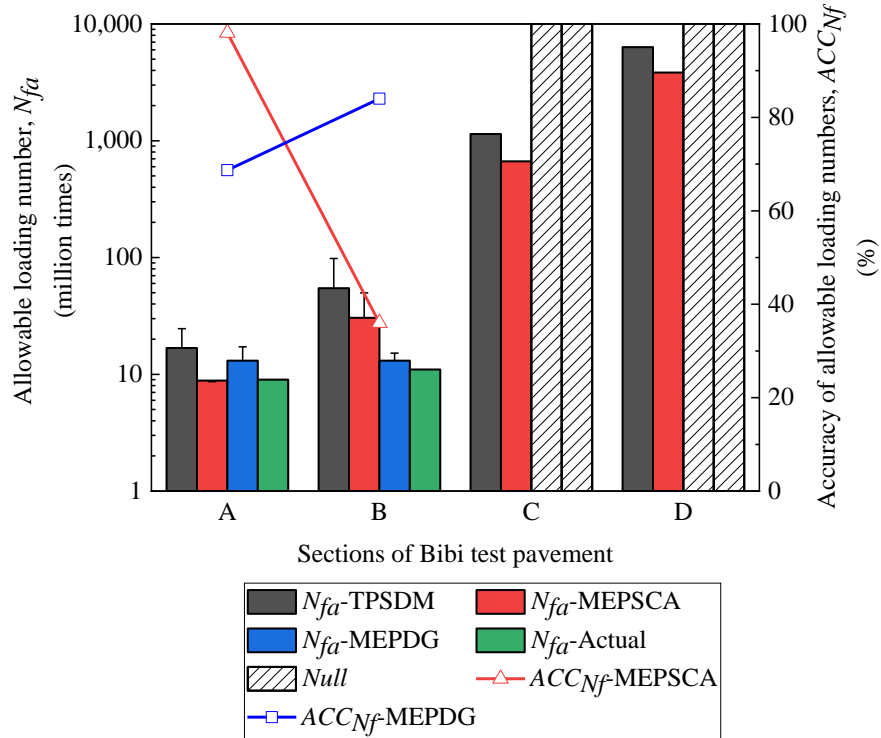


Figure 6-10 Comparison of ACC_{Nfa} for different sections under various fatigue life prediction models.

In the fatigue life against rutting calculation results, R_{Nf} for the MEPSCA, MEPSCA-MEPDG, and MEPSCA-MEPDG-PSAR models are around 58.3%, 9.2%, and 4.6%, respectively. The N_{fs} decreased by 41.7% when accounting for the environmental impacts. Furthermore, applying the MEPDG rutting prediction model further reduces the N_{fs} by 49.1%. Finally, considering the PSAR effect results in an additional decrease of 4.6% in the N_{fs} . From the comparison results of ACC_{Nfs} , MEPSCA-MEPDG-PSAR model has a better applicability in predicting N_{fs} . However, when predicting the fatigue life of pavement structures with a thick asphalt layer, the accuracy is low. This limitation needs to be improved in the future.

In the fatigue life against fatigue cracking calculation results, R_{Nf} caused by the environmental impacts is around 56.8%. In other words, the environmental impact on pavement materials decreases N_{fa} by about 43.2%. From the comparison results of ACC_{Nfa} , MEPDG and MEPSCA have a good applicability in predicting N_{fa} .

These results suggest that these prediction models enhance the applicability and effectiveness of TPSDM by accounting for environmental impacts and traffic load actions on pavement materials.

6.6 Summary

By replacing the constant elastic modulus of the pavement materials in the TPSDM with the resilient modulus related to the stress state and environmental impacts, this chapter calculate the fatigue life of pavements against rutting and fatigue cracking. The following findings can be mainly obtained in this chapter:

- (1) The environmental impacts, including water fluctuations and freeze-thaw action can reduce fatigue life against fatigue cracking by 43.2% and fatigue life against rutting by 41.7%, indicating a significant impact.
- (2) In addition, introducing the PSAR effect and the MEPDG rutting prediction model, the addition of daily axial strain ratio ($(R_s)_{ave}$), and daily adjustment parameter β_m to the rutting failure criterion further improve the prediction accuracy and applicability of the modified model.

7 CONCLUSIONS AND RECOMMENDATIONS

7.1 Conclusions and recommendations

This study explored the mechanical response and fatigue life prediction of asphalt pavement in cold regions through THM coupling simulation and proposed a comprehensive analytical procedure, as shown in Figure 7-1. Through the analysis of experimental data and the comparison of numerical simulation results, the following conclusions can be drawn:

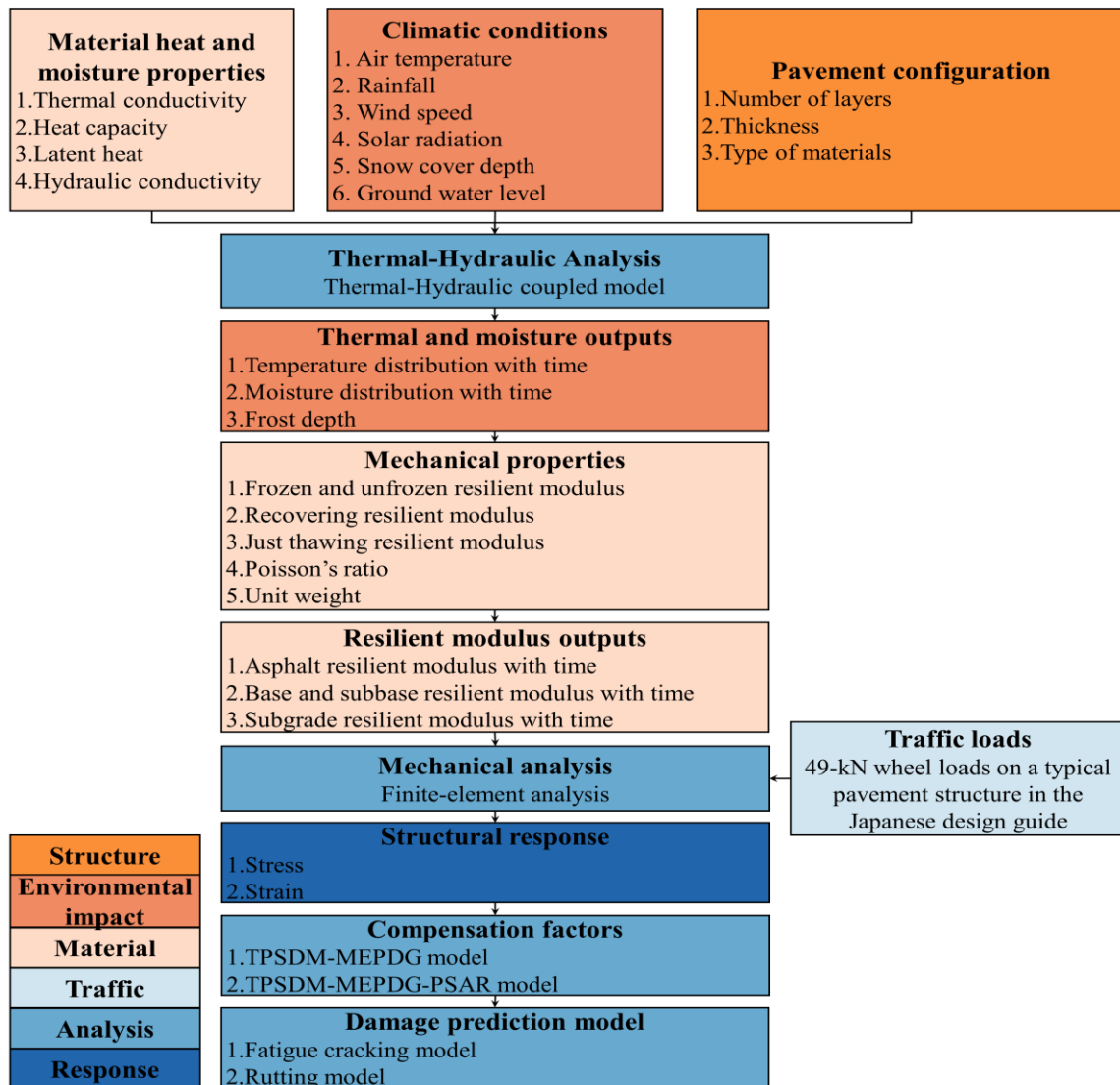


Figure 7-1 Scheme of the proposed MEPSCA

- (1) By comparing the simulation results with the measured data of ground temperature, frost-penetration depth, and degree of saturation, it can be concluded that the proposed THM simulation method can accurately reproduce the changes in temperature and water content of asphalt pavement, which is the prerequisite for accurately predicting the resilient modulus. The study also analyzed the environmental impacts that cause changes in the thermal and hydraulic fields of pavements and proposed corresponding methods to determine the physical state of each pavement element. These findings demonstrate the potential of THM simulation methods in better understanding physical processes.
- (2) Based on relevant experimental results, the relationship between resilient modulus, environmental impacts, physical state, and stress state can be established. The application of ODEs and weak-form PDEs can effectively address the challenge of geomaterials physical state changes and the cyclic dependency between resilient modulus, environmental impacts, and stress states. From the distribution of the resilient modulus in the selected typical five seasons, it can be found that the As layer shows a resilient modulus distribution varying with depth, which is mainly due to the ground temperature. In winter, the surface temperature is lower than the internal temperature, while in regular and thawing seasons, the surface temperature is higher than the internal temperature. For the base course layer, resilient modulus increases as the depth increase due to the bulk stress of soils increasing, and the octahedral shear stress is weakened along with the depth. Under the center of wheel loads, the resilient modulus at the surface of the base course layer changes significantly due to the stress concentration in this area.
- (3) The infiltration behavior of asphalt pavements can be evaluated through seepage analysis by considering hydraulic properties of As layer. It also concludes that single-phase flow model can adequately simulate pavement infiltration behavior and air flow does not seriously affect the infiltration behavior under low rainfall intensity.
- (4) Combining the time history curve of the resilient modulus, freeze–thaw action, and fluctuation in water content significantly impacts the resilient modulus. On rainy days and during the thawing season, the sudden increase in water content leads to

a significant decrease in the resilient modulus inside the pavement, which may seriously affect the fatigue life of the pavement. During partial thawing seasons, due to the decrease in permeability in the frozen area, a sandwich structure with reduced resilient modulus will be formed on the surface of the frozen area, which may seriously affect the fatigue life of pavements. On the other hand, the resilient modulus in the pavement increases significantly in the freezing season.

- (5) By replacing the constant elastic modulus of the pavement materials in the TPSDM with the resilient modulus related to the stress state and environmental impacts, the fatigue life of pavements against rutting and fatigue cracking is calculated. The results show that water fluctuations and freeze–thaw action will significantly reduce the fatigue life of the pavement in cold regions by reducing the resilient modulus of geomaterials. In addition, introducing the PSAR effect and the MEPDG rutting prediction model, the addition of daily axial strain ratio $((R_s)_{ave})$, and daily adjustment parameter β_m to the rutting failure criterion further improve the prediction accuracy and applicability of the modified model.

This study highlights the importance of understanding the mechanical response and fatigue life prediction of asphalt pavement in cold regions through THM coupling simulation. The findings of this study can be used to improve the design of asphalt pavements in cold regions and to prevent issues of over-design and under-design.

7.2 Future assignments

The proposed method provides a framework for continuous improvement, and it is recommended to conduct further and more comprehensive research to improve the model. There are a number of problems that require further investigation.

- (1) The proposed THM coupling model only considers the change in resilient modulus caused by the variation of matric suction during the freeze-thaw process. Simulation of frost heave and thaw settlement is not included. In fact, it is widely believed that displacement changes caused by frost heave and thaw settlement can lead to serious pavement damage, thereby reducing the fatigue life of the pavement. It is necessary

to continue exploring the impact of frost heave and thaw settlement on pavement fatigue life.

- (2) When predicting the fatigue life of pavement structures with a thick asphalt layer, the accuracy is low in this study. It is necessary to further investigate the impact of pavement structure on fatigue life.
- (3) Currently, many drainage materials are being applied in pavement engineering. Practice has shown that these measures effectively reduce the accumulation of moisture within the pavement. Therefore, in order to effectively evaluate such designs, it is necessary to improve the geometric models in simulations and add more material properties.

LIST OF NOTATIONS

Description	Symbol
Regression constants	$k_1, k_2, k_3,$ k_4
Atmospheric pressure	p_a
Bulk stress	θ
Octahedral shear stress	τ_{oct}
Permanent strain for the layer/sub-layer	$\varepsilon_p(N)$
Number of traffic repetitions	N
Material property	ε_0
Material property	β
Material property	ρ
Resilient strain imposed in laboratory testing	ε_r
Average vertical resilient strain in the layer, which is calculated by a multi-layer elastic pavement response model	ε_v
Calibration factor for the unbound granular and subgrade materials	β_1
Global calibration coefficient	K_1
Octahedral normal stress	σ_{oct}
Matric suction	ψ
Net mean stress	σ_{net}
Volumetric water content	$\frac{V_w}{V_t}$
Unit weight of material normalized by the unit weight of water	$\frac{\gamma}{\gamma_w}$
First principal stress	σ_1
Second principal stress	σ_2
Third principal stress	σ_3

First stress invariant	I_1
Saturation factor	f'
Deviator stress	σ_d
Volumetric water content	θ'
Model parameters	A, B, C, D
Normalizing reference stress	p_0
Specific moisture capacity of soil	C_H
Pore-water pressure	u_w
Coefficient of water permeability	k_w
Total hydraulic potential head	h
Porosity	n
Density of water	ρ_w
Density of ice	ρ_i
Degree of saturation for ice	S_i
Time	t
Sink/source term of mass	f_w
Apparent heat capacity of soil	C_{Ta}
Latent heat of fusion of water	L
Thermal conductivity of soil	λ_T
Volumetric heat capacity of water	C_{Tw}
Flux vector of water	\mathbf{v}_w
Sink/source term of energy	f_e
Temperature	T
Stress tensor	$\{\sigma\}$
Elastic strain tensor	$\{\varepsilon\}$
Initial stress	$\{\sigma_0\}$
Initial strain	$\{\varepsilon_0\}$

Stiffness matrix	$[D]$
Elastic modulus (resilient modulus)	E
Poisson's ratio	μ
Permeability of saturated soil	k_s
Relative hydraulic conductivity	k_{wr}
Effective degree of saturation	S_e
Degree of saturation	S_r
Residual degree of saturation	S_{rr}
Saturated degree of saturation	S_{rs}
VG model fitting parameters	$\alpha, m, \lambda,$
Heat conductivity of soil particles	λ_s
Heat conductivity of ice	λ_i
Heat conductivity of water	λ_w
Volumetric water content	θ_w
Volumetric heat capacity of soil particles	C_{Tp}
Volumetric heat capacity of ice	C_{Ti}
Nominal freezing temperature	T_0
Pore-water pressure (suction) before freezing	u_{w0}
Precipitation	P_{in}
Rainfall	P_{rain}
Snow-melt water equivalent	$SMWE$
Snow density	ρ_{snow}
Value of decreasing snow depth per day	Δd_{sn}
Snow depth	d_{sn}
DOY	t_1
Time in hours measured from the lying snow exist	t_2
A number from -92 (1st October) to +181 (30th June)	DOY

Total daily radiation	Q
Net short-wave radiation received	q_s
Absorptivity of the pavement surface to solar radiation	α_s
Emitted radiation	q_{er}
The Stefan-Boltzman constant	ζ
Surface emissivity	ϵ_s
Temperature of the ground surface	T_s
Temperature of the atmosphere	T_a
Heat extraction by convection	q_c
Convective heat transfer coefficient	h_c
Wind speed	U
The energy flux through the snow	q_{sn}
Thermal conductivity of snow cover	λ_{sn}
Depth from the air temperature boundary	z
Temperature at any depth and time	T_z
Mean annual ground surface temperature	T_m
Ground surface temperature amplitude	A_z
Initial phase	φ
Period (day)	p_d
Thermal diffusivity	α_u
Period (hour)	p_h
Depth	z_1
Depth	z_2
Observed annual temperature range at the depth of z_1	T_{z1}
Observed annual temperature range at the depth of z_2	T_{z2}
Dry density of soil	ρ_d
Saturated volume fraction	θ_s

Residual volume fraction	θ_r
The effective saturation of water and air, respectively	$S_{e,w}, S_{e,g}$
The intrinsic permeability of a given porous medium	κ_{int}
The relative permeability of water and air, respectively	$k_{r,w}, k_{r,g}$
The dynamic viscosity of water and air, respectively	ν_w, ν_g
Pressure of water and air, respectively	p_w, p_g
Density of air	ρ_g
The coordinate (for example, x, y) of vertical elevation	$D_{x,y}$
Capillary pressure	p_c
Capillary pressure in terms of pressure head	h_c
Specific capacity of air	C_G
The saturated coefficient of permeability of water and dry air permeability, respectively.	k_{ws}, k_{gs}
A curve fitting parameter related to pore-size distribution	m'
Density	ρ'
The volumetric flow rate of water and air, respectively.	Q_w, Q_g
Monthly mean temperature of asphalt mixture at depth of h_1	M_p
Depth equals to one-third of the height of asphalt mixture	h_1
Elastic modulus of As layer	E_1
Average temperature of As layer	T_1
Regression constants	a, b, c, d
Climatic factor	F_{clim}
Total bulk stress	σ_{ii}
Pore air pressure	u_a
Loading frequency	f
Predicted resilient modulus at any frequency (f)	$E(f)$
Frequency effect	$F(\psi)$

Resilient modulus of base course material obtained at $f = 50$ Hz	$E_2(50Hz)$
Resilient modulus of base course material obtained at $f = 50$ Hz	$E_3(50Hz)$
Resilient modulus of subgrade soil obtained at $f = 10$ Hz	$E_2(10Hz)$
Resilient modulus of subgrade soil obtained at $f = 0.2$ Hz	$E_3(0.2Hz)$
Resilient modulus in frozen state	M_{rF}
Resilient modulus in recovering state	M_{rR}
Resilient modulus in unfrozen state	M_{rU}
Resilient modulus in just thawing state	M_{rmin}
Recovery ratio	RR
The number of days elapsed from thawing started in numerical simulation	$T_{R,S}$
The number of days required for a given geomaterial from thawed state to unfrozen state	T_R
The minimum of climatic factor during just thawing state	$F_{clim,min}$
The percent passing the No. 200 sieve (0.075mm)	P_{200}
Plasticity index	PI
Intermediate variables	IV_0, IV_1 IV_2, IV_3
Accuracy	ACC
The measured resilient modulus of i -th measurement	u_i
The simulated resilient modulus of i -th measurement	z_i
The number of measurements	N'
The allowable numbers of equivalent 49-kN wheel loads against rutting	N_{fs}
The allowable numbers of equivalent 49-kN wheel loads against fatigue cracking	N_{fa}
The compensation rates for failure criteria based on the actual situation of Japanese pavement	$\beta_{s1}, \beta_{s2},$ $\beta_{a1}, \beta_{a2},$ β_{a3}

Material parameter	C_a
A factor that relates the <i>VFA</i> to C_a	M
Voids Filled with Asphalt	<i>VFA</i>
A correction factor	K_a
The thickness of asphalt mixture	H_a
Compressive strain on the top surface of the subgrade layer	ε_a
Tensile strain on the lower surface of the As layer	ε_t
The number of environmental conditions	k
Damage rate	$D_{a,s}$
Lower and upper limits of β_m	A_1, A_2
Daily adjustment parameter	β_m
Fitting parameter	x_0, p
Ratio of axial strain	$(R_s)_{ave}$
Maximum vertical stress at surface of subgrade layer	$(\sigma_z)_{max}$
Maximum shear stress at surface of subgrade layer	$(\tau_{yz})_{max}$
Material constant	β_{PSAR}
Predicted failure loading number	$N_{f,p}$
Standard failure loading number	$N_{fa,d}$
Coefficient corresponding to the reliability	γ_R
The accuracy of allowable loading number	ACC_{Nf}
The reduction rate of allowable loading number	R_{Nf}

LIST OF REFERENCES

- [1] Japan Meteorological Agency, Automated meteorological data acquisition system. <https://www.jma.go.jp/jp/amedas/>, 2020 (accessed 5 December 2020).
- [2] AASHTO. Mechanistic-empirical pavement design guide: A manual of practice. Washington: American Association of State Highway and Transportation Officials; 2008.
- [3] AASHTOWare Pavement ME Design. AASHTOWare® v.2.6 (Version 2.6). Champaign; 2021. <https://me-design.com/MEDesign/>.
- [4] Abdullah GM. Performance of enhanced problematic soils in roads pavement structure: Numerical simulation and laboratory study. *Sustainability* 2023;15:2595.
- [5] Andersland OB, Ladanyi B. Frozen ground engineering. 2nd ed. Jersey: John Wiley & Sons; 2003.
- [6] Barksdale RD. Laboratory evaluation of rutting in base course materials. *The Third International Conference on the Structural Design of Asphalt Pavements* 1972;1:161-174.
- [7] Bear J. Dynamics of fluids in porous media. New York: American Elsevier Publishing Company; 1972.
- [8] Bras RL. Hydrology: An introduction to hydrologic science. Boston: Addison Wesley Publishing Company; 1990.
- [9] Chow LC, Mishra D, Tutumluer E. Framework for development of an improved unbound aggregate base rutting model for mechanistic–empirical pavement design. *Transportation Research Record* 2014;2401:11-21.
- [10] Christopher BR, Schwartz CW, Boudreaux R, Berg RR. Geotechnical aspects of pavements. United States. Federal Highway Administration, 2006;
- [11] Clayton C. Stiffness at small strain: Research and practice. *Geotechnique* 2011;61:5-37. <https://doi.org/10.1680/geot.2011.61.1.5>.
- [12] Cole DM, Irwin LH, Johnson TC. Effect of freezing and thawing on resilient modulus of a granular soil exhibiting nonlinear behavior. *Transportation Research Record* 1981;809:809-818.
- [13] COMSOL Multiphysics. COMSOL multiphysics® v.6.1 (Version 6.1). Stockholm; 2021. www.comsol.com.
- [14] Côté J, Konrad JM. A generalized thermal conductivity model for soils and construction materials. *Canadian Geotechnical Journal* 2005;42:443-458. <https://doi.org/10.1139/t04-106>.

- [15] Crockford W. Modeling stress and strain states in pavement structures incorporating thick granular layers. Texas Transformation Institute; 1990.
- [16] Dai S, Boerner D, Isackson C. Failure analysis of flexible pavement section on mn/road 2007;
- [17] Dall'Amico M, Endrizzi S, Gruber S, Rigon R. A robust and energy-conserving model of freezing variably-saturated soil. *The Cryosphere* 2011;5:469-484. <https://doi.org/10.5194/tc-5-469-2011>.
- [18] David M P, Lidiya Z. Finite element analysis in geotechnical engineering: Theory. 1st ed. London: Thomas Telford; 1999.
- [19] De Vries DA. Simultaneous transfer of heat and moisture in porous media. *Transactions American Geophysical Union* 1958;39:909-916. <https://doi.org/10.1029/TR039i005p00909>.
- [20] Doré G, Zubeck HK. Cold regions pavement engineering. 1st ed. VA: ASCE press; 2009.
- [21] Endo A. A question of snow density and maximum snow depth. *Journal of Japan Association for Snow Engineering* 1986:23-30. [in Japanese].
- [22] Fan Y, Wu Y, Chen H, Liu S, Huang W, Wang H, Yang J. Performance evaluation and structure optimization of low-emission mixed epoxy asphalt pavement. *Materials* 2022;15:6472.
- [23] Fredlund DG, Rahardjo H, Fredlund MD. *Unsaturated soil mechanics in engineering practice*. John Wiley & Sons; 2012.
- [24] Furuki T, Ishikawa T, Kobe H, Ochi Y. Proposal of capillary barrier system by size optimization of asphalt pavement. Annual Meeting of the JGS Hokkaido branch 2022;62:67-76. [in Japanese].
- [25] Gräbe P, Clayton C. Effects of principal stress rotation on permanent deformation in rail track foundations. *Journal of Geotechnical and Geoenvironmental Engineering* 2009;135:555-565. [https://doi.org/10.1061/\(ASCE\)1090-0241\(2009\)135:4\(555\)](https://doi.org/10.1061/(ASCE)1090-0241(2009)135:4(555)).
- [26] Hansson K, Šimunek J, Mizoguchi M, Lundin L-C, Van Genuchten MT. Water flow and heat transport in frozen soil: Numerical solution and freeze–thaw applications. *Vadose Zone Journal* 2004;3:693-704.
- [27] Harlan R. Analysis of coupled heat–fluid transport in partially frozen soil. *Water Resources Research* 1973;9:1314-1323.
- [28] Huurman M. Permanent deformation in concrete block pavements. 1997;
- [29] Inam A, Ishikawa T, Miura S. Effect of principal stress axis rotation on cyclic plastic deformation characteristics of unsaturated base course material. *Soils and Foundations* 2012;52:465-480. <https://doi.org/10.1016/j.sandf.2012.05.006>.

- [30] Ishikawa T, Kawabata S, Kameyama S, Abe R, Ono T. Effects of freeze-thawing of granular base on fatigue life of pavement and its evaluation. *Journal of Japan Society of Civil Engineers* 2011a;67:109-116. [in Japanese].
- [31] Ishikawa T, Lin T, Kawabata S, Kameyama S, Tokoro T. Effect evaluation of freeze-thaw on resilient modulus of unsaturated granular base course material in pavement. *Transportation Geotechnics* 2019a;21:100284. <https://doi.org/10.1016/j.trgeo.2019.100284>.
- [32] Ishikawa T, Lin T, Yang J, Tokoro T, Tutumluer E. Application of the UIUC model for predicting ballast settlement to unsaturated ballasts under moving wheel loads. *Transportation Geotechnics* 2019b;18:149-162. <https://doi.org/10.1016/j.trgeo.2018.12.003>.
- [33] Ishikawa T, Miura S, Sekine E. Development and performance evaluation of multi-ring shear apparatus. *Development and Performance Evaluation of Multi-ring Shear Apparatus*; 2007.
- [34] Ishikawa T, Sekine E, Miura S. Cyclic deformation of granular material subjected to moving-wheel loads. *Canadian Geotechnical Journal* 2011b;48:691-703. <https://doi.org/10.1139/t10-099>.
- [35] Itani SY. 1990. *Behavior of base materials containing large sized particles*, Georgia Institute of Technology.
- [36] Japan Road Association. *Pavement design manual*. Tokyo: Japan Road Association; 2006. [in Japanese].
- [37] Johnson TC, Cole DM, Chamberlain EJ. Influence of freezing and thawing on the resilient properties of a silt soil beneath an asphalt concrete pavement. U.S. Cold Regions Research and Engineering Laboratory, CRREL Report 1978;78:23.
- [38] Johnston GH, Ladanyi B, Morgenstern NR, Penner E. Engineering characteristics of frozen and thawing soils. In: Johnston GH, editors. *Permafrost engineering design and construction*. Toronto: John Wiley Sons; 1981.
- [39] Jong D-T, Bosscher PJ, Benson CH. Field assessment of changes in pavement moduli caused by freezing and thawing. *Transportation Research Record* 1998;1615:41-48.
- [40] Kabir T, Tighe S. Construction and performance evaluation of polyurethane-bound porous rubber pavement (prp) trial section in the cold climate. *Sustainability* 2023;15:2413.
- [41] Kaneko H, Ishikawa T, Nakamura T, Kishitani I, Hiramatsu K. Effect of ageing on rainfall infiltration characteristics of unsaturated granular roadbeds. *Annual Meeting of the JGS Hokkaido branch* 2021;61:165-172. [in Japanese].

- [42] Kim DS, Kweon GC, Lee KH. Alternative method of determining resilient modulus of compacted subgrade soils using free-free resonant column test. *Transportation Research Record* 1997;1577:62-69. <https://doi.org/10.3141/1577-08>.
- [43] Konrad J-M, Morgenstern NR. A mechanistic theory of ice lens formation in fine-grained soils. *Canadian Geotechnical Journal* 1980;17:473-486.
- [44] Korkiala-Tanttu L. Verification of rutting calculation for unbound road materials. *Proceedings of the institution of civil engineers-transport* 2009;162:107-114.
- [45] Lekarp F, Dawson A. Modelling permanent deformation behaviour of unbound granular materials. *Construction and Building Materials* 1998;12:9-18. [https://doi.org/10.1016/S0950-0618\(97\)00078-0](https://doi.org/10.1016/S0950-0618(97)00078-0).
- [46] Lin T, Ishikawa T, Luo B. Applicability of modified university of illinois at urbana-champaign model for unbound aggregate material with different water content. *Transportation Research Record* 2019a;2673:439-449. <https://doi.org/10.1177/0361198119827530>.
- [47] Lin T, Ishikawa T, Maruyama K, Tokoro T. Pavement design method in Japan with consideration of climate effect and principal stress axis rotation. *Transportation Geotechnics* 2021;28:100552. <https://doi.org/10.1016/j.trgeo.2021.100552>.
- [48] Lin T, Ishikawa T, Tokoro T. Testing method for resilient properties of unsaturated unbound granular materials subjected to freeze-thaw action. *Japanese Geotechnical Society Special Publication* 2019b;7:576-581.
- [49] Lin T, Ishikawa T, Yang J, Tokoro T. Evaluation of climate effect on resilient modulus of granular subgrade material. *Cold Regions Science and Technology* 2022;194:103452. <https://doi.org/10.1016/j.coldregions.2021.103452>.
- [50] Liu Z, Yu X. Coupled thermo-hydro-mechanical model for porous materials under frost action: Theory and implementation. *Acta Geotechnica* 2011;6:51-65.
- [51] Lytton R. Foundations and pavements on unsaturated soils. *Proceedings of the first international conference on unsaturated soils* 1996;
- [52] Maruyama K, Abe R, Kumagai M. Development of mechanistic-empirical asphalt pavement design method for cold regions. *Monthly Bulletin of Civil Engineering Research Institute* 2012:2-13.
- [53] Maruyama K, Tako J, Kasahara A. Long-term performance of asphalt pavements at bibi new test road. *J JSCE E* 2006;62:519-530. [in Japanese].
- [54] Maruyama K, Tako J, Kasahara A. Fatigue failure life prediction method of asphalt pavement. *Jpn Soc Civ Eng Annu Meet E* 2008;64:416-426.
- [55] Miner MA. Cumulative damage in fatigue. *Journal of Applied mechanics* 1945; <https://doi.org/10.1115/1.4009458>.

- [56] Miura K, Miura S, Toki S. Deformation behavior of anisotropic dense sand under principal stress axes rotation. *Soils and Foundations* 1986;26:36-52. <https://doi.org/10.3208/sandf1972.26.36>.
- [57] Monismith CL, Hicks RG, Salam Y. Basic properties of pavement components 1971;
- [58] Monismith CL, Ogawa N, Freeme C. Permanent deformation characteristics of subgrade soils due to repeated loading. *Transportation Research Record* 1975;
- [59] Murakami T, Ishikawa T, Binh NT, Mori A, Yokota S. Prediction of slope failure in cold regions induced by a rainfall during snowmelt period. *Proceedings of the 16th International Conference on Computer Methods and Advances in Geomechanics* 2022;2:457-465. https://doi.org/10.1007/978-3-030-64518-2_54.
- [60] NCHRP. Guide for mechanistic-empirical design of new and rehabilitated pavement structures. Washington: National Cooperative Highway Research Program; 2004.
- [61] Ng CWW, Zhou C, Yuan Q, Xu J. Resilient modulus of unsaturated subgrade soil: Experimental and theoretical investigations. *Canadian Geotechnical Journal* 2013;50:223-232.
- [62] O'Neill K, Miller RD. Exploration of a rigid ice model of frost heave. *Water Resources Research* 1985;21:281-296.
- [63] Oliver JE. *Climate and man's environment: An introduction to applied climatology*. 1978;
- [64] Paute J, Hornych P, Benaben J. Repeated load triaxial testing of granular materials in the french network of laboratories des ponts et chaussées. *FLEXIBLE PAVEMENTS. PROCEEDINGS OF THE EUROPEAN SYMPOSIUM EUROFLEX 1993 HELD IN LISBON, PORTUGAL, 20-22 SEPTEMBER 1993* 1996;
- [65] Pavement Engineering Committee. *FWD and small FWD operational guide*. 3rd ed. Tokyo: JSCE press; 2002. [in Japanese].
- [66] Pavement Engineering Committee. *Problems and countermeasures of pavement in snowy cold regions*. 1st ed. Tokyo: JSCE Press; 2016. [in Japanese].
- [67] Peng J, Zhang J, Li J, Yao Y, Zhang A. Modeling humidity and stress-dependent subgrade soils in flexible pavements. *Computers and Geotechnics* 2020;120:103413.
- [68] Perić D, Goh G, Saeidaskari J, Rashk Olia AS, Ayar P. Development of prediction models for performance of flexible pavements in kansas with emphasis on the effects of subgrade and unbound layers. *Sustainability* 2022;14:9020.
- [69] Pezo RF. A general method of reporting resilient modulus tests of soils, a pavement engineer's point of view. *72nd Annual Meeting of the TRB* 1993;
- [70] Puppala AJ. Estimating stiffness of subgrade and unbound materials for pavement design. *Transportation Research Board*; 2008.

- [71] Ren D, Ishikawa T, Si J, Tokoro T. Effect of hysteresis of soil-water characteristic curve on resilient modulus of subgrade soil under different climatic and stress conditions. Transportation Research Board 102nd Annual Meeting 2023.
- [72] Richards LA. Capillary conduction of liquids through porous mediums. ArXiv Physics e-prints 1931;1:318-333.
- [73] Saeed A, Hall Jr J, Barker W. Performance-related tests of aggregates for use in unbound pavement layers. 2001.
- [74] Seed H, Mitry F, Monismith C, Chan C. Factors influencing the resilient deformations of untreated aggregate base in two-layer pavements subjected to repeated loading. Highway Research Record 1967;190:19-57.
- [75] Seed HB, Chan CK, Monismith CL. Effects of repeated loading on the strength and deformation of compacted clay. Highway research board proceedings 1955;34:541-558.
- [76] Shackel B. Repeated loading of soils-a review. Australian Road Research 1973;5
- [77] Shao J, Lister P, McDonald A. A surface-temperature prediction model for porous asphalt pavement and its validation. Meteorological Applications 1994;1:129-134.
- [78] Sheppard M, Kay B, Loch J. Development and testing of a computer model for heat and mass flow in freezing soils. International conference on permafrost 1978:75-81.
- [79] Shinme R, Yamashita S. Hydrologic measurement using snowcover weightmeter in winter. Proceedings of Hydraulic Engineering 2008;52:493-498. <https://doi.org/10.2208/prohe.52.493>. [in Japanese].
- [80] Si J, Ishikawa T, Maruyama K, Ueno C. Evaluation of resilient modulus of asphalt pavement in cold region based on thermo-hydro-mechanical coupling simulation. Annual Meeting of the JGS Hokkaido branch 2022;62:97-106.
- [81] Simonsen E, Isacsson U. Thaw weakening of pavement structures in cold regions. Cold Regions Science and Technology 1999;29:135-151.
- [82] Simonsen E, Isacsson U. Soil behavior during freezing and thawing using variable and constant confining pressure triaxial tests. Canadian Geotechnical Journal 2001;38:863-875.
- [83] Simonsen E, Janoo VC, Isacsson U. Resilient properties of unbound road materials during seasonal frost conditions. Journal of Cold Regions Engineering 2002;16:28-50.
- [84] Takahashi S, Ono Y, Sato M. Field survey to identify the important key factors for long term durability of asphalt pavement on expressways in Japan. Jpn Soc Civ Eng Annu Meet E 2015;71:93-101. <https://doi.org/10.2208/jscejpe.71.I.93>. [in Japanese].

- [85] Takeichi K, Kubo H, Kasahara A. A pavement design for low-volume roads that considers the antifrost effects of thickly packed snow. *Transportation Research Record* 1987;1:237.
- [86] Tangella SR, Craus J, Deacon J, Monismith C. Summary report on fatigue response of asphalt mixtures 1990;
- [87] Tseng K-H, Lytton RL. Prediction of permanent deformation in flexible pavement materials. Implication of Aggregates in the Design, Construction and Performance of Flexible Pavements. *ASTM STP* 1989;1016:154-172.
- [88] Ullidtz P. Modelling of granular materials using the discrete element method. Eighth International Conference on Asphalt Pavements Federal Highway Administration 1997;
- [89] Uzan J. Characterization of granular material. *Transportation Research Record* 1985;1022:52-59.
- [90] Vaitkus A, Gražulytė J, Skrodenis E, Kravcovas I. Design of frost resistant pavement structure based on road weather stations (rwss) data. *Sustainability* 2016;8:1328.
- [91] Van Genuchten MT. A closed-form equation for predicting the hydraulic conductivity of unsaturated soils. *Soil science society of America journal* 1980;44:892-898.
- [92] Witczak M, Uzan J. The universal airport pavement design system, report i of iv: Granular material characterization. University of Maryland, College Park, MD 1988;
- [93] Wu Z, Chen X, Yang X. Finite element simulation of structural performance on flexible pavements with stabilized base/treated subbase materials under accelerated loading. Louisiana Transportation Research Center, 2011;
- [94] Xiao Y. Performance-based evaluation of unbound aggregates affecting mechanistic response and performance of flexible pavements. University of Illinois at Urbana-Champaign; 2014.
- [95] Yavuzturk C, Ksaibati K. Assessment of fluctuations in asphalt pavement due to thermal environmental conditions using a two-dimensional transient finite differential approach. Department of Civil and Architectural Engineering, University of Wyoming, Wyoming 2002;
- [96] Zarling JP, Braley WA. Embankment design and construction in cold regions. In: Johnson EG, Phukan A, Haas WH, editors. *Geotechnical thermal analysis*. VA: ASCE press; 1988.
- [97] Zeiada W, Hamad K, Omar M, Underwood BS, Khalil MA, Karzad AS. Investigation and modelling of asphalt pavement performance in cold regions. *International Journal of Pavement Engineering* 2019;20:986-997.

- [98] Zhang H, Ma S, Yu T. Comparative study on HMA elastic modulus based on different predicting methods. *Journal of Chongqing Jiaotong University (Natural Science)* 2018a;37:35-39. [in Chinese].
- [99] Zhang L, Ke Y. Combinations of soil materials for granular capillary barriers for minimizing rainfall infiltration and gas emission. *Canadian Geotechnical Journal* 2017;54:1580-1591.
- [100] Zhang Y, Gu F, Luo X, Birgisson B, Lytton RL. Modeling stress-dependent anisotropic elastoplastic unbound granular base in flexible pavements. *Transportation Research Record* 2018b;2672:46-56.
- [101] Zhu Y, Ishikawa T, Subramanian SS, Luo B. Early warning system for rainfall and snowmelt induced slope failure in seasonally cold regions. *Soils and Foundations* 2021;61:198-217. <https://doi.org/10.1016/j.sandf.2020.11.009>.
- [102] Zuo G, Drumm EC, Meier RW. Environmental effects on the predicted service life of flexible pavements. *Journal of Transportation Engineering* 2007;133:47-56.